Doctoral Dissertation

Study of self-assembled structure of polysaccharide sacran using second harmonic generation microscopy

PHAN DINH THANG

Supervisor: **Goro Mizutani**

Graduate School of Advanced Science and Technology

Japan Advanced Institute of Science and Technology

Materials Science

March 2023

Abstract

The polysaccharide sacran is a supramolecular structure with many interesting natural properties such as super absorption of water, efficient adsorption of metal ions, and especially nonlinear optical susceptibility to the manifestations extraordinary strange. Moreover, the sacran molecule is a living molecule, its structure in an aqueous solution can change unpredictably due to its ability to self-assemble depending on the surrounding environment and solution concentration. This is really a big challenge for studying the structure using its nonlinear optical response. In this study, I have presented crucial research results from sonicated sacran molecules from initial 0.5 wt% sacran solutions with the methodology: combining SEM, EDX-SEM measurements, and SFG spectroscopy with SHG microscopy for the SHG-active sacran aggregates identified in sacran cast film made from ultrasonicated sacran solutions. The dissertation includes four chapters with the content:

Chapter 1: This chapter aims to give a brief overview of the theory of nonlinear optics and some most famous nonlinear optical effects commonly used in current research: sum- and difference frequency generation (S/DFG), second-harmonic generation (SHG), third-harmonic generation (THG), and coherent Raman scattering (CRS). Introduction to the background of surface second-harmonic generation (SSHG) and the SHG microscopy method used in this study of sacran molecular structure. Briefly summarize the sacran polysaccharide material used in this study and its crucial properties and raise the purpose and motivation for carrying out this study.

Chapter 2: This chapter includes an introduction to the laser system, the detector and receiver, the experimental setup of the SHG microscope, and the result of the SHG observational study that includes (i) power dependence of second-harmonic generation signal generated from sacran aggregates, (ii) polarization dependence of second-harmonic generation active sacran aggregates, (iii) nonlinear optical behavior and scavenging ability of sacran molecules, and conclusions.

Chapter 3: This section includes the combined experimental setup between SHG microscopy, SEM, EDX-SEM, and SFG spectroscopy. The results include SEM images and chemical element analysis maps of SHG-active sacran aggregates using EDX-SEM measurement and the SFG spectra of sacran cast film with very dense SHG spot distribution. In this chapter, I also pointed out the characterization of the SHG-sacran aggregates and modeled the structure of SHG-active sacran aggregates on the microscale.

Chapter 4 is a general conclusion about this study.

This study has added many points of insight into the sacran molecule whose SHG activity and nonlinear optical response at specific conditions depending on ultrasonication time and metal ion adsorption. I also first observed the SFG spectra of sacran molecules that can pave a new approach to studying this biomaterial.

I tentatively modeled the structure of the SHG-active sacran aggregates with positively charged sacran chains in the center of the SHG spot and aligned around by negatively charged sacran. On the other hand, water molecules are stored and well-aligned in the SGH-active sacran aggregates. Hence the hexagonal shape might come from an ice crystalline morphology like that of snow.

Keywords: Sacran, Second-harmonic generation (SHG) microscopy, Sum-frequency generation (SFG) spectroscopy, Scanning electron microscope (SEM), Energy-dispersive X-ray spectroscopy (EDS)

ACKNOWLEDGEMENTS

I would like to express my warmest thanks to my supervisor Professor Goro Mizutani who greatly encouraged me with his valuable advice, insight, and personal kindness. Professor Goro Mizutani is a respectable sensei; he is always ready to help students with the most enthusiasm. I had one of the most luckily in my life becoming his student. Working time in his lab will always be a wonderful and memorable time that will stay with me for the rest of my life. I also extend my sincere thanks to all the laboratory members with whom I met and worked together during my studying and working in Professor Mizutani's lab. They were very kind and friendly and helped me a lot.

I would like to thank Associate Prof. TSUTSUI Hidekazu who is my second supervisor. He also helped me a lot during my study at Jaist.

I would like to thank my internal committee members, Prof. KANEKO Tatsuo, Associate Prof. TSUTSUI Hidekazu , Associate Prof. OKEYOSHI Kosuke from School of Materials Science, JAIST, and Associate Professor MIYAUCHI Yoshihiro from National Defense Academy. I thank all of them for their time and consideration in serving on my thesis committee.

My special thanks to Professor KANEKO Tatsuo, for welcoming and supporting me during my research time. It might be difficult to go to the end of this journey without his help enthusiast. His scientific comments and laboratory collaboration have contributed in no small part to the results of my research. I also give my thanks to Kaneko sensei lab members: Ph.D. Maninder Singh, Ph.D. Kulisara Budpud, and Ph.D. Pruetsakorn Saosamniang sent me essential technique support in my preparation sample.

Table of Contents

List of tables

List of Figures

1. Chapter 1. General introduction to the nonlinear optical study of sacran aggregates

1.1. Nonlinear optical phenomena and applications

Nonlinear optical phenomena imply optical processes in which incident light interacts with the nonlinear-optical media and emits a new light having nonlinear proportional properties to the original lights. Nonlinear optical processes allow us to generate lights that have a tunable wavelength, change shape in space and time, and create the shortest events ever made by humans on a zeptosecond scale. [1] Nonlinear optical phenomena are the basis of most reputation applications in components of optical communications systems, optical sensing, and materials research. Nonlinear optical phenomena occur when an intense light (laser light) crosses passthrough a nonlinear dielectric coefficient material transparent to both the fundamental and emitted waves. Second-harmonic generation (SHG) was observed and demonstrated by an experiment in the year 1962 [2] to be the origin of nonlinear optics. In particular, the second harmonic light originated from nonlinear materials, and its intensity depends on the incident polarization as a quadratic function. However, the foundation of nonlinear optics originates with the discovery of the Kerr effect, [3]–[5] in which the rotation of the plane of polarization of the light propagates through a dielectric medium subjected to a large electric field, caused by the anisotropic field dependent refractive index variation. Another nonlinear phenomenon is the saturation of absorption in Uranium glass using intense light from a spark known as the state-filling effect, [6] proposed as the first nonlinear optical phenomenon.

Discussions about the nonlinear phenomena, primarily related to the harmonic generation and mixing process, [7] have been conducted and energy level diagram modeling of this process used an imaginary energy level known as the "virtual" level

energy [8] or virtual state of solid materials. Virtual energy is an energy state designed to explain the transition of atoms or molecules to a high-energy state that is not a real electronic energy state when simultaneously absorbing two or more photons of the same frequency or different frequencies. The SHG is a conversion energy process of fundamental frequencies (ω_1, ω_2) and the harmonic frequency (ω_3): $\omega_3 = \omega_1 + \omega_2, \omega_1 = \omega_2$ for the case of SHG. [9], [10] The fundamental theory of nonlinear optics was developed by Bloembergen, [11] Akhmanov and Khokhlov, [12] Y. Shen, [13] and R. Boyd, [14] The electric polarization-dependence ($\boldsymbol{P}$) of the medium on the external electric field ($\boldsymbol{E}$) of the laser pulses is popularly expressed by relationship.

$$\boldsymbol{P} = \varepsilon[\chi^{(1)} \cdot \boldsymbol{E} + \chi^{(2)} : \boldsymbol{EE} + \chi^{(3)} \vdots \boldsymbol{EEE} + \cdots] \quad (1\text{-}1)$$

where ε is the physical quantity of the permittivity $\varepsilon = \varepsilon_r \varepsilon_0, \varepsilon_0 \approx 8.8542 \times 10^{-12}$ [F m^{-1}] is the vacuum permittivity known or the electric constant, [15] $\chi^{(n)}$ are the n^{th}-order susceptibilities of the medium (n = 1, 2, 3, …), and is a tensor of rank n + 1. The electric polarization ($\boldsymbol{P}$) is the response of molecules of a medium to an electric field.

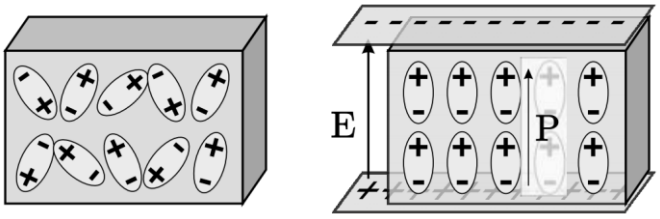

Figure 1. Creating polarization of a medium when an electric field is applied.

In an anisotropic case, the electric susceptibilities are tensors with the corresponding order that interact with the vector filed $\boldsymbol{E}$ by the scalar product ":". The susceptibility in the first term in the (1-1) equation ($\chi^{(1)}$) is the macroscopic average of the polarizability of the molecular electrons a and is known as the first-order (or linear) susceptibility. [16] Generally, polarization can be expressed by a sum.

$$\boldsymbol{P} = \boldsymbol{P}_L + \boldsymbol{P}_{NL} \quad (1\text{-}2)$$

where $\boldsymbol{P}_L = \varepsilon\chi^{(1)} \cdot \boldsymbol{E}$ is the linear part of the electric dipole polarization and governs linear-optical phenomena. $\boldsymbol{P}_{NL} = \varepsilon[\chi^{(2)}\!:\boldsymbol{EE} + \chi^{(3)} \vdots \boldsymbol{EEE} + \cdots]$ is the nonlinear part of the polarization, $\chi^{(2)} = \chi^{(2)}(\omega;\omega_1,\omega_2) = \chi^{(2)}(\omega = \omega_1 \pm \omega_2)$ is the second-order nonlinear-optical susceptibility that gives rise to three-wave mixing processes such as second-harmonic generation (SHG) ($\omega_1 = \omega_2$), sum-frequency generation (SFG)($\omega_{SFG} = \omega_1 + \omega_2$), and or difference-frequency generation (DFG) ($\omega_{DFG} = \omega_1 - \omega_2$). Second-order nonlinear optical phenomena can only happen in noncentrosymmetric, asymmetric, broken-symmetric, and chiral structural materials. The third susceptibility in the third term of equation (1-1), $\chi^{(3)} = \chi^{(3)}(\omega;\omega_1,\omega_2,\omega_3) = \chi^{(3)}(\omega = \omega_1 \pm \omega_2 \pm \omega_3)$ is the third-order nonlinear-optical susceptibility responses to four-wave mixing (FWM), stimulated Raman scattering, two-photon absorption, Kerr-effect-related phenomena such as self-phase modulation (SPM), and self-focusing…. The third-harmonic generation is a particular case of FWM in which three photons are of the same frequency ($\omega_1 = \omega_2 = \omega_3 = \omega_0$) and come from the same source. The cubic susceptibility is then calculated by $\chi^{(3)}_{THG} = \chi^{(3)}(3\omega_0;\omega_0,\omega_0,\omega_0)$. These nonlinear optical effects are described in the following table 1 and figure 1. [17] Some other special cases of nonlinear optical effects were also observed such as optical rectification (OR) ($\omega_1 = \omega_2 = \omega_0, \omega_0 - \omega_0 = 0$) [18], parametric amplification (PA) ($2\omega_0 - \omega_0 = \omega_0$), [19] electric field-induced second-harmonic generation (EFISH) ($\omega_0 + \omega_0 + 0 = 2\omega_0$), [20] and second-harmonic generation by five-wave mixing ($\omega_0 + \omega_0 + \omega_0 - \omega_0 = 2\omega_0$). [21]

Table 1. Nonlinear optical effects

Frequency of incident light	Frequency of scattered or emitted lights	Order of effect	The rank of the susceptibility tensor	Name of effect
ω	ω	1	2	Rayleigh scattering
ω_1, ω_2	$\omega_1 + \omega_2\ (\omega_1 = \omega_2)$ $\omega_1 + \omega_2\ (\omega_1 \neq \omega_2)$ $\omega_1 - \omega_2\ (\omega_1 \neq \omega_2)$	2	3	Second-harmonic generation Sum-frequency generation Difference-frequency generation

$\omega_1, \omega_2, \omega_3$	$\omega_1 + \omega_2 + \omega_3$ ($\omega_1 = \omega_2 = \omega_3$) $\omega_1 + \omega_2 + \omega_3$ ($\omega_1 \neq \omega_2 \neq \omega_3$) $\omega_1 - \omega_2 + \omega_3$ $\omega_1 + \omega_2 - \omega_3$ $\omega_1 - \omega_2 - \omega_3$	3	4	Third-harmonic generation Four-wave mixing
$\omega_1, \omega_2, \omega_3, \omega_4$	$\omega_1 + \omega_2 + \omega_3 + \omega_4$ ($\omega_1 = \omega_2 = \omega_3 = \omega_4$)	4	5	Four-harmonic generation
$\omega_1, \omega_2, \omega_3, \omega_4$	$\omega_1 \pm \omega_2 \pm \omega_3 \pm \omega_4$ ($\omega_1 \neq \omega_2 \neq \omega_3 \neq \omega_4$)	4	5	Five-wave mixing

One rarely beholds nonlinear optical phenomena in ordinary environments because the high-order susceptibilities are extremely smaller than linear susceptibility. The second-order susceptibility is proportional to the first-order susceptibility by a factor of $\chi^{(1)}/E_{at}$ and $\chi^{(3)} = \chi^{(2)}/E_{at}$, E_{at} [V/cm] is the atomic electric field strength. [9][14] Therefore, the conversion into higher harmonics is efficient for extremely intense fields applied as excitation light.

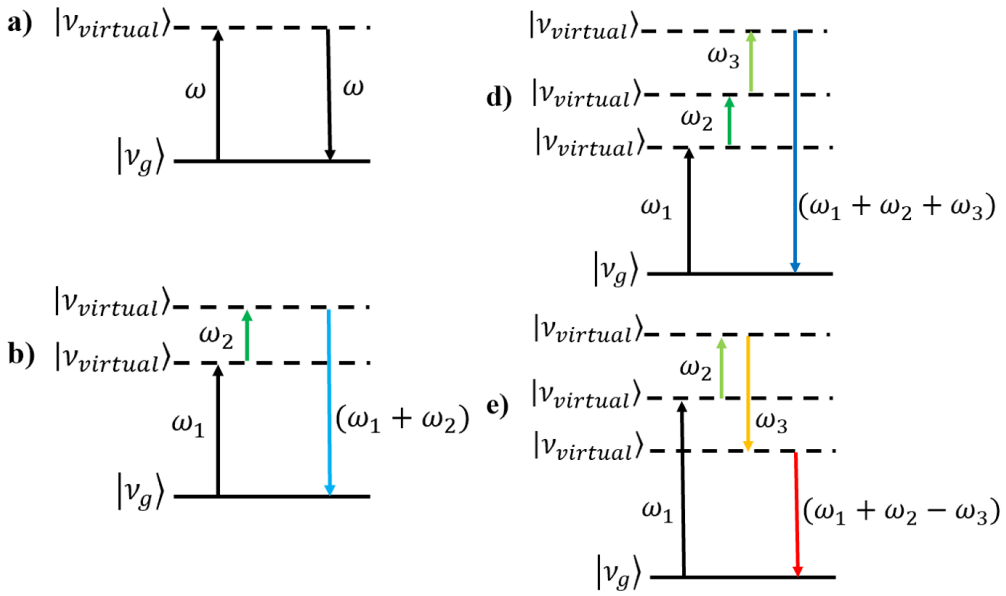

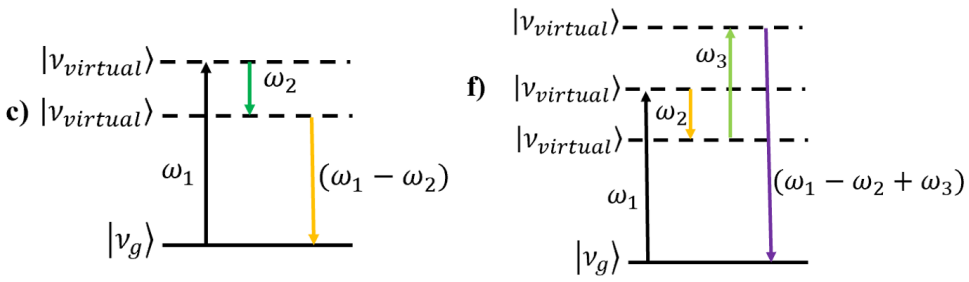

Figure 2. Linear process (a), second-order nonlinear processes (b, c), and third-order nonlinear processes (d, e, f)

The nonlinear optical phenomena are mathematically established based on the foundation of Maxwell's equations without magnetic fields, extraneous charges, and currents existing within the materials or influence. Maxwell's equations are written by:

$$\nabla \times \boldsymbol{E} = -\frac{\partial \boldsymbol{B}}{\partial t} \tag{1-3}$$

$$\nabla \times \boldsymbol{B} = \mu_o \frac{\partial \boldsymbol{D}}{\partial t} + \mu_o \mathbf{J}_f \tag{1-4}$$

$$\nabla \cdot \boldsymbol{D} = -\rho_f \tag{1-5}$$

$$\nabla \cdot \boldsymbol{B} = 0 \tag{1-6}$$

where μ is the permeability of material and equal to the vacuum permeability $\mu_0 \approx 1.256 \times 10^{-6}$ [kg.m.s^{-2}.A^{-2}], for the non-magnetic material, ρ_f (=0) is the free charge density, $\mathbf{J}_f$ (=0) is free current density, and $\nabla \times$ is the vector operator known as the curl. [22] Maxwell's equations are only applied to the materials without discontinuities. Therefore, there are a set of boundary conditions at the interface between two different materials.

(**i**) the different displacement currents between the normal components equal the surface-charge density.

$$\boldsymbol{n}_1 \cdot (\boldsymbol{D}_1)_\perp + \boldsymbol{n}_2 \cdot (\boldsymbol{D}_2)_\perp = \rho_s \tag{1-7}$$

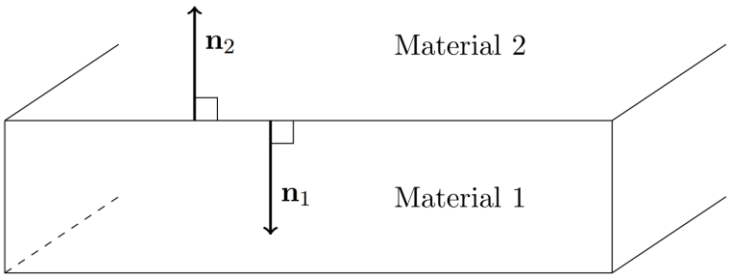

Figure 3. The boundary between two different materials

This boundary condition sometimes is supposed as a boundary condition for the electric field for some materials since $\boldsymbol{D} = n^2\varepsilon_0\boldsymbol{E}$, where n is the refractive index of the material. In a particular case of no charges inside and outside of the material, the displacement current is continuous across the interface between two materials.

(**ii**) the normal components of the magnetic induction in the two materials go continuously across the interface between the two materials.

$$\boldsymbol{n}_1 \cdot (\boldsymbol{B}_1)_\perp + \boldsymbol{n}_2 \cdot (\boldsymbol{B}_2)_\perp = 0 \tag{1-8}$$

(**iii**) vectorial tangential components of the electric field are continuous across the interface between two materials.

$$\boldsymbol{n}_1 \times (\boldsymbol{E}_1)_\parallel + \boldsymbol{n}_2 \times (\boldsymbol{E}_2)_\parallel = 0 \tag{1-9}$$

(**iv**) on the other hand, vectorial tangential components of the magnetic field equal the surface-current $\boldsymbol{J}_s$ across the interface between two materials.

$$\boldsymbol{n}_1 \times (\boldsymbol{H}_1)_\parallel + \boldsymbol{n}_2 \times (\boldsymbol{H}_2)_\parallel = \boldsymbol{J}_s \tag{1-10}$$

We establish the relationship between the electric field and the electric displacement by taking the curl equation (1-3) on both sides and substituting the right-hand side with equation (1-4). The first Maxwell's equation is rewritten by

$$\nabla \times \nabla \times \boldsymbol{E} = -\mu_0 \frac{\partial^2 \boldsymbol{D}}{\partial t^2} \tag{1-11}$$

The electric displacement $\boldsymbol{D}$ is defined by the sum of the electric field $\boldsymbol{E}$ and the polarization $\boldsymbol{P}$. [23]

$$\boldsymbol{D} = \varepsilon_0 \boldsymbol{E} + \boldsymbol{P} \tag{1-12}$$

Substituting equation (1-12) into the right-hand side of equation (1-11), we have only left the dependence of polarization on the electric field.

$$\nabla \times (\nabla \times \boldsymbol{E}) \ + \varepsilon_0 \mu_0 \frac{\partial^2 \boldsymbol{E}}{\partial t^2} = -\mu_0 \frac{\partial^2 \boldsymbol{P}}{\partial t^2} \tag{1-13}$$

The first term of the (1-13) equation is a combination of the second derivative of the vector field and is expressed using the Laplacian operator ∇^2: [24]

$$\nabla \times (\nabla \times \boldsymbol{E}) = \nabla(\nabla \cdot \boldsymbol{E}) - \ \nabla^2 \boldsymbol{E} \tag{1-14}$$

In the case of homogeneous media and without free density charges, the term inside the parentheses on the right-hand side is zero, $\nabla \cdot \boldsymbol{E} = 0$.

The equation (1-13) can be rewritten by

$$\nabla^2 \boldsymbol{E} - \varepsilon_0 \mu_0 \frac{\partial^2 \boldsymbol{E}}{\partial t^2} = \mu_0 \frac{\partial^2 \boldsymbol{P}}{\partial t^2} \tag{1-15}$$

$$\nabla^2 \boldsymbol{E} - \frac{1}{c^2} \frac{\partial^2 \boldsymbol{E}}{\partial t^2} = \frac{1}{\varepsilon_0 c^2} \frac{\partial^2 \boldsymbol{P}}{\partial t^2} \tag{1-16}$$

$$\nabla^2 \boldsymbol{E} - \frac{1}{c^2} \frac{\partial^2 \boldsymbol{E}}{\partial t^2} - \frac{1}{\varepsilon_0 c^2} \frac{\partial^2 \boldsymbol{P}_L}{\partial t^2} = \frac{1}{\varepsilon_0 c^2} \frac{\partial^2 \boldsymbol{P}_{NL}}{\partial t^2} \tag{1-17}$$

The equation (1-17) describes the propagation of the electric field in the media, where $c = \frac{1}{\sqrt{\varepsilon_0 \mu_0}} \approx 3 \times 10^8$ m/s is the speed of light in space. [25] The nonlinear polarization on the right-hand side of equation (1-17) plays the role of a source of nonlinear phenomena.

In the lossless linear materials $\boldsymbol{P}_L = \ \varepsilon_0 \chi^{(1)} : \boldsymbol{E}$ and we can get

$$-\nabla^2 \boldsymbol{E} = -\frac{\left(1+\chi^{(1)}\right)}{c^2} \frac{\partial^2 \boldsymbol{E}}{\partial t^2} = -\frac{\boldsymbol{\epsilon}}{c^2} \frac{\partial^2 \boldsymbol{E}}{\partial t^2} \tag{1-18}$$

where $\boldsymbol{\epsilon}$ is the frequency-dependent dielectric tensor and becomes a scalar quantity in an isotropic material case, the solution of the (1-18) equation has a general form

$$\boldsymbol{E} = \boldsymbol{E}_0 e^{i(kz \pm \omega t)} \tag{1-19}$$

In lossless materials, $\chi^{(1)}$ and $k = \omega\sqrt{1+\chi^{(1)}}/c$ have real values. In the case of complex susceptibility $\chi^{(1)} = \chi_r^{(1)} + i\chi_i^{(1)}$, the wavenumber should be a complex number $k = k_r + ik_i$. The real and imaginary parts of the wavenumber are approximately found as

$$k_r \approx \frac{\omega}{c}\sqrt{1+\chi_r^{(1)}} \tag{1-20}$$

$$k_i \approx \frac{1}{2}\frac{\omega}{c}\frac{\chi_i^{(1)}}{\sqrt{1+\chi_r^{(1)}}} \tag{1-21}$$

The polarization $\boldsymbol{P}$ of dielectric materials can be calculated by making up *N* dipoles per unit volume and assuming that all dipoles are lined up in the same direction.

$$\boldsymbol{P} = N\boldsymbol{p} \tag{1-22}$$

where $\boldsymbol{p} = q_1\boldsymbol{r}_1 + q_2\boldsymbol{r}_2 + q_3\boldsymbol{r}_3 + \cdots + q_n\boldsymbol{r}_n$ [Cm] is the dipole moment vector created by charges q_i at $\boldsymbol{r}_i$ respectively. The induced polarization P will be a linear function of a weak external applied electric field and become nonlinear behavior with an extreme external electric field applied to dielectric materials.

In this case, the external electric field is an infinite plane wave given by

$$\boldsymbol{E}(\boldsymbol{r},t) = \sum_{\boldsymbol{i}} \boldsymbol{E}_{\boldsymbol{i}}(\boldsymbol{k}_i,\omega_i) = \sum_{\boldsymbol{i}} A_i e^{-i(\omega_i t - \boldsymbol{k}\cdot\boldsymbol{r})} \tag{1-23}$$

The linear and nonlinear polarization are set by

$$\boldsymbol{P}_L(\boldsymbol{r},t) = \sum_i \chi^{(1)}(\omega_i)\boldsymbol{E}_{\boldsymbol{i}}(\boldsymbol{k}_i,\omega_i) \tag{1-24}$$

$$\boldsymbol{P}_{NL}(\boldsymbol{r},t) = \sum_m \boldsymbol{P}_{NL}(\boldsymbol{k}_m,\omega) = \sum P_{NL} e^{-i(\omega t - \boldsymbol{k}_m\cdot\boldsymbol{r})} \tag{1-25}$$

where A_i is independent of time, $\varepsilon(\omega_i) \equiv 1 + 4\pi\chi^{(1)}(\omega_i)$. The equation (1-17) becomes.

$$\nabla^2\boldsymbol{E}(\boldsymbol{r},t) - \frac{\omega^2}{c^2}\boldsymbol{\epsilon}\cdot\boldsymbol{E}(\boldsymbol{r},t) = \frac{\omega^2}{\varepsilon_0 c^2}\boldsymbol{P}_{NL}(\boldsymbol{k}_m,\omega) \tag{1-26}$$

Let's consider the electric fields are assumed to be quasi-monochromatic plane waves and propagate along the z-axis, then the electric fields are written by

$$\boldsymbol{E} = \vec{E}(\vec{r},t) = Re\left[\boldsymbol{e}A(z,t)e^{-i(\omega t - kz)}\right] \tag{1-27}$$

where k is the wave vector, $A(z,t)$ is the envelope of the electric field.

The nonlinear polarization is given by

$$\boldsymbol{P}_{NL} = \vec{P}_{NL}(\vec{r},t) = Re\left[\boldsymbol{e}_P P_{NL}(z,t)e^{-i(\omega t - k_P z)}\right] \tag{1-28}$$

We assume that the envelope function $A(z,t)$ is almost independent of the frequency of the electric field. The second-order partial derivative in the direction of wave propagation is negligible to the first-order partial derivative: $\left|{\partial^2 A}/{\partial z^2}\right| \ll \left|{k\partial A}/{\partial z}\right|$.

The equation (1-17) will become as

$$\frac{\partial A}{\partial z} + \frac{\partial k}{\partial \omega}\left(\frac{\partial A}{\partial t}\right) = \frac{i\omega^2}{\varepsilon_0 k c^2} P_{NL} e^{i\Delta \boldsymbol{k} z} \tag{1-29}$$

where $\left(\frac{\partial k}{\partial \omega}\right)^{-1}$ displays the variations of the envelope function of the wave propagating through space and known as group velocity, $k = \omega n/c$, and $\Delta\boldsymbol{k} = \boldsymbol{k}_P - \boldsymbol{k}$ is the wave–vector mismatch.

Generally, the electric field is a combination of components parallel and perpendicular components to wave – vector $\boldsymbol{k}$: $\boldsymbol{E} = \boldsymbol{E}_{\parallel} + \boldsymbol{E}_{\perp}$. Logically, the nonlinear polarization is also now represented in the same way $\boldsymbol{P}_{NL} = (\boldsymbol{P}_{NL})_{\parallel} + (\boldsymbol{P}_{NL})_{\perp}$. Therefore, the wave equation will become

$$\nabla^2 \boldsymbol{E}_{\perp} - \frac{\omega^2}{c^2}(\boldsymbol{\epsilon}\cdot\boldsymbol{E})_{\perp} = \frac{\omega^2}{\varepsilon_0 c^2}(\boldsymbol{P}_{NL})_{\perp}(\omega,z) \tag{1-30}$$

and

$$\nabla\cdot[(\boldsymbol{\epsilon}\cdot\boldsymbol{E})_{\parallel} + \varepsilon_0^{-1}(\boldsymbol{P}_{NL})_{\parallel}] = 0 \tag{1-31}$$

$$\nabla^2 \boldsymbol{E}_{\perp} = \frac{\partial^2}{\partial z^2}\boldsymbol{E}_{\perp} = e^{-i(\omega t - kz)}\left[\frac{\partial^2}{\partial z^2} + i2k\frac{\partial}{\partial z} - k^2\right]E_{\perp}(z) \tag{1-32}$$

where,

$$-k^2 \boldsymbol{E}_{\perp} + \frac{\omega^2}{c^2}(\boldsymbol{\epsilon}\cdot\boldsymbol{E})_{\perp} = 0 \tag{1-33}$$

Second-order nonlinear optical phenomena

In general, the second-order nonlinear processes happen when two incident infinite plane waves $\boldsymbol{E}(\boldsymbol{k}_1, \omega_1)$ and $\boldsymbol{E}(\boldsymbol{k}_2, \omega_2)$ interact with the electric media and generate a new wave $\boldsymbol{E}(\boldsymbol{k}, \omega = \omega_1 + \omega_2)$. The wave equation becomes

$$\left(\nabla^2 - \frac{\omega_1^2}{c^2}\boldsymbol{e}_1\right)\boldsymbol{E}_1(\boldsymbol{k}_1, \omega_1) = \frac{\omega_1^2}{\varepsilon_1 c^2}\boldsymbol{P}^{(2)}(\omega_1)$$

$$= \frac{\omega_1^2}{\varepsilon_1 c^2}\chi^{(2)}(\omega_1 = -\omega_2 + \omega)\boldsymbol{E}_2^*(\boldsymbol{k}_2, \omega_2)\boldsymbol{E}(\boldsymbol{k}, \omega) \quad (1\text{-}34)$$

$$\left(\nabla^2 - \frac{\omega_2^2}{c^2}\boldsymbol{e}_2\right)\boldsymbol{E}_2(\boldsymbol{k}_2, \omega_2) = \frac{\omega_1^2}{\varepsilon_1 c^2}\boldsymbol{P}^{(2)}(\omega_2)$$

$$= \frac{\omega_1^2}{\varepsilon_1 c^2}\chi^{(2)}(\omega_2 = \omega - \omega_1)\boldsymbol{E}(\boldsymbol{k}, \omega)\boldsymbol{E}_1^*(\boldsymbol{k}_1, \omega_1) \quad (1\text{-}35)$$

$$\left(\nabla^2 - \frac{\omega_1^2}{c^2}\boldsymbol{e}\right)\boldsymbol{E}(\boldsymbol{k}, \omega) = \frac{\omega_1^2}{\varepsilon_1 c^2}\boldsymbol{P}^{(2)}(\omega_1)$$

$$= \frac{\omega_1^2}{\varepsilon_1 c^2}\chi^{(2)}(\omega = \omega_2 + \omega_1)\boldsymbol{E}(\boldsymbol{k}_1, \omega_1)\boldsymbol{E}(\boldsymbol{k}_2, \omega_2) \quad (1\text{-}36)$$

If momentum conservation $\boldsymbol{k} = \boldsymbol{k}_1 + \boldsymbol{k}_2$ is satisfied, the wave coupling reaches the maximum. This condition is known as the phase-matching condition. Two optical fields interact in the medium and create an optical field amplitude given by

$$\boldsymbol{E}(t) = \boldsymbol{E}(\omega_1)e^{-i\omega_1 t} + \boldsymbol{E}(\omega_2)e^{-i\omega_2 t} + c.c. \quad (1\text{-}37)$$

The second-order phenomena can directly be seen by the second order polarization.

$$\boldsymbol{P}^{(2)}(t) = \chi^{(2)}(2\omega_1; \omega_1, \omega_1)E^2(\omega_1)e^{-i2\omega_1 t} + \chi^{(2)}(2\omega_2; \omega_2, \omega_2)E^2(\omega_2)e^{-i2\omega_2 t}$$

$$+\frac{1}{2}\left[\chi^{(2)}(\omega_1 + \omega_2; \omega_1, \omega_2) + \chi^{(2)}(\omega_2 + \omega_1; \omega_2, \omega_1)\right]E(\omega_1)E(\omega_2)e^{-i(\omega_1+\omega_2)t}$$

$$+\frac{1}{2}\left[\chi^{(2)}(\omega_1 - \omega_2; \omega_1, -\omega_2)\right.$$

$$\left.+ \chi^{(2)}(-\omega_2 + \omega_1; -\omega_2, \omega_1)\right]E(\omega_1)E^*(\omega_2)\left\langle e^{-i\omega_2 t}\middle| e^{-i(\omega_1-\omega_2)t}\right\rangle + c.c.$$

$$+\left[\chi^{(2)}(0; \omega_1, -\omega_1) + \chi^{(2)}(0; -\omega_1, \omega_1)\right]|E(\omega_1)|^2 + \left[\chi^{(2)}(0; \omega_2, -\omega_2) +\right.$$

$$\left.\chi^{(2)}(0; -\omega_2, \omega_2)\right]|E(\omega_2)|^2 \quad (1\text{-}38)$$

Optical rectification

The optical rectification (OR) phenomenon describes a quasi-DC polarization generated inside a nonlinear material when intense electric passing throughout that material [18]. Assuming an intense laser pulse with frequency ω is incident on a material without a center of symmetry, the second-order nonlinear polarization of the material can happen $\omega + \omega = 2\omega$ and $\omega - \omega = 0$ components corresponding to second-harmonic generation (SHG) and OR, respectively. The OR occurs when the polarization changes its sign more slowly than the applied field. Crystal materials exhibit a large linear electro-optic effect such as potassium dihydrogen phosphate (KDP) and potassium di-deuterium phosphate (KD_dP) are reported as the first case of the optical rectification phenomenon.

$$\boldsymbol{P}^{(2)}(0) = \chi^{(2)}(0 = \omega - \omega) : \boldsymbol{E}(\omega)\boldsymbol{E}^{*}(\omega) \tag{1-39}$$

$$\boldsymbol{P}^{(2)}(0) = \left[\chi^{(2)}(0; \omega_1, -\omega_1) + \chi^{(2)}(0; -\omega_1, \omega_1)\right]|\boldsymbol{E}(\omega_1)|^2 + \left[\chi^{(2)}(0; \omega_2, -\omega_2) + \chi^{(2)}(0; -\omega_2, \omega_2)\right]|\boldsymbol{E}(\omega_2)|^2 \tag{1-40}$$

The electric field is assumed $\boldsymbol{E}(\omega) = E_i e^{-i(\omega_i t - \boldsymbol{k}\cdot\boldsymbol{r})}$. There exists a permutation relation of the nonlinear susceptibility $\chi^{(2)}(0 = \omega - \omega)$

$$\chi_{ijk}^{(2)}(0 = \omega - \omega) = \chi_{jki}{}^{(2)}(\omega = \omega + 0) = \chi_{kij}{}^{(2)}(\omega = 0 + \omega)$$

$$= -\frac{\varepsilon_{ii}^{(1)}\varepsilon_{jj}^{(1)}}{4\pi} r_{ijk} \tag{1-41}$$

The voltage across the crystal materials of the optical rectification phenomenon is

$$V = -4\pi\left(\frac{s\times t}{\varepsilon_0 w}\right)\sum_{j,k}\chi_{ijk}^{(2)}\boldsymbol{E}_j(\omega)\boldsymbol{E}_k^{*}(\omega) \tag{1-42}$$

where r_{ijk} is the electrooptical coefficient, and $s \times t$ is the rectangular cross-section of the crystal. The optical rectification was used to generate electromagnetic waves in the terahertz region when an incident femtosecond electric field was applied. [26] A strong terahertz electric field emitted from the surface of a 100 nm thick Au plate excited by Ti:

sapphire femtosecond laser with a repetition rate of 11 MHz. [27], [28] This phenomenon isn't only similar to effects such as surface second harmonic generation (SSHG) and surface sum-frequency generation (SSFG), but it also can be enhanced by surface plasmons.

Sum – and difference–frequency generation

Two electric fields with angular frequencies ω_1 and ω_2 excite an electric material, a nonlinear crystal, and generate one new photon at a frequency $\omega_3 = \omega_1 + \omega_2$. In the sum-frequency process, the wave-vector matching condition satisfied $\Delta\boldsymbol{k} = \boldsymbol{k}_1 + \boldsymbol{k}_2 - \boldsymbol{k}_3$, and $\boldsymbol{k}_i$ is the wave vector of the *i*th field. Nonlinear polarization is

$$\boldsymbol{P}^{(2)}(t) = \frac{1}{2}[\chi^{(2)}(\omega_1 + \omega_2; \omega_1, \omega_2) + \chi^{(2)}(\omega_2 + \omega_1; \omega_2, \omega_1)]\boldsymbol{E}(\omega_1)\boldsymbol{E}(\omega_2)e^{-i(\omega_1+\omega_2)t} + c.c. \quad (1\text{-}43)$$

The susceptibility in equation (1-43) is a third-rank tensor containing two tensors of each of 27 elements and they are permuted.

$$\chi^{(2)}_{ijk}(\omega_3 = \omega_1 + \omega_2) = \chi_{jki}{}^{(2)}(\omega_3 = \omega_1 + \omega_2) = \chi_{kij}{}^{(2)}(\omega_3 = \omega_1 + \omega_2) = \chi_{ikj}{}^{(2)}(\omega_3 = \omega_1 + \omega_2) = \chi_{jik}{}^{(2)}(\omega_3 = \omega_1 + \omega_2) = \chi_{kji}{}^{(2)}(\omega_3 = \omega_1 + \omega_2) \quad (1\text{-}44)$$

$$P(\omega_1 + \omega_2) = \begin{bmatrix} \chi^{(2)}_{111}(\omega_1,\omega_2) & \chi^{(2)}_{122}(\omega_1,\omega_2) & \chi^{(2)}_{133}(\omega_1,\omega_2) & \chi^{(2)}_{123}(\omega_1,\omega_2) & \chi^{(2)}_{132}(\omega_1,\omega_2) \\ \chi^{(2)}_{113}(\omega_1,\omega_2) & \chi^{(2)}_{131}(\omega_1,\omega_2) & \chi^{(2)}_{112}(\omega_1,\omega_2) & \chi^{(2)}_{121}(\omega_1,\omega_2) & \\ \chi^{(2)}_{211}(\omega_1,\omega_2) & \chi^{(2)}_{222}(\omega_1,\omega_2) & \chi^{(2)}_{233}(\omega_1,\omega_2) & \chi^{(2)}_{223}(\omega_1,\omega_2) & \chi^{(2)}_{232}(\omega_1,\omega_2) \\ \chi^{(2)}_{213}(\omega_1,\omega_2) & \chi^{(2)}_{231}(\omega_1,\omega_2) & \chi^{(2)}_{212}(\omega_1,\omega_2) & \chi^{(2)}_{221}(\omega_1,\omega_2) & \\ \chi^{(2)}_{311}(\omega_1,\omega_2) & \chi^{(2)}_{322}(\omega_1,\omega_2) & \chi^{(2)}_{333}(\omega_1,\omega_2) & \chi^{(2)}_{323}(\omega_1,\omega_2) & \chi^{(2)}_{332}(\omega_1,\omega_2) \\ \chi^{(2)}_{313}(\omega_1,\omega_2) & \chi^{(2)}_{331}(\omega_1,\omega_2) & \chi^{(2)}_{312}(\omega_1,\omega_2) & \chi^{(2)}_{321}(\omega_1,\omega_2) & \end{bmatrix} \begin{bmatrix} E_1(\omega_1)E_1(\omega_2) \\ E_2(\omega_1)E_2(\omega_2) \\ E_3(\omega_1)E_3(\omega_2) \\ E_2(\omega_1)E_3(\omega_2) \\ E_3(\omega_1)E_2(\omega_2) \\ E_1(\omega_1)E_3(\omega_2) \\ E_3(\omega_1)E_1(\omega_2) \\ E_1(\omega_1)E_2(\omega_2) \\ E_2(\omega_1)E_1(\omega_2) \end{bmatrix} \quad (1\text{-}45)$$

$$P(\omega_2+\omega_1)=\begin{bmatrix}\chi^{(2)}_{111}(\omega_2,\omega_1) & \chi^{(2)}_{122}(\omega_2,\omega_1) & \chi^{(2)}_{133}(\omega_2,\omega_1) & \chi^{(2)}_{123}(\omega_2,\omega_1) & \chi^{(2)}_{132}(\omega_2,\omega_1)\\ \chi^{(2)}_{113}(\omega_2,\omega_1) & \chi^{(2)}_{131}(\omega_2,\omega_1) & \chi^{(2)}_{112}(\omega_2,\omega_1) & \chi^{(2)}_{121}(\omega_2,\omega_1) & \\ \chi^{(2)}_{211}(\omega_2,\omega_1) & \chi^{(2)}_{222}(\omega_2,\omega_1) & \chi^{(2)}_{233}(\omega_2,\omega_1) & \chi^{(2)}_{223}(\omega_2,\omega_1) & \chi^{(2)}_{232}(\omega_2,\omega_1)\\ \chi^{(2)}_{213}(\omega_2,\omega_1) & \chi^{(2)}_{231}(\omega_2,\omega_1) & \chi^{(2)}_{212}(\omega_2,\omega_1) & \chi^{(2)}_{221}(\omega_2,\omega_1) & \\ \chi^{(2)}_{311}(\omega_2,\omega_1) & \chi^{(2)}_{322}(\omega_2,\omega_1) & \chi^{(2)}_{333}(\omega_2,\omega_1) & \chi^{(2)}_{323}(\omega_2,\omega_1) & \chi^{(2)}_{332}(\omega_2,\omega_1)\\ \chi^{(2)}_{313}(\omega_2,\omega_1) & \chi^{(2)}_{331}(\omega_2,\omega_1) & \chi^{(2)}_{312}(\omega_2,\omega_1) & \chi^{(2)}_{321}(\omega_2,\omega_1) & \end{bmatrix}\begin{bmatrix}E_1(\omega_2)E_1(\omega_1)\\ E_2(\omega_2)E_2(\omega_1)\\ E_3(\omega_2)E_3(\omega_1)\\ E_2(\omega_2)E_3(\omega_1)\\ E_3(\omega_2)E_2(\omega_1)\\ E_1(\omega_2)E_3(\omega_1)\\ E_3(\omega_2)E_1(\omega_1)\\ E_1(\omega_2)E_2(\omega_1)\\ E_2(\omega_2)E_1(\omega_1)\end{bmatrix} \quad (1\text{-}46)$$

The total number of independent terms of susceptibility tensors will reduce from 54 to 30 elements when Kleinman's symmetry matrices are applied. The second-order susceptibility tensors in the form of D-matrices

$$d_{ijk}=\frac{1}{2}\chi^{(2)}_{ijk} \quad (1\text{-}47)$$

$$\begin{array}{cccccccc} jk & 11 & 22 & 33 & 23,32 & 31,13 & 12,21 \\ l & 1 & 2 & 3 & 4 & 5 & 6 \end{array} \quad (1\text{-}48)$$

$$d_{il}=\begin{pmatrix} d_{11} & d_{12} & d_{13} & d_{14} & d_{15} & d_{16} \\ d_{16} & d_{22} & d_{23} & d_{24} & d_{14} & d_{12} \\ d_{15} & d_{24} & d_{33} & d_{23} & d_{13} & d_{14} \end{pmatrix} \quad (1\text{-}49)$$

$$P(\omega_3=\omega_1+\omega_2)=\begin{bmatrix} d_{11} & d_{12} & d_{13} & d_{14} & d_{15} & d_{16} \\ d_{16} & d_{22} & d_{23} & d_{24} & d_{14} & d_{12} \\ d_{15} & d_{24} & d_{33} & d_{23} & d_{13} & d_{14} \end{bmatrix}\times\begin{bmatrix}E_1(\omega_1)E_1(\omega_2)\\ E_2(\omega_1)E_2(\omega_2)\\ E_3(\omega_1)E_3(\omega_2)\\ E_2(\omega_1)E_3(\omega_2)\\ E_3(\omega_1)E_2(\omega_2)\\ E_1(\omega_1)E_3(\omega_2)\\ E_3(\omega_1)E_1(\omega_2)\\ E_1(\omega_1)E_2(\omega_2)\\ E_2(\omega_1)E_1(\omega_2)\end{bmatrix} \quad (1\text{-}50)$$

The amplitude of the sum-frequency field can be written by

$$A_3(z,t)=i\gamma_3\int_0^L A_{10}\left[t-z/u_3+z(u_3^{-1}-u_1^{-1})\right]$$
$$\times A_{20}[t-z/u_3+z(u_3^{-1}-u_2^{-1})]\times e^{(-i\Delta kz)}dz \quad (1\text{-}51)$$

where $\gamma_3=\frac{2\pi\omega_3^2}{k_3c^2}\chi^{(2)}_{SFG}$, $A_{10}(t)=A_1(z,t)$, $A_{20}(t)=A_2(z,t)$, $u_i=(\partial k_i/\partial\,\omega_i)^{-1}$ is the group velocity that drives the efficiency of frequency conversion, and L is the thickness of the crystal medium. The sum-frequency process is an extremely good tool in the material

studying field with very high sensitivity and selectivity features. A weak scanning input field was used to generate the sum-frequency signal converted from the scanning field energy by mixing with an intense input field. The spectrum of the sum-frequency signal contains information on the molecular structure of the material used to study. For the plane–wave case, the effect of depletion of the scanning field (ω_1) will be converted to a signal field (ω_3). The coupled equations are given by

$$\frac{dA_3(z)}{dz} = \left(\frac{4i}{n_3^2} d_{eff} \frac{A_2}{4} k_3 e^{i\Delta \boldsymbol{k} z}\right) A_1(z) \tag{1-52}$$

$$\frac{dA_1(z)}{dz} = \left(\frac{4i}{n_1^2} d_{eff} \frac{A_2^*}{4} k_1 e^{-i\Delta \boldsymbol{k} z}\right) A_3(z) \tag{1-53}$$

We assume that the amplitude of the strong input field (ω_2) is not depleted. The sum-frequency field is generated without phase–delay. The coupled equations (1-52) and (1-53) can be rewritten by

$$\frac{dA_3(z)}{dz} = i\kappa_3 e^{i\Delta \boldsymbol{k} z} A_1(z) \tag{1-54}$$

$$\frac{dA_1(z)}{dz} = i\kappa_1 e^{-i\Delta \boldsymbol{k} z} A_3(z) \tag{1-55}$$

where $\kappa_1 = k_1 d_{eff} A_2 / n_1^2$, $\kappa_3 = k_3 d_{eff} A_2^* / n_3^2$

Differentiate the (1-54) equation and use the (1-55) equation we obtain.

$$\frac{d^2 A_3(z)}{dz^2} - i\Delta \boldsymbol{k} \frac{dA_3(z)}{dz} + \kappa_1 \kappa_3 A_3(z) = 0 \tag{1-56}$$

I assume that the general solution of the (1-56) equation is the form

$$A_3(z) = \left(Ce^{i\alpha z} + De^{-i\alpha z}\right) e^{i\Delta \boldsymbol{k} z/2} \tag{1-57}$$

At the $z = 0$, $A_3(0) = 0$ we have the boundary condition $C + D = 0$. Therefore

$$A_3(z) = 2iC sin(\alpha z) e^{i\Delta \boldsymbol{k} z/2} \tag{1-58}$$

Using the (1-58) to calculate the factor C, we obtain the amplitude of the sum-frequency field.

$$A_3(z) = 2i\left(\frac{-\kappa_3 A_1(0)}{2}\right) sin(\alpha z) e^{i\Delta \boldsymbol{k} z/2} \tag{1-59}$$

The intensity of the sum-frequency field can be calculated by

$$I_3(z) = \frac{A_3(z)A_3^*(z)}{2\eta_3} = \frac{\eta_1}{\eta_3} \cdot \kappa_3^2 \cdot I_1(0)\left(\frac{sin\alpha z}{\gamma}\right)^2 \tag{1-60}$$

In the ideal condition, the transferring energy will reach maximum conversion efficiency when the phase-matching condition is satisfied $\Delta \boldsymbol{k} = 0$, $\gamma = \sqrt{\kappa_1 \kappa_3}$. In addition, the thickness of the material must satisfy an equation $\sqrt{\kappa_1 \kappa_3} \mathrm{L_z} = \pi/2$ and the strong field $I_2 = \frac{\pi^2 n_1^2 n_3^2}{8 L_z k_1 k_3 \eta_2 d_{eff}^2}$. Therefore, the intensity of the sum-frequency field $I_3(L_z) = \frac{\lambda_1}{\lambda_3} I_1(0)$.

In the SFG process, the energy of two incident electric fields (ω_1 and ω_2) transfer to the energy of the SFG field ($\omega_1 + \omega_2$). On the other hand, in the difference-frequency generation (DFG) process, two incident electric fields interact and generate three photons of two fundamental electric fields and a new electric field$\omega_3 = \omega_1 - \omega_2$. In order to make energy transfer from ω_1 and ω_2 to $\omega_3$is required for the matching condition $\Delta \boldsymbol{k} = \boldsymbol{k}_1 - \boldsymbol{k}_2 - \boldsymbol{k}_3$.

$$\boldsymbol{P^{(2)}}(t) = +\frac{1}{2}[\chi^{(2)}(\omega_1 - \omega_2; \omega_1, -\omega_2)$$

$$+\chi^{(2)}(-\omega_2 + \omega_1; -\omega_2, \omega_1)]E(\omega_1)E^*(\omega_2)\left\langle e^{-i\omega_2 t}\middle| e^{-i(\omega_1-\omega_2)t}\right\rangle + c.c. \tag{1-61}$$

$$P\ (\omega_1 - \omega_2) = \begin{bmatrix} \chi^{(2)}_{111}(\omega_1,-\omega_2) & \chi^{(2)}_{122}(\omega_1,-\omega_2) & \chi^{(2)}_{133}(\omega_1,-\omega_2) & \chi^{(2)}_{123}(\omega_1,-\omega_2) & \chi^{(2)}_{132}(\omega_1,-\omega_2) \\ \chi^{(2)}_{113}(\omega_1,-\omega_2) & \chi^{(2)}_{131}(\omega_1,-\omega_2) & \chi^{(2)}_{112}(\omega_1,-\omega_2) & \chi^{(2)}_{121}(\omega_1,-\omega_2) & \\ \chi^{(2)}_{211}(\omega_1,-\omega_2) & \chi^{(2)}_{222}(\omega_1,-\omega_2) & \chi^{(2)}_{233}(\omega_1,-\omega_2) & \chi^{(2)}_{223}(\omega_1,-\omega_2) & \chi^{(2)}_{232}(\omega_1,-\omega_2) \\ \chi^{(2)}_{213}(\omega_1,-\omega_2) & \chi^{(2)}_{231}(\omega_1,-\omega_2) & \chi^{(2)}_{212}(\omega_1,-\omega_2) & \chi^{(2)}_{221}(\omega_1,-\omega_2) & \\ \chi^{(2)}_{311}(\omega_1,-\omega_2) & \chi^{(2)}_{322}(\omega_1,-\omega_2) & \chi^{(2)}_{333}(\omega_1,-\omega_2) & \chi^{(2)}_{323}(\omega_1,-\omega_2) & \chi^{(2)}_{332}(\omega_1,-\omega_2) \\ \chi^{(2)}_{313}(\omega_1,-\omega_2) & \chi^{(2)}_{331}(\omega_1,-\omega_2) & \chi^{(2)}_{312}(\omega_1,-\omega_2) & \chi^{(2)}_{321}(\omega_1,-\omega_2) & \end{bmatrix} \begin{bmatrix} E_1(\omega_1)E_1(-\omega_2) \\ E_2(\omega_1)E_2(-\omega_2) \\ E_3(\omega_1)E_3(-\omega_2) \\ E_2(\omega_1)E_3(-\omega_2) \\ E_3(\omega_1)E_2(-\omega_2) \\ E_1(\omega_1)E_3(-\omega_2) \\ E_3(\omega_1)E_1(-\omega_2) \\ E_1(\omega_1)E_2(-\omega_2) \\ E_2(\omega_1)E_1(-\omega_2) \end{bmatrix}$$

(1-62)

$$P(-\omega_2+\omega_1)=\begin{bmatrix}\chi^{(2)}_{111}(-\omega_2,\omega_1) & \chi^{(2)}_{122}(-\omega_2,\omega_1) & \chi^{(2)}_{133}(-\omega_2,\omega_1) & \chi^{(2)}_{123}(-\omega_2,\omega_1) & \chi^{(2)}_{132}(-\omega_2,\omega_1)\\ \chi^{(2)}_{113}(-\omega_2,\omega_1) & \chi^{(2)}_{131}(-\omega_2,\omega_1) & \chi^{(2)}_{112}(-\omega_2,\omega_1) & \chi^{(2)}_{121}(-\omega_2,\omega_1) & \\ \chi^{(2)}_{211}(-\omega_2,\omega_1) & \chi^{(2)}_{222}(-\omega_2,\omega_1) & \chi^{(2)}_{233}(-\omega_2,\omega_1) & \chi^{(2)}_{223}(-\omega_2,\omega_1) & \chi^{(2)}_{232}(-\omega_2,\omega_1)\\ \chi^{(2)}_{213}(-\omega_2,\omega_1) & \chi^{(2)}_{231}(-\omega_2,\omega_1) & \chi^{(2)}_{212}(-\omega_2,\omega_1) & \chi^{(2)}_{221}(-\omega_2,\omega_1) & \\ \chi^{(2)}_{311}(-\omega_2,\omega_1) & \chi^{(2)}_{322}(-\omega_2,\omega_1) & \chi^{(2)}_{333}(-\omega_2,\omega_1) & \chi^{(2)}_{323}(-\omega_2,\omega_1) & \chi^{(2)}_{332}(-\omega_2,\omega_1)\\ \chi^{(2)}_{313}(-\omega_2,\omega_1) & \chi^{(2)}_{331}(-\omega_2,\omega_1) & \chi^{(2)}_{312}(-\omega_2,\omega_1) & \chi^{(2)}_{321}(-\omega_2,\omega_1) & \end{bmatrix}\begin{bmatrix}E_1(-\omega_2)E_1(\omega_1)\\ E_2(-\omega_2)E_2(\omega_1)\\ E_3(-\omega_2)E_3(\omega_1)\\ E_2(-\omega_2)E_3(\omega_1)\\ E_3(-\omega_2)E_2(\omega_1)\\ E_1(-\omega_2)E_3(\omega_1)\\ E_3(-\omega_2)E_1(\omega_1)\\ E_1(-\omega_2)E_2(\omega_1)\\ E_2(-\omega_2)E_1(\omega_1)\end{bmatrix} \quad (1\text{-}63)$$

In this process, the intensity of fields with frequencies of ω_2 and ω_3 increase with decreasing intensity field frequency of ω_1. The amplitude of these remaining two fields in the stationary regime is

$$\frac{\partial A_2}{\partial z}+\frac{1}{u_2}\frac{\partial A_2}{\partial t}=i\gamma_2 A_1 A_3^* e^{i\Delta kz} \quad (1\text{-}64)$$

$$\frac{\partial A_3}{\partial z}+\frac{1}{u_3}\frac{\partial A_3}{\partial t}=i\gamma_3 A_1 A_2^* e^{-i\Delta kz} \quad (1\text{-}65)$$

where,

$$\gamma_2=\frac{2\pi\omega_2^2}{k_2c^2}\chi^{(2)}(\omega_2;\omega_1,-\omega_3) \quad (1\text{-}66)$$

$$\gamma_3=\frac{2\pi\omega_3^2}{k_3c^2}\chi^{(2)}(\omega_3;\omega_1,-\omega_2) \quad (1\text{-}67)$$

The amplitude of the second field (ω_2) at the input time, $A_3(0,t)=0$, is the solution of the equation (1-64) and (1-65)

$$A_2(z)=A_2(0)\{cosh[(4\gamma_2\gamma_3^*|A_1|^2-(\Delta\boldsymbol{k})^2)z]\}$$
$$+i\frac{\Delta\boldsymbol{k}}{2(4\gamma_2\gamma_3^*|A_1|^2-(\Delta\boldsymbol{k})^2)}\sinh[(4\gamma_2\gamma_3^*|A_1|^2-(\Delta\boldsymbol{k})^2)z] \quad (1\text{-}68)$$

$$A_3(z)=iA_2(0)\sinh[(4\gamma_2\gamma_3^*|A_1|^2-(\Delta\boldsymbol{k})^2)z] \quad (1\text{-}69)$$

Second-harmonic generation (SHG)

A single incident monochromatic plane field, ω, interacts with the nonlinear medium and generates a new field with a frequency of 2ω. The second-harmonic generation wave equation is

$$\nabla^2 \boldsymbol{E}^{(2)}(2\omega) - \frac{n_{2\omega}^2}{c^2}\frac{\partial^2 \boldsymbol{E}^{(2)}(2\omega)}{\partial t^2} + c.c. = -\frac{2\omega^2}{c^2}\chi_{ijk}^{(2)} e^{-2i(\omega t - k_{2\omega} z)} + c.c. \quad (1\text{-}70)$$

The phase-matching condition $\boldsymbol{k}_2 = \boldsymbol{2k}_1$ being satisfied, the polarization expression for SHG is

$$P^{(2)}(t) = \chi^{(2)}(2\omega;\omega,\omega)E^2(\omega)e^{-i2\omega t} + c.c. \quad (1\text{-}71)$$

The intensity of the SHG signal is a function of the susceptibility tensor regardless of the order of interaction. The number of elements of the polarization in equation (1-71) is 27 corresponding to the number of the susceptibility tensor $\chi^{(2)}(2\omega;\omega,\omega)$.

$$P\,(2\omega) = 2\varepsilon_0 \begin{bmatrix} \chi_{111}^{(2)}(\omega,\omega) & \chi_{122}^{(2)}(\omega,\omega) & \chi_{133}^{(2)}(\omega,\omega) & \chi_{123}^{(2)}(\omega,\omega) & \chi_{132}^{(2)}(\omega,\omega) \\ \chi_{113}^{(2)}(\omega,\omega) & \chi_{131}^{(2)}(\omega,\omega) & \chi_{112}^{(2)}(\omega,\omega) & \chi_{121}^{(2)}(\omega,\omega) & \\ \chi_{211}^{(2)}(\omega,\omega) & \chi_{222}^{(2)}(\omega,\omega) & \chi_{233}^{(2)}(\omega,\omega) & \chi_{223}^{(2)}(\omega,\omega) & \chi_{232}^{(2)}(\omega,\omega) \\ \chi_{213}^{(2)}(\omega,\omega) & \chi_{231}^{(2)}(\omega,\omega) & \chi_{212}^{(2)}(\omega,\omega) & \chi_{221}^{(2)}(\omega,\omega) & \\ \chi_{311}^{(2)}(\omega,\omega) & \chi_{322}^{(2)}(\omega,\omega) & \chi_{333}^{(2)}(\omega,\omega) & \chi_{323}^{(2)}(\omega,\omega) & \chi_{332}^{(2)}(\omega,\omega) \\ \chi_{313}^{(2)}(\omega,\omega) & \chi_{331}^{(2)}(\omega,\omega) & \chi_{312}^{(2)}(\omega,\omega) & \chi_{321}^{(2)}(\omega,\omega) & \end{bmatrix} \begin{bmatrix} E_1^2(\omega) \\ E_2^2(\omega) \\ E_3^2(\omega) \\ E_2(\omega)E_3(\omega) \\ E_3(\omega)E_2(\omega) \\ E_1(\omega)E_3(\omega) \\ E_3(\omega)E_1(\omega) \\ E_1(\omega)E_2(\omega) \\ E_2(\omega)E_1(\omega) \end{bmatrix} \quad (1\text{-}72)$$

The total possible susceptibility terms in the (1-71) equation of the SHG process are 57 elements including 27 elements of the c.c. term. In most SHG cases, nonlinear material is excited up to the virtual energy levels. It means that there is no case of resonance. Using Kleinman's D-matrix, the number of elements of the susceptibility tensor reduces to 18 independent elements. Therefore, the polarization of SHG is rewritten as

$$P\,(2\omega) = 2\varepsilon_0 \begin{bmatrix} d_{11} & d_{12} & d_{13} & d_{14} & d_{15} & d_{16} \\ d_{21} & d_{22} & d_{23} & d_{24} & d_{25} & d_{26} \\ d_{31} & d_{32} & d_{33} & d_{34} & d_{35} & d_{36} \end{bmatrix} \times \begin{bmatrix} {E^2}_1(\omega) \\ {E^2}_2(\omega) \\ E_3^2(\omega) \\ 2E_2(\omega)E_3(\omega) \\ 2E_1(\omega)E_3(\omega) \\ 2E_1(\omega)E_2(\omega) \end{bmatrix} \quad (1\text{-}73)$$

Considering the case of plane waves propagating to the z direction, the SHG's polarization amplitudes are given by

$$P_2(z) = 2\varepsilon_0 d_{eff} E_1^2 = \varepsilon_0 \chi_{ijk}^{(2)} A_1^2 e^{2ik_1 z} \quad (1\text{-}74)$$

The coupled equation for the slowly varying envelopes becomes

$$\frac{\partial A_2}{\partial z} = -i\frac{2\omega^2}{k_2 c^2}\chi^{(2)}E_0^2 e^{i\Delta \boldsymbol{k} z} \tag{1-75}$$

where u_1 and u_2 are the group velocities of the incident field and second-harmonic field, respectively, and $\Delta \boldsymbol{k} = \boldsymbol{2k}_1 - \boldsymbol{k}_2$ is the wave-vector mismatch. Using the initial condition $A(0) = 0$, the amplitude of the SHG is the solution of the (1-75) equation as

$$A_2(z) = \frac{2\omega^2}{c^2}\chi^{(2)}E_0^2\frac{k_2\left(1-e^{i\Delta \boldsymbol{k} z}\right)-\Delta k\left(1-e^{-ik_2 z}\right)}{\Delta k k_2(\Delta k+k_2)} \tag{1-76}$$

The intensity of the SHG will be

$$I_2(z) = \frac{\omega^2}{4\varepsilon_0 c^2}\frac{\left|\chi^{(2)}(\omega)\right|^2}{n_1^2 n_2} I_1^2 z^2 sinc^2\left(\frac{\Delta k z}{2}\right) \tag{1-77}$$

where the function $sinc$ is shorthand for the function $\sin(z)/z$. The (1-77) equation indicates the importance of phase-matching in creating SHG. The dependence of SHG intensity on the phase-matching and the thickness of the nonlinear material is shown in figure 4. The SHG signal is only significant when $\Delta k \cdot z < \pi$.

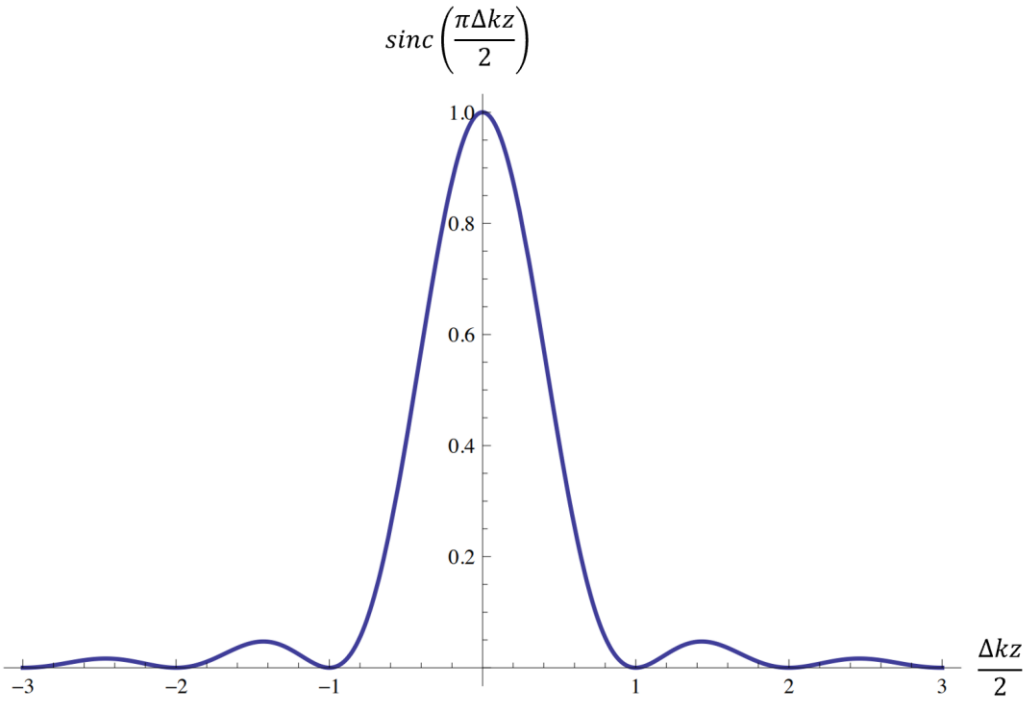

Figure 4. Second harmonic generation production efficiency depends on the magnitude of the phase-matching, $\Delta \boldsymbol{k}$, determined by eq. (1-77).

However, the phase-matching is different for the focused beam. At the focus point, the phase surface of the Gaussian beam shifts to an extra twist of phase. The focused beam has an equiphasic surface as the Gaussian distribution, [30 - 31] as shown in figure 5. Along propagation z-direction, a Gaussian beam acquires a phase shift that differs with respect to a plane wave with the same optical frequency. This difference is called the Gouy phase shift and its physical origin was explained by Simin Feng *et al*. [31]

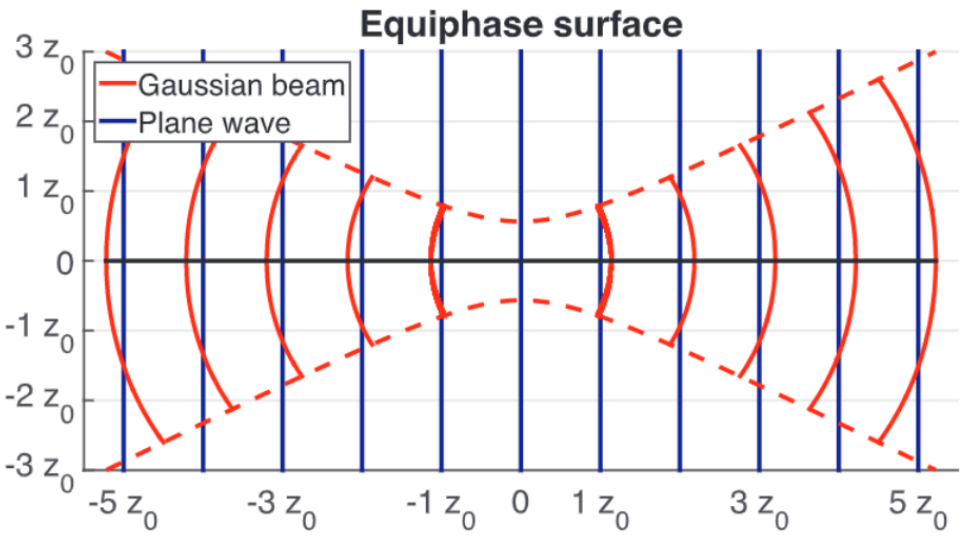

Figure 5. The equiphasic surfaces of a plane wave (blue lines) and of a Gaussian beam (red lines) in which the Gouy phase shift leads to the dephasing. The dashed red lines show the divergence radius of the Gaussian beam.

The twisted phase plane is a result of the convergence of the beam's rays from different angles. This brings a high potential for an efficient combination of phase-matching, which the total phase-matching balance can significantly alter.

In second-order optical nonlinear materials, the second-order susceptibility tensors generally vanish in centrosymmetric media. The non-zero, independent elements of second-order susceptibility tensors of some triclinic symmetry materials are shown in table 2.

Table 2. Independent nonvanishing elements of second-order susceptibility tensors for crystals of given symmetry classes.

Crystal system	Crystal class	Nonvanishing tensor elements
Triclinic	1	All elements are independent and nonzero
	$\bar{1}$	Each element vanishes
Monoclinic	2	xyz, xzy, xxy, xyx, yxx, yyy, yzz, yzx, yxz, zyz, zzy, zxy, zyx (twofold axis parallel to $\hat{y}$)
	m	xxx, xyy, xzz, xzx, xxz, yyz, yzy, yxy, yyx, zxx, zyy, zzz, zzx, zxz (mirror plane perpendicular to $\hat{y}$)
	2/m	each element vanishes
Orthorhombic	222	xyz, xzy, yzx, yxz, zxy, zyx
	mm2	xzx, xxz, yyz, yzy, zxx, zyy, zzz
	mmm	each element vanishes
Tetragonal	4	xyz=-yxz, xzy=-yzx, xzx=yzy, xxz=yyz, zxx-zyy, zzz, zxy=-zyx
	$\bar{4}$	xyz=yxz, xzy=yzx, xzx=-yzy, xxz=-yyz, zxx=-zyy, zxy=zyx
	422	xyz-=y, xzy=yxz, zxy=-zyx
	4mm	xzx=yzy, xxz=yyz, zxx=zyy,zzz
	$\bar{4}$2m	xyz=yxz, xzy=yzx, zxy=zyx
	4/m	each element vanishes
	4/mm	
Cubic	432	xyz=-xzy=yzx=-yxz=zxy=-zyx
	$\bar{4}$3m	xyz=xzy=yzx=yxz=zxy=zyx
	23	xyz=yzx=zxy, xzy=yxz=zyx
	m3,	each element vanishes
	m3m	
Trigonal	3	xxx=-xyy=-yyz=-yxy, xyz=-yxz, xzy=-yzx, xzx=-yzy, xxz=yyz, yyy=-yxx=-xxy=-xyx, zxx=zyy, zzz
	32	xxx=-xyy=-yyx=-yxy, xyz=-yxz, xzy=-yzx, zxy=-zyx
	3m	xzx=yzy, xxz=yyz, zxx=zyy, zzz, yyy=-yxx=-xxy=-xyx (mirror plane perpendicular to $\hat{x}$)
	$\bar{3}\bar{3}$m	each element vanishes
Hexagonal	6	xyz=-yxz, xzy=-yzx, xzx=yxy, xxz=yyz, zxx=zyy, zzz, zxy=-zyx
	$\bar{6}$	xxx=-xxy=-yxy=-yyx, yyy=-yxx=-xyx=-xxy
	622	xyz=-yxz, xzy=-yxz, zxy=-zyx
	6mm	xzx=yzy, xxz=yyz, zxx=zyy, zzz
	$\bar{6}$m2	yyy=-yxx=-xxy=-xyx
	6/m	each element vanishes
	6/mm	
	m	

One of the most popular applications of sum- and difference-frequency generation is to generate the selective wavelength or called optical parametric oscillation (OPO) using

nonlinear crystals such as KDP, [32] $LiNbO_3$, [19] and periodically poled lithium niobate (PPLN), [33] periodically poled $LiNbO_3$ and $KTiOPO_4$. [34] [35] These periodic materials show the important optical properties in table 3.

Table 3. Optical properties of some second-order nonlinear materials

Crystal (class)	*Transmission range (μm)*	*Refractive index (at 1.06 μm)*	*Nonlinear coefficient (pmV^{-1})*	*Damage threshold ($GWcm^{-2}$)*
Silver gallium selenide, $AgGaSe_2$ ($\bar{4}2m$)	0.78–18	$n_o=2.7010$ $n_e=2.6792$	$d_{36}=33$ (at 10.6 μm)	0.25 for 10 ns
β-Barium borate, BBO (3*m*)	0.21–2.1	$n_o=1.6551$ $n_e=1.5425$	$d_{22}=2.3$ $d_{24}=d_{15}\leqslant 0.1$	4.6 for 1 ns, 15 for 0.1 ns
Lithium iodate, $LiIO_3$ (6)	0.31–5	$n_o=1.8517$ $n_e=1.7168$	$d_{31}=-7.11$ $d_{33}=-7.02$ $d_{14}=0.31$	~0.5
Lithium niobate, $LiNbO_3$ (3*m*)		$n_o=2.234$ $n_e=2.155$	$d_{31}=-5.95$ $d_{33}=-34.4$	
Potassium dihydrogen phosphate, KH_2PO_4 (KDP)	0.18–1.55	$n_o=1.4944$ $n_e=1.4604$	$d_{36}=0.63$	
$KTiOPO_4$, KTP (*mm*2)	0.35–4.5	$n_x=1.7367$ $n_y=1.7395$ $n_z=1.8305$	$d_{31}=6.5$ $d_{32}=5.0$ $d_{33}=13.7$ $d_{24}=6.6$ $d_{15}=6.1$	

SHG is applied to generate efficient wavelength conversion by using the bulk-type quasi-phase mismatching device in MgO: $LiNbO_3$, $LiNbO_3$, and $LiTaO_3$ material. [36]

Third and high-order nonlinear optical phenomena

Three waves at frequencies ω_1, ω_2, and ω_3 participate in the third-order nonlinear process. The linear sum of these fundamental waves has the optical amplitude is

$$E(t) = E(\omega_1)e^{-i\omega_1 t} + E(\omega_2)e^{-i\omega_2 t} + E(\omega_3)e^{-i\omega_3 t} + c.c. \tag{1-78}$$

The third-order nonlinear polarization form is given by

$$P^{(3)}(t) = \{\chi^{(3)}(3\omega_1;\omega_1,\omega_1,\omega_1)E^3(\omega_1)e^{-i3\omega_1 t} + \chi^{(3)}(3\omega_2;\omega_2,\omega_2,\omega_2)E^3(\omega_2)e^{-i3\omega_2 t} + \chi^{(3)}(3\omega_3;\omega_3,\omega_3,\omega_3)E^3(\omega_3)e^{-i3\omega_3 t}\}$$

$$+\begin{Bmatrix} [\chi^{(3)}(2\omega_1+\omega_2)+\chi^{(3)}(\omega_1+\omega_2+\omega_1)+\chi^{(3)}(\omega_2+2\omega_1)]E^2(\omega_1)E(\omega_2)e^{-i(2\omega_1+\omega_2)t} \\ +[\chi^{(3)}(2\omega_1+\omega_3)+\chi^{(3)}(\omega_1+\omega_3+\omega_1)+\chi^{(3)}(\omega_3+2\omega_1)]E^2(\omega_1)E(\omega_3)e^{-i(2\omega_1+\omega_3)t} \\ +[\chi^{(3)}(\omega_1+2\omega_2)+\chi^{(3)}(\omega_2+\omega_1+\omega_2)+\chi^{(3)}(2\omega_2+\omega_1)]E(\omega_1)E^2(\omega_2)e^{-i(\omega_1+2\omega_2)t} \\ +[\chi^{(3)}(2\omega_2+\omega_3)+\chi^{(3)}(\omega_2+\omega_3+\omega_2)+\chi^{(3)}(\omega_3+2\omega_2)]E^2(\omega_2)E(\omega_3)e^{-i(2\omega_2+\omega_3)t} \\ +[\chi^{(3)}(2\omega_3+\omega_2)+\chi^{(3)}(\omega_3+\omega_2+\omega_3)+\chi^{(3)}(\omega_2+2\omega_3)]E^2(\omega_3)E(\omega_2)e^{-i(\omega_2+2\omega_3)t} \\ +[\chi^{(3)}(2\omega_3+\omega_1)+\chi^{(3)}(\omega_3+\omega_1+\omega_3)+\chi^{(3)}(\omega_1+2\omega_3)]E^2(\omega_3)E(\omega 1)e^{-i(\omega_1+2\omega_1)t} \end{Bmatrix}$$

$$+\begin{bmatrix} \chi^{(3)}(\omega_1+\omega_2+\omega_3)+\chi^{(3)}(\omega_1+\omega_3+\omega_2) \\ +\chi^{(3)}(\omega_2+\omega_1+\omega_3)+\chi^{(3)}(\omega_2+\omega_3+\omega_1) \\ +\chi^{(3)}(\omega_3+\omega_1+\omega_2)+\chi^{(3)}(\omega_3+\omega_2+\omega_1) \end{bmatrix} E(\omega_1)E(\omega_2)E(\omega_3)e^{-i(\omega_1+\omega_2+\omega_3)t}$$

$$
+\begin{Bmatrix}
\left[\chi^{(3)}(2\omega_1-\omega_2)+\chi^{(3)}(\omega_1-\omega_2+\omega_1)+\chi^{(3)}(-\omega_2+2\omega_1)\right]E^2(\omega_1)E^*(\omega_2)\langle e^{-i\omega_2}|e^{-i(2\omega_1-\omega_2)t}\rangle \\
+\left[\chi^{(3)}(2\omega_1-\omega_3)+\chi^{(3)}(\omega_1-\omega_3+\omega_1)+\chi^{(3)}(-\omega_3+2\omega_1)\right]E^2(\omega_1)E^*(\omega_3)\langle e^{-i\omega_3}|e^{-i(2\omega_1-\omega_3)t}\rangle \\
+\left[\chi^{(3)}(-\omega_1+2\omega_2)+\chi^{(3)}(\omega_2-\omega_1+\omega_2)+\chi^{(3)}(2\omega_2-\omega_1)\right]E^*(\omega_1)E^2(\omega_2)\langle e^{-i\omega_1}|e^{-i(2\omega_2-\omega_1)t}\rangle \\
+\left[\chi^{(3)}(2\omega_2-\omega_3)+\chi^{(3)}(\omega_2-\omega_3+\omega_2)+\chi^{(3)}(-\omega_3+2\omega_2)\right]E^2(\omega_2)E^*(\omega_3)\langle e^{-i\omega_3}|e^{-i(2\omega_2-\omega_3)t}\rangle \\
+\left[\chi^{(3)}(2\omega_3-\omega_2)+\chi^{(3)}(\omega_3-\omega_2+\omega_3)+\chi^{(3)}(-\omega_2+2\omega_3)\right]E^2(\omega_3)E^*(\omega_2)\langle e^{-i\omega_2}|e^{-i(2\omega_3-\omega_2)t}\rangle \\
+\left[\chi^{(3)}(2\omega_3-\omega_1)+\chi^{(3)}(\omega_3-\omega_1+\omega_3)+\chi^{(3)}(-\omega_1+2\omega_3)\right]E^2(\omega_3)E^*(\omega 1)\langle e^{-i\omega_1}|e^{-i(2\omega_3-\omega_1)t}\rangle
\end{Bmatrix}
$$

$$
+\begin{Bmatrix}
\begin{bmatrix}\chi^{(3)}(-\omega_1+\omega_2+\omega_3)+\chi^{(3)}(-\omega_1+\omega_3+\omega_2)\\ +\chi^{(3)}(\omega_2-\omega_1+\omega_3)+\chi^{(3)}(\omega_2+\omega_3-\omega_1)\\ +\chi^{(3)}(\omega_3-\omega_1+\omega_2)+\chi^{(3)}(\omega_3+\omega_2-\omega_1)\end{bmatrix}E^*(\omega_1)E(\omega_2)E(\omega_3)\langle e^{-i\omega_1}|e^{-i(-\omega_1+\omega_2+\omega_3)t}\rangle \\
+\begin{bmatrix}\chi^{(3)}(\omega_1-\omega_2+\omega_3)+\chi^{(3)}(\omega_1+\omega_3-\omega_2)\\ +\chi^{(3)}(-\omega_2+\omega_1+\omega_3)+\chi^{(3)}(-\omega_2+\omega_3+\omega_1)\\ +\chi^{(3)}(\omega_3+\omega_1-\omega_2)+\chi^{(3)}(\omega_3-\omega_2+\omega_1)\end{bmatrix}E(\omega_1)E^*(\omega_2)E(\omega_3)\langle e^{-i\omega_2}|e^{-i(\omega_1-\omega_2+\omega_3)t}\rangle \\
+\begin{bmatrix}\chi^{(3)}(\omega_1+\omega_2-\omega_3)+\chi^{(3)}(\omega_1-\omega_3+\omega_2)\\ +\chi^{(3)}(\omega_2+\omega_1-\omega_3)+\chi^{(3)}(\omega_2-\omega_3+\omega_1)\\ +\chi^{(3)}(-\omega_3+\omega_1+\omega_2)+\chi^{(3)}(-\omega_3+\omega_2+\omega_1)\end{bmatrix}E(\omega_1)E(\omega_2)E^*(\omega_3)\langle e^{-i\omega_3}|e^{-i(\omega_1+\omega_2-\omega_3)t}\rangle
\end{Bmatrix}
$$

$$
+\begin{Bmatrix}
\left[\chi^{(3)}(\omega_1;\omega_1,\omega_1,-\omega_1)+\chi^{(3)}(\omega_1;\omega_1,-\omega_1,\omega_1)+\chi^{(3)}(\omega_1;-\omega_1,\omega_1,\omega_1)\right]E(\omega_1)|E(\omega_1)|^2e^{-i\omega_1t} \\
+\left[\chi^{(3)}(\omega_2;\omega_2,\omega_2,-\omega_2)+\chi^{(3)}(\omega_2;\omega_2,-\omega_2,\omega_2)+\chi^{(3)}(\omega_2;-\omega_2,\omega_2,\omega_2)\right]E(\omega_2)|E(\omega_2)|^2e^{-i\omega_2t} \\
+\left[\chi^{(3)}(\omega_3;\omega_3,\omega_3,-\omega_3)+\chi^{(3)}(\omega_3;\omega_3,-\omega_3,\omega_3)+\chi^{(3)}(\omega_3;-\omega_3,\omega_3,\omega_3)\right]E(\omega_3)|E(\omega_3)|^2e^{-i\omega_3t}
\end{Bmatrix}
$$

$$
+\begin{Bmatrix}
\begin{bmatrix}\chi^{(3)}(\omega_2;-\omega_1,\omega_1,\omega_2)+\chi^{(3)}(\omega_2;\omega_1,-\omega_1,\omega_2)+\chi^{(3)}\left(\omega_2;\omega_2,\omega_1,-\omega_1\right)\\ \chi^{(3)}(\omega_2;\omega_2,\omega_1,-\omega_1)+\chi^{(3)}(\omega_2;\omega_1,\omega_2,-\omega_1)+\chi^{(3)}(\omega_2;-\omega_1,\omega_2,\omega_1)\end{bmatrix}E(\omega_2)|E(\omega_1)|^2e^{-i\omega_2t} \\
+\begin{bmatrix}\chi^{(3)}(\omega_3;-\omega_1,\omega_1,\omega_3)+\chi^{(3)}(\omega_3;\omega_1,-\omega_1,\omega_3)+\chi^{(3)}\left(\omega_3;\omega_3,\omega_1,-\omega_1\right)\\ \chi^{(3)}(\omega_3;\omega_3,\omega_1,-\omega_1)+\chi^{(3)}(\omega_3;\omega_1,\omega_3,-\omega_1)+\chi^{(3)}(\omega_3;-\omega_1,\omega_3,\omega_1)\end{bmatrix}E(\omega_3)|E(\omega_1)|^2e^{-i\omega_3t} \\
+\begin{bmatrix}\chi^{(3)}(\omega_1;-\omega_2,\omega_2,\omega_1)+\chi^{(3)}(\omega_1;\omega_2,-\omega_2,\omega_1)+\chi^{(3)}(\omega_1;\omega_1,\omega_2,-\omega_2)\\ \chi^{(3)}(\omega_1;\omega_1,-\omega_2,\omega_2)+\chi^{(3)}(\omega_1;\omega_2,\omega_1,-\omega_2)+\chi^{(3)}(\omega_1;-\omega_2,\omega_1,\omega_2)\end{bmatrix}E(\omega_1)|E(\omega_2)|^2e^{-i\omega_1t} \\
+\begin{bmatrix}\chi^{(3)}(\omega_3;-\omega_2,\omega_2,\omega_3)+\chi^{(3)}(\omega_3;\omega_2,-\omega_2,\omega_3)+\chi^{(3)}(\omega_3;\omega_3,-\omega_2,\omega_2)\\ \chi^{(3)}(\omega_3;\omega_3,-\omega_2,\omega_2)+\chi^{(3)}(\omega_3;\omega_2,\omega_3,-\omega_2)+\chi^{(3)}(\omega_3;-\omega_2,\omega_3,\omega_2)\end{bmatrix}E(\omega_3)|E(\omega_2)|^2e^{-i\omega_3t} \\
+\begin{bmatrix}\chi^{(3)}(\omega_1;-\omega_3,\omega_3,\omega_1)+\chi^{(3)}(\omega_1;\omega_3,-\omega_3,\omega_1)+\chi^{(3)}(\omega_1;\omega_1,\omega_3,-\omega_3)\\ \chi^{(3)}(\omega_1;\omega_1,-\omega_3,\omega_3)+\chi^{(3)}(\omega_1;\omega_3,\omega_1,-\omega_3)+\chi^{(3)}(\omega_1;-\omega_3,\omega_1,\omega_3)\end{bmatrix}E(\omega_1)|E(\omega_3)|^2e^{-i\omega_1t} \\
+\begin{bmatrix}\chi^{(3)}(\omega_2;-\omega_3,\omega_3,\omega_2)+\chi^{(3)}(\omega_2;\omega_3,-\omega_3,\omega_2)+\chi^{(3)}(\omega_2;\omega_2,\omega_3,-\omega_3)\\ \chi^{(3)}(\omega_2;\omega_2,-\omega_3,\omega_3)+\chi^{(3)}(\omega_2;\omega_3,\omega_2,-\omega_3)+\chi^{(3)}(\omega_2;-\omega_3,\omega_2,\omega_3)\end{bmatrix}E(\omega_2)|E(\omega_3)|^2e^{-i\omega_2t}
\end{Bmatrix}
\tag{1-79}
$$

$+c.c.$

The (1-79) equation shows the total interacting cases of three fundamental frequencies FWM, including 210 nonlinear susceptibility tensors. In particular, the special case of THG may fully have the number of elements of 486 in the third-harmonic susceptibility tensors if we consider the elements of c.c. term. Also, from the (1-79) equation, the other third-order nonlinear optical phenomena can occur as (i) the SFSHG and DFSHG nonlinear process might occur as a result of mixing the generated SHG frequencies with the other generated SFG frequencies, (ii) The DFSFG process is generated by the generated SFG

frequencies absent to other generated SFG frequencies, (iii) and no frequency generation (NFG) process that the emitted frequencies are same as fundamental frequencies. The total number of elements is given in table 4.

Table 4. Elements of third-order susceptibility tensors

Third-order nonlinear optical processes	Elements of susceptibility tensors	Total numbers
Third-harmonic generation (THG)	[(81+81(c.c.))(3ω1)] + [(81+81(c.c.))(3ω2)] + [(81+81(c.c.))(3ω3)]	468
Sum-frequency generation (SFG)	6(81+81(c.c.))(ω1+ω2+ω3)	972
Sum-frequency-second-harmonic generation (SFSHG)	{[3(81+81(c.c.))(2ω1+ω2)] + [3(81+81(c.c.))(2ω1+ω3)] +[3(81+81(c.c.))(2ω2+ω1)] + [3(81+81(c.c.))(2ω2+ω3)] +[3(81+81(c.c.))(2ω3+ω1)] +[3(81+81(c.c.))(2ω3+ω2)]}	2916
Difference-frequency- second-harmonic generation (DFSHG)	{[3(81+81(c.c.))(2ω1-ω2)] + [3(81+81(c.c.))(2ω1 ω3)] +[3(81+81(c.c.))(2ω2-ω1)] + [3(81+81(c.c.))(2ω2-ω3)] +[3(81+81(c.c.))(2ω3-ω1)]+[3(81+81(c.c.))(2ω3-ω2)]}	2916
Difference-frequency-sum-frequency generation (DFSFG)	{[6(81+81(c.c.))(-ω1+ω2+ω3)] + [6(81+81(c.c.))(ω1-ω2+ω3)] + [6(81+81(c.c.))(ω1+ω2-ω3)]}	2916
Degenerative No Frequency Generation (DNGF)	{[3(81+81(c.c.))(ω1)] + [3(81+81(c.c.))(ω2)] + [3(81+81(c.c.))(ω3)]}	1458
Non-Degenerative No Frequency Generation (NDNGF)	{[12(81+81(c.c.))(ω1)] + [12(81+81(c.c.))(ω2)] + [12(81+81(c.c.))(ω3)]}	5346

In the case of a single field interacting with the Centro-symmetric materials, the SFG and SFSHG become the THG process undergoing phase matching condition $\boldsymbol{k}_2 = 3\boldsymbol{k}_1$.

The nonlinear polarization of the THG is given by

$$P^{(3)}(t) = \chi^{(3)}(3\omega;\omega,\omega,\omega)E^3(\omega)e^{-i3\omega t} + c.c. \tag{1-80}$$

Or $$P^{(3)}(t) = 3d_{3\omega}^{THG}E^3(\omega)e^{-i3\omega t} \tag{1-81}$$

Using the (1-23) equation to express the form of the fundamental field $\boldsymbol{E}_1(\omega)$ and the THG field $\boldsymbol{E}_2(3\omega)$, the nonlinear polarization of the fundamental and THG waves should be

$$P^{(3)}(\omega,z) = \varepsilon_0\chi^{(3)}(3\omega,-\omega,-\omega)\boldsymbol{e}_2\boldsymbol{e}_1\boldsymbol{e}_1A_2(z)A_1^*(z)A_1^*(z)e^{i(k_2-2k_1)z} \tag{1-82}$$

$$P^{(3)}(3\omega,z) = \varepsilon_0\chi^{(3)}(\omega,\omega,\omega)\boldsymbol{e}_1\boldsymbol{e}_1\boldsymbol{e}_1A_1^3(z)e^{i(3k_1)z} \tag{1-83}$$

The coupled-wave function will come

$$\frac{\partial A_2(z)}{\partial z} = \frac{ik_2\varepsilon_0}{2\varepsilon(3\omega)}\chi_e^{(3)}A_1(z)e^{i\Delta kz}, \text{ where } \chi_e^{(3)} = \boldsymbol{e}_2\cdot\chi^{(3)}(\omega,\omega,\omega)\boldsymbol{e}_1\boldsymbol{e}_1\boldsymbol{e}_1 \tag{1-84}$$

Δk is the phase mismatch factor that can be calculated by

$$\Delta k = 3k_1 - k_2 = \frac{6\pi}{\lambda_1}[n(\omega) - n(3\omega)] \tag{1-85}$$

In the case of the phase-mismatched condition, $\Delta k \neq 0$, the conservation energy is not satisfied. At the initial condition, the THG wave is zero $A_2(0) = 0$ and assumes that changing of the fundamental wave is extremely small $A_1(z) \approx A_1(0)$. The solution of the (1-84) equation is the amplitude of the THG wave

$$A_2(z) = \frac{\varepsilon_0 k_2}{2\Delta k \varepsilon(3\omega)} \chi_e^{(3)} A_1^3(0)(e^{i\Delta kz} - 1) \tag{1-86}$$

The corresponding intensity of the THG wave along the z-direction is

$$I_2(z) \propto A_2 A_2^* \propto \chi_e^{(3)} I_1^3(0) \left(\frac{sin^{\Delta kz}/_2}{\Delta kz/_2}\right)^2 \tag{1-87}$$

where $I_1(0)$ is the intensity of the initial fundamental wave as a quadratic function of amplitude $A_1(0)$. The THG intensity is proportional to the cube of the fundamental wave intensity and varies periodically along the *z*-axis as shown in Figure 6.

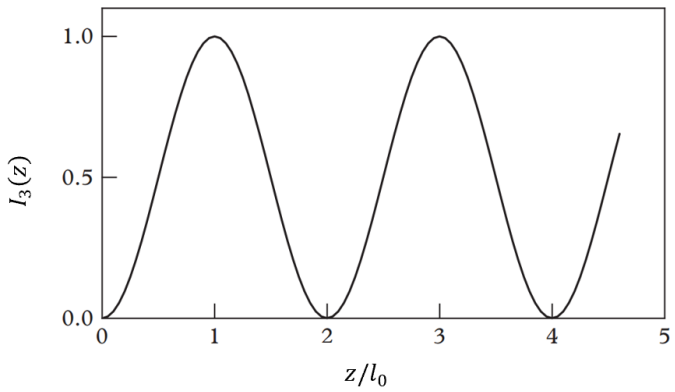

Figure 6. Variation of normalized third-harmonic intensity versus z in the condition of Δk = 0.

The coherent length of THG can be calculated by

$$l_0 = \frac{\pi}{|\Delta k|} = \frac{\lambda_1}{6|n(\omega) - n(3\omega)|} \tag{1-88}$$

$$\begin{bmatrix} P_1(3\omega) \\ P_2(3\omega) \\ P_3(3\omega) \end{bmatrix} = \frac{1}{81}\begin{bmatrix} d_{11} & d_{12} & d_{13} & d_{14} & d_{15} & d_{16} & d_{17} & d_{18} & d_{19} & d_{110} \\ d_{21} & d_{22} & d_{23} & d_{24} & d_{25} & d_{26} & d_{27} & d_{28} & d_{29} & d_{210} \\ d_{31} & d_{32} & d_{33} & d_{34} & d_{35} & d_{36} & d_{37} & d_{38} & d_{39} & d_{310} \end{bmatrix} \begin{bmatrix} E_1^3(\omega) \\ E_2^3(\omega) \\ E_2^3(\omega) \\ 3E_2(\omega)E_3(\omega)E_3(\omega) \\ 3E_3(\omega)E_2(\omega)E_2(\omega) \\ 3E_1(\omega)E_3(\omega)E_3(\omega) \\ 3E_1(\omega)E_1(\omega)E_3(\omega) \\ 3E_1(\omega)E_2(\omega)E_2(\omega) \\ 3E_1(\omega)E_1(\omega)E_2(\omega) \\ 6E_1(\omega)E_2(\omega)E_3(\omega) \end{bmatrix}$$

(1-89)

The number of elements of the fourth-rank tensor $\chi_{ijkl}^{(3)}$ depends on the material structures. For example, the isotropic material (glass, liquid, vapor), the susceptibility $\chi_{ijkl} = \chi_{ijkl}^{(3)}(\omega_4 = \omega_1 + \omega_2 + \omega_3)$ has only 21 nonzero elements and shows the following symmetry properties.

Nonlinear in the interface between two nonlinear materials

The first nonlinear optical phenomenon, the SHG process, is observed from crystallized quartz. [2] They observed the SHG signal from many other bulk materials as a current commercial nonlinear medium as potassium dihydrogen phosphate (KDP), [37] β-Barium Borate (BBO) and lithium triborate (LBO), [38] and potassium titanyl phosphate (KTP) [39]. However, many works studying the surface and bulk SHG responses together indicated that the surface and bulk responses are substantially different. [38-39] Several common interface/surface nonlinear optical phenomena such as surface second-, third-harmonic generation, and surface sum-frequency generation are used to study the properties, and electronic and crystal structures of surfaces. [42]–[46] The theory of surface nonlinear optical effects is introduced by Shen, and Lambert. [13][16][48][11][49]–[51] At the interface of two nonlinear materials, the external field interacting with the molecules of each medium having chemical structure will suddenly change the consequence of

symmetry property at the interface can be broken. The thin interface layer consists of only a single or few molecular monolayers considered a quasi-macroscopic second-order nonlinear medium. On the other hand, if the surface of the nonlinear material includes adsorbed molecules manifesting an oriented structure that consequences centrosymmetric property is locally broken. These two cases allow both SHG and SFG phenomena to happen. [51] The SHG signal was observed from anisotropic achiral surfaces originating from electric dipole to study complex chiral structures and characterize the anisotropic achiral surfaces. [52] This section presents the second-order nonlinear optical phenomenon, SHG process, generation from the interface between two centrosymmetric media. Assuming a fundamental wave has the form theoretically as $\boldsymbol{E}_i(\boldsymbol{r},t) = \boldsymbol{A}_i(\omega_i)e^{i(\boldsymbol{k}_i(\omega_i)\cdot\boldsymbol{r}-\omega_i t)} + c.c.$, when this fundamental wave interacts with the interface of a second-order nonlinear optical material, the emitted wave separate to two part of transmitted and reflected waves. The surface of a centrosymmetric nonlinear material as shown in Figure 7. [14]

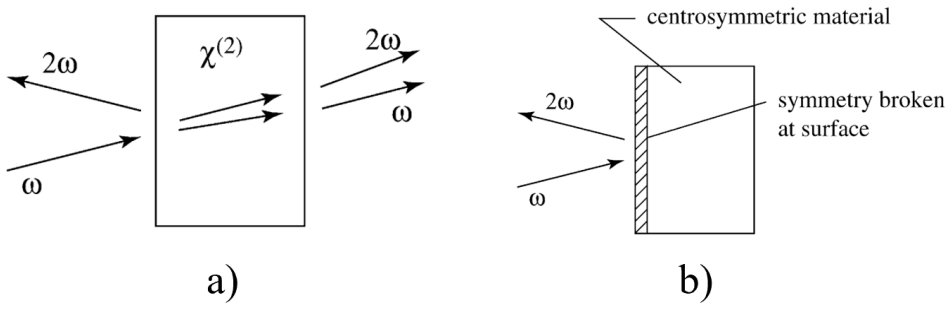

Figure 7. Reflection of second-harmonic generation light at the surface of a second-order nonlinear optical material (a) and a centrosymmetric nonlinear (b).

The electric field component of the electromagnetic wave interacts with the surface of a second-order nonlinear optical material that can be considered into two specific cases of polarized parallel and perpendicular to the plane of incidence called p-polarization and s-polarization, respectively as in Figure 8.

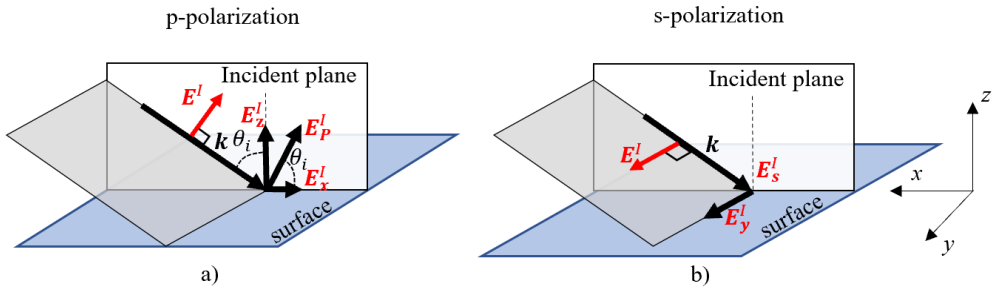

Figure 8. p- and s-polarized incident E fields. a) the p-polarization is combined from the z and x components, b) the s-polarization is only the y component, θ_i is the incident angle.

According to the separation of the electric field along the *i*-axis, the magnitude of the electric field components is calculated as

$$E_x^I = \pm E_P^I cos\theta_i \tag{1-90}$$

$$E_y^I = E_s^I \tag{1-91}$$

$$E_z^I = E_P^I sin\theta_i \tag{1-92}$$

The reflected part and transmitted part of the p- and s-polarized electric field at the interface between two nonlinear media is explained in Figure 9 and calculated using Fresnel coefficients and equations [16].

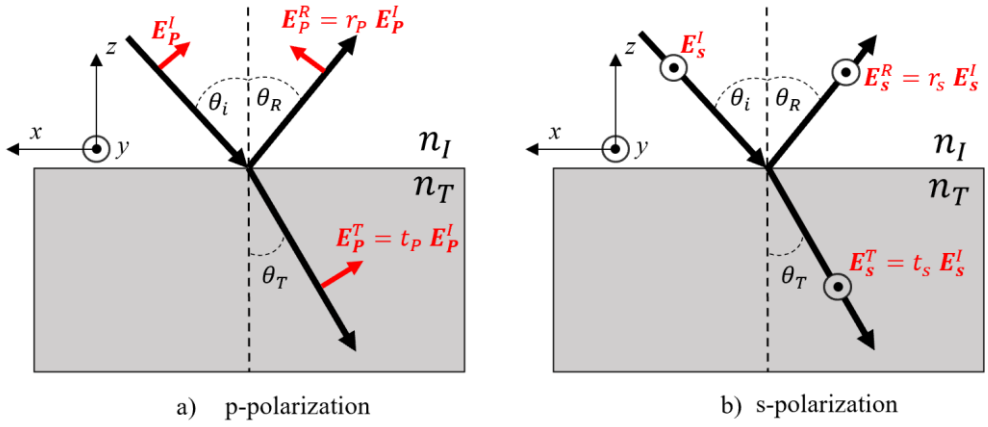

Figure 9. The reflection and transmission of an electric field at the surface of a second-order nonlinear optical material, a) p-polarization, b) s-polarization

The Fresnel amplitude coefficients for reflection and transmission in the p- and s-polarization cases

$$r_s \equiv \left(\frac{E_s^R}{E_s^I}\right) = \frac{n_I cos\theta_i - n_T cos\theta_T}{n_I cos\theta_i + n_T cos\theta_T} \tag{1-93}$$

$$r_P \equiv \left(\frac{E_P^R}{E_P^I}\right) = \frac{n_T cos\theta_i - n_I cos\theta_T}{n_I cos\theta_T + n_T cos\theta_i} \tag{1-94}$$

$$t_s \equiv \left(\frac{E_s^T}{E_s^I}\right) = \frac{2n_I cos\theta_I}{n_I cos\theta_i + n_T cos\theta_T} \tag{1-95}$$

$$t_P \equiv \left(\frac{E_P^T}{E_P^I}\right) = \frac{2n_I cos\theta_i}{n_I cos\theta_T + n_T cos\theta_i} \tag{1-96}$$

Electric fields incident at angular frequency ω from medium 1 (diffractive index n_I) induces a nonlinear source polarization at an angular frequency ω_s in both the surface and bulk region of nonlinear medium 2. The surface region consists of several atomic layers of a homogeneous material in which the normal component of the incident electric fields is discontinuous, and the layers of material are made different from the bulk by the presence of surface electronic states, defects, damage, surface adsorbates, and other deformations at the surface. The thickness of the surface is much thinner than the optical wavelength, and the radiation from the surface may be thought that from a single surface layer of nonlinear source polarization $\boldsymbol{P}_{surf}^{NL}$ - the integral of the nonlinear source polarization over the thickness of the real surface region. While the nonlinear surface polarization of the bulk region is assumed $\boldsymbol{P}_b^{NL}$ In medium 2, the bulk and surface polarizations are originated from the same incident field and the tangential component of the wave vector is conserved across the interfaces $\boldsymbol{k}_b \equiv \boldsymbol{k}_{surf}$, where $\boldsymbol{k}_b$ is the wave vector of $\boldsymbol{P}_b^{NL}$ and while $\boldsymbol{k}_{surf}$ is the wave vector of $\boldsymbol{P}_{surf}^{NL}$. The second-harmonic generation $\boldsymbol{E}(\omega_s)$ can be calculated using surface and bulk nonlinear source polarization of the form

$$\boldsymbol{P}^{NL} = \left(\boldsymbol{P}_{surf}^{NL} + \boldsymbol{P}_b^{NL}\right) e^{i(\boldsymbol{k}_s \cdot \boldsymbol{r} - \omega_s t)} \tag{1-97}$$

The x-component of all the waver vectors is constrained by the continuity of the electric field at $z = 0$ such that $k_{1,s} = k_{2,s} = k_{s,x} \equiv k_x$.

The surface nonlinear source polarization is usually expressed in a power series of the local electric field. Generally, two electric fields interact at the surface.

$$\boldsymbol{P}(\omega_s) = \chi^{(2)}_{ijk}(\omega_s = \omega_1 + \omega_2) : \boldsymbol{E}(\omega_1)\boldsymbol{E}(\omega_2) \tag{1-98}$$

If $\omega_1 = \omega_2$, the (1-98) equation becomes the second-harmonic nonlinear polarization at a surface.

$$\boldsymbol{P}(2\omega) = \chi^{(2)}_{ijk}(2\omega) : \boldsymbol{E}_j(\omega)\boldsymbol{E}_k(\omega) \tag{1-99}$$

For the surface of an isotropic medium and centrosymmetric materials, normal to the z-direction, only three independent elements tensor components are $\chi_{zzz}, \chi_{zxx} = \chi_{zyy}$, and $\chi_{xxz} = \chi_{xzx} = \chi_{yyz} = \chi_{yzy}$. Radiation from a surface layer with source polarization $\boldsymbol{P}^s e^{i(\boldsymbol{k}\cdot\boldsymbol{r}-\omega_s t)}$ and with isotropic local dielectric ε' can be calculated using the boundary conditions. [47]

$$E_P(\omega_s) = \frac{i4\pi k_1}{\varepsilon_2 k_{1,z} + \varepsilon_1 k_{2,z}} \left[k_{2,z} P_x^s + (\varepsilon_2/\varepsilon') k_x P_z^s\right] e^{i(\boldsymbol{k}_1\cdot\boldsymbol{r}-\omega_s t)}$$

$$E_s(\omega_s) = \frac{i4\pi k_1}{k_{1,z}+k_{2,z}} \left[(\varepsilon_1)^{-1} k_1 P_y^s\right] e^{i(\boldsymbol{k}_1\cdot\boldsymbol{r}-\omega_s t)} \tag{1-100}$$

In the case of $\varepsilon' = \varepsilon_1 = \varepsilon_2$, the radiation fields in equation (1-100) becomes

$$E_{P0}(\omega_s) = \frac{i2\pi k_1}{\varepsilon_1 k_{1,z}} \left[k_{1,z} P_x^s + k_x P_z^s\right] e^{i(\boldsymbol{k}_1\cdot\boldsymbol{r}-\omega_s t)}$$

$$E_{s0}(\omega_s) = \frac{i2\pi k_1^2}{\varepsilon_1 k_{1,z}} P_y^s e^{i(\boldsymbol{k}_1\cdot\boldsymbol{r}-\omega_s t)} \tag{1-101}$$

From the (1-100) and (1-101) equations, the reflected fields can be expressed as

$$\boldsymbol{E}(\omega_s) = \boldsymbol{L} \cdot \boldsymbol{E}_0(\omega_s) \tag{1-102}$$

where $\boldsymbol{L}$ is a macroscopic local field correction factor, [47] is used to calculate the radiation fields in presence of the boundary surfaces. In the inversion symmetry medium, the

second-order nonlinear optical phenomena are forbidden but allowed at the surface. This makes the reflected SHG field at the surface become highly surface specific. The reflected field from the surface is surface SHG generated by the surface nonlinear polarization $\boldsymbol{P}^s(2\omega)$

$$\boldsymbol{E}_P(2\omega) = i(4\pi\omega/c)[L_{xx}(2\omega)\chi^{(2)}_{s,xjk}L_{jj}(\omega)L_{kk}(\omega) + (k_x(2\omega))/k_{1z}(2\omega)] \times L_{zz}(2\omega)\chi^{(2)}_{s,zjk}L_{jj}(\omega)L_{kk}(\omega)]E_{1j}(\omega)E_{1k}(\omega) \quad (1\text{-}103)$$

$$\boldsymbol{E}_s(2\omega) = i(2\pi k_1^2(2\omega)/k_{1z}(2\omega)\varepsilon_1(2\omega))L_{yy}(2\omega)\chi^{(2)}_{s,yjk}L_{jj}(\omega)L_{kk}(\omega) \times E_{1j}(\omega)E_{1k}(\omega) \quad (1\text{-}104)$$

where $\boldsymbol{k}_1$ and $\boldsymbol{k}_2$ are wave vectors of reflected SHG wave into medium 1 and transmitted SHG wave into medium 2, respectively. The SHG intensity now can be calculated by

$$I(2\omega) = \frac{c\varepsilon_1(2\omega)|\boldsymbol{E}(2\omega)|^2}{2\pi} = \frac{32\pi^3\omega^2\sec^2\theta_R}{c^3\varepsilon_1^{1/2}(2\omega)\varepsilon_1(\omega)}\left|\boldsymbol{e}'(2\omega)\cdot\chi_s^{(2)}:\boldsymbol{e}'(\omega)\boldsymbol{e}'(\omega)\right|^2 I_1^2(\omega) \quad (1\text{-}105)$$

where $\boldsymbol{e}'(\sigma) \equiv \boldsymbol{L}(\sigma)\cdot\hat{\boldsymbol{e}}(\sigma)$, $\hat{\boldsymbol{e}}(\omega)$ is the unit vector describing the polarization of the field at frequency σ . The power of the reflected SHG field will be calculated by

$$\wp(2\omega) = \frac{c}{2\pi}\int|E(2\omega)|^2 dA \quad (1\text{-}106)$$

And the SHG signal at the surface will be obtained by

$$S(2\omega) \propto \left[32\pi^3\omega\sec^2\theta_R/\hbar c^3\varepsilon(\omega)\varepsilon^{1/2}(2\omega)\right]\left|\chi^{(2)}_{s,\text{eff}}\right|^2 I^2(\omega)AT \quad (1\text{-}107)$$

where $I(\omega)$, A, and T are the incident laser intensity, cross-section, and pulse width, respectively. $\chi^{(2)}_{s,\text{eff}}$ is the effective surface nonlinear susceptibility and has 27 components. However, the nonzero components of $\chi^{(2)}_{s,\text{eff}}$ dependent on the surface property of materials. For example, C_{3v}-symmetry surfaces like Si(111) surfaces with square-shaped have only

four independent non-zero components corresponding to the $[2\bar{1}\bar{1}]$-x, $[01\bar{1}]$-y, and $[111]$-z directions. [53]

$$\chi^{(2)}_{s,xxx} = -\chi^{(2)}_{s,xyy} = -\chi^{(2)}_{s,yxy}$$
$$\chi^{(2)}_{s,xxz} = \chi^{(2)}_{s,yyz}$$
$$\chi^{(2)}_{s,zxx} = \chi^{(2)}_{s,zyy}$$
$$\chi^{(2)}_{s,zzz} \tag{1-108}$$

$\chi^{(2)}_{s,\mathrm{eff}}$ has a relationship with $\chi^{(2)}_{s}$ through the macroscopic local field correction and calculated by

$$\boldsymbol{\chi}^{(2)}_{s,\mathrm{eff}} = \boldsymbol{L}^{\dagger}(2\omega) \cdot \boldsymbol{\chi}^{(2)}_{s} : \boldsymbol{L}(\omega)\boldsymbol{L}(\omega) \tag{1-109}$$

The superscript † expresses an adjoint operation, $\boldsymbol{L}$ is the tensor of a local field correction factor. The $\boldsymbol{\chi}^{(2)}_{s}$ can be deduced by measuring the surface SHG signal. Different components of the third-rank tensor $\boldsymbol{\chi}^{(2)}_{s}$ can be calculated using the different polarization combinations, polarized dependence of SHG intensity, and orientation of the surface with respect to the incident beam. Consequently, the structural symmetry of the surface and interface layer can be studied by measuring SHG and/or SFG signals. If the surface consists of the group adsorbed material. Surface nonlinear susceptibility is given by

$$\boldsymbol{\chi}^{(2)}_{s} = \boldsymbol{\chi}^{(2)}_{ss} + \boldsymbol{\chi}^{(2)}_{m} + \boldsymbol{\chi}^{(2)}_{i} \tag{1-110}$$

$\boldsymbol{\chi}^{(2)}_{ss}$ and $\boldsymbol{\chi}^{(2)}_{m}$ are the contribution from the bare substrate surface and the molecular layer isolated from the substrate, respectively. $\boldsymbol{\chi}^{(2)}_{i}$ originated from the interaction between the molecule and the substrate. Generally, the form used to calculate $\boldsymbol{\chi}^{(2)}_{s}$ reflects the structural symmetry of an interface, and is related to the number of molecules per unit area $N_s = \int f(\Omega)d\Omega$, molecular population ρ^{0}_{gg} in the ground state $\langle g|$, higher-level state $\langle n|$, $\langle n'|$, and transition parameter ω_{ng}

$$\boldsymbol{\chi}^{(2)}_{s,ijk} = \int\left\{\sum_{g,n,n'}\langle g|r_i|n\rangle\langle n|r_j|n'\rangle\langle n'|r_k|g\rangle\ \rho^{0}_{gg}A'_{nn}\right\}\int f(\Omega)d\Omega \tag{1-111}$$

$$A'_{nn} = \left(\frac{e^3}{\hbar^2}\right)\left\{\left[\left(\omega - \omega_{n'g}\right)\left(2\omega - \omega_{ng}\right)\right]^{-1} + \left[\left(\omega - \omega_{n'g}\right)\left(\omega + \omega_{ng}\right)\right]^{-1} + \right.$$

$$\left. + \left[\left(\omega + \omega_{n'g}\right)\left(2\omega + \omega_{ng}\right)\right]^{-1}\right\} \quad (1\text{-}112)$$

The real surface nonlinear susceptibility is a sum of the electric dipole arising from the structural discontinuity at the interface and the nonlocal electric quadrupole term arising from the field discontinuity at the interface. The nonzero components of $\boldsymbol{\chi}_s^{(2)}$ of various two-dimensional symmetry, classes have indicated in table 5. [47]

Table 5. Independent nonvanishing elements of $\chi_s^{(2)}(2\omega)$ for surfaces of various symmetry classes (surface is in the x-y plane)

Symmetry classes	Location of a mirror plane	Independent nonzero elements
C_1	No mirror	$xxx, xxy = xyx, xyy, yxx, yxy = yyx, yyy, xxz = xzx,$ $xyz = xzy, yxz = yzx, yyz = yzy, zxx, zxy = zyx, zyy$ $xzz, yzz, zxz = zzx, zyz = zzy, zzz$
C_{1v}	$y - x$	$xxy = xyz, yxx, yyy, xxz = xzx, yyz = yzy, zxx, zyy$ $yzz, zyz = zzy, zzz$
C_2	No mirror	$xxz = xzx, xyz = xzy, yxz = yzx, yyz = yzy, zxx, zyy$ $zxy = zyx, zzz$
C_{2v}	$x - z, y - z$	$xxz = xzx, yyz = yzy, zxx, zyy, zzz$
C_3	No mirror	$xxx = -xyy = -yxy = -yyx, yyy = -yxx = -xxy$ $= -xyx, xxz = xzx = yyz = yzy, zxx$ $= zyy, xyz = xzy = -yxz = -yzx, zzz$
C_{3v}	$y - z$	$yyy = -yxx = -xxy = -xyz, xxz = xzx = yyz = yzy$ $xxz = xzx = yyz = yzy, zxx = zyy, zzz$
C_4, C_6	No mirror	$xxz = xzx = yyz = yzy, zxx = zyy, xyz = xzy = -yxz$ $= -yzx, zzz$
C_{4v}, C_{6v} or isotropic	$x - z, y - z$	$xxz = xzx = yzy = yyz, zxx = zyy, zzz$

In centrosymmetric media the second-order nonlinear susceptibility $\chi^{(2)} = 0$ and the local response of the medium vanishes. And assuming that the material doesn't have any magnetic dipole, the second-order polarization is induced from the distribution of nonlocal responses in the following formulation.

$$\boldsymbol{P}(\omega_s) = \chi^{(2)}_{nonlocal}(\omega_s = \omega_1 + \omega_2) : \boldsymbol{E}(\omega_1)\boldsymbol{\nabla}\boldsymbol{E}(\omega_2) + \\ + \chi^{(2)}_{nonlocal}(\omega_s = \omega_2 + \omega_1) : \boldsymbol{E}(\omega_2)\boldsymbol{\nabla}\boldsymbol{E}(\omega_1) \quad (1\text{-}113)$$

where $\chi^{(2)}_{nonlocal}$ is a fourth-rank tensor with 81 independent elements and does not vanish in centrosymmetric media. Therefore, the nonlinear polarization in the bulk region, $\boldsymbol{P}_b^{NL}$, becomes the form of the (1-113) equation. When the two fundamental electric fields are the same wavelength ($\omega_1 = \omega_2 = \omega$), the $\chi^{(2)}_{nonlocal}(2\omega)$ has only fourth independent non-zero elements, the components of $\boldsymbol{P}_b^{NL}$ in cubic media is given by [11], [54]

$$\boldsymbol{P}^{NL}_{b,i}(2\omega) = (\delta - \beta - 2\gamma)(\boldsymbol{E}(\omega)\cdot\boldsymbol{\nabla})\boldsymbol{E}_i(\omega) + \beta\boldsymbol{E}_i(\omega)(\boldsymbol{\nabla}\cdot\boldsymbol{E}(\omega)) + \\ + \gamma\nabla_i(\boldsymbol{E}(\omega)\cdot\boldsymbol{E}(\omega)) + \xi E_i(\omega)\nabla_i E_i(\omega) \quad (1\text{-}114)$$

where δ, β, γ, and ξ are parameters depending on the material property known as frequency dependent. The fourth frequency $\xi = 0$ in the case of isotropic media because the result of the point product $E_i\nabla_i E_i$ is a scalar field. The (1-114) equation can be rewritten as

$$\boldsymbol{P}^{NL}_{b,i}(2\omega) = (\delta - \beta - 2\gamma)(\boldsymbol{E}(\omega)\cdot\boldsymbol{\nabla})\boldsymbol{E}_i(\omega) + \beta\boldsymbol{E}_i(\omega)(\boldsymbol{\nabla}\cdot\boldsymbol{E}(\omega)) + \\ + \left(\frac{2i\omega}{c}\right)\gamma\big(\boldsymbol{E}(\omega)\times\boldsymbol{B}(\omega)\big)_i \quad (1\text{-}115)$$

The first two-term of the (1-115) equation is usually called the electric quadrupole terms; the third term is known as the magnetic dipole. The dependent frequencies are calculated by Sudhanshu *et al.* [55], [56] at a metal surface under the handling of the conduction electrons n_c as a free electron gas with effective mass m_e^*.

$$\beta = \frac{e}{8\pi m_e^*\omega^2},\ \gamma = \frac{\beta\pi n_c e^2}{m_e^*\omega^2},\ \delta = \beta + 2\gamma \quad (1\text{-}116)$$

For homogeneous and isotropic materials, $\boldsymbol{\nabla} \cdot \boldsymbol{E} = 0$ and the $(\boldsymbol{E} \cdot \boldsymbol{\nabla})\boldsymbol{E}$ term is also zero because the incident fields are plane waves with the same wavelength ω. Then, the bulk contribution to the nonlinear polarization becomes.

$$\boldsymbol{P}_{b,i}^{NL}(2\omega) = \gamma \boldsymbol{\nabla}\big(\boldsymbol{E}(\omega) \cdot \boldsymbol{E}(\omega)\big) \tag{1-117}$$

The bulk nonlinear polarization source is much less attention and is neglected usually in studying the structural surface of materials. In order to separate the contribution of bulk and surface nonlinear polarization sources, two incident beams focus on the surface of nonlinear material from two different incident angles θ_{i1} and θ_{i2}. [40] Wang *et al.* calculated the s-polarization SHG signals from the effective surface and bulk contributions and are given by

$$E_{s,surff} \propto \chi_{xxz}^{C,eff}\left(E_{1,P}E_{2,s} + \frac{sin\theta_{i2}}{sin\theta_{i1}}E_{1,s}E_{2,P}\right) \tag{1-118}$$

$$E_{s,bulk} \propto i\delta'(E_{1,P}E_{2,s} - E_{1,s}E_{2,P}) \tag{1-119}$$

where $\chi_{xxz}^{C,eff}$ is the effective conventional (C) surface tensor $\chi_{zzz}^{C,eff} = \chi_{zzz}^{C} + \gamma/\varepsilon(2\omega)$, $\chi_{zxx}^{C,eff} = \chi_{zxx}^{C} + \gamma/\varepsilon(2\omega)$, and $\chi_{xxz}^{C,eff} = \chi_{xxz}^{C}$. The material parameter $\delta' = \delta - \beta - 2\gamma$.

SSHG originates from the surface nonlinear polarization contribution of the electric dipole and bulk nonlinear polarization contribution of the electric quadrupole. Therefore, SSHG can be used to study the surface's characterization by using surface electronic spectra. However, SSHG cannot give information about vibrational spectra at the surface. In order to solve this task, surface sum-frequency generation (SSFG) with an excitation beam in the infrared-visible (IR-vis) region corresponding to the vibrational frequency of specific material is appropriated. The SSFG susceptibility is studied and expressed in more detail by Lambert *et al.* [16] Two incident electric fields at frequencies ω_1 and ω_2 illustrate into the surface of a nonlinear material (or interface between two centrosymmetric materials) at incident angle θ_1 and θ_2, respectively. The sum-frequency generation at a

frequency $\omega = \omega_1 + \omega_2$ will appear in both reflected and transmitted directions with angles θ_R and θ_T, respectively. The electric boundary condition at the surface (z= 0) induces the wave vector parallel components of incident and emitted fields satisfied the matching condition: $k_{1\parallel} + k_{2\parallel} = k_{SF\parallel}$.

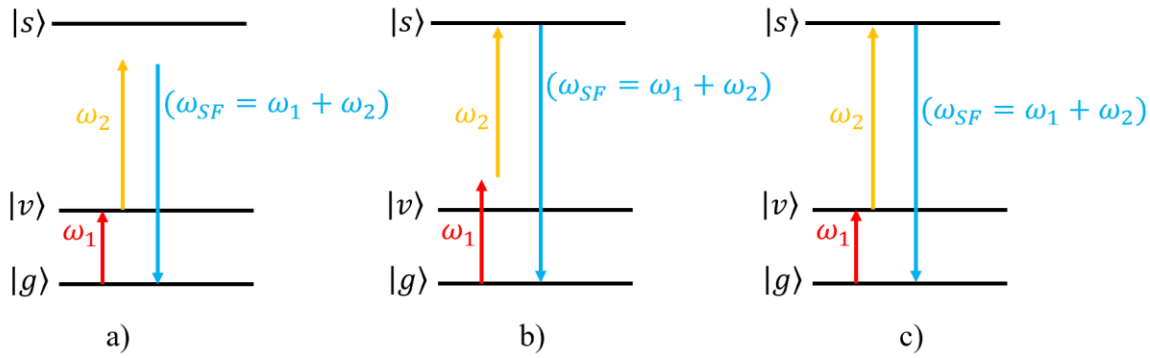

Figure 10. Description of level energy diagram of resonant SFG with (a) ω_1 on resonance, (b) $\omega_1 + \omega_2$ on resonance, and (c) both ω_1 and $\omega_1 + \omega_2$ on resonances.

If the SSFG happens at the interface (z = 0) between two semi-infinite, the bulk and surface nonlinear optical polarization sources will contribute to the SSFG signal. Assuming the dielectric constants of two media I and II are ε_1 and ε_2, respectively. $\chi_b^{(2)}$is the bulk nonlinearity of medium II. These parameters of the interface are ε' and $\chi_s^{(2)}$due to the significantly different structure from the bulks. The bulk nonlinear polarization in medium II is given by

$$\boldsymbol{P}_b^{(2)} = \chi_{\mathrm{b}}^{(2)} : \boldsymbol{E}_1^{II}(\omega_1)\boldsymbol{E}_2^{II}(\omega_2)$$
$$= \chi_{\mathrm{b}}^{(2)} \boldsymbol{A}_1^{II}(\omega_1)\boldsymbol{A}_2^{II}(\omega_2) e^{i[(k_1^I + k_1^{II})\cdot \boldsymbol{r} - (\omega_1+\omega_2)t]} \quad (1\text{-}120)$$

At the thin interfacial layer (z = 0), the nonlinear polarization is given by

$$\boldsymbol{P}^{(2)} = \delta(z)\chi_{\mathrm{s}}^{(2)} \boldsymbol{A}_1^0(\omega_1)\boldsymbol{A}_2^0(\omega_2) e^{i[(k_1^0 + k_2^0)\cdot \boldsymbol{r} - (\omega_1+\omega_2)t]} \quad (1\text{-}121)$$

The SFG field originates from the nonlinear bulk and the interfacial layer is calculated by

$$\boldsymbol{E}(\omega_{SFG}) = \boldsymbol{E}_b(\omega) + \boldsymbol{E}_s(\omega) \quad (1\text{-}122)$$

where

$$\boldsymbol{E}_s(\omega) = \frac{i2\pi\omega^2}{c^2 k_z}\boldsymbol{p}_s e^{i(\boldsymbol{k}\cdot\boldsymbol{r}-\omega t)} \tag{1-123}$$

The expression of $\chi_s^{(2)}$ and $\chi_b^{(2)}$ [57] is given by

$$\begin{aligned}\chi^{(2)}_{S,ijk} = \int_0^{0+} \Big[& f_i(\omega,z)\chi^{(2)}_{d,ijk}(z) f_j(\omega_1 z) f_k(\omega_2 z) \\ & + \frac{\partial}{\partial z} f_i(\omega,z)\chi^{(2)}_{q,zijk}(z) f_j(\omega_1,z) f_k(\omega_2,z) \\ & + f_i(\omega,z)\chi^{(2)}_{q1,izjk}(z)\frac{\partial}{\partial z} f_j(\omega_1,z) f_k(\omega_2,z) \\ & + f_i(\omega,z)\chi^{(2)}_{q2,ijzk}(z) f_j(\omega_1 z)\frac{\partial}{\partial z} f_k(\omega_2 z)\Big] dz \\ \equiv \chi^{(2)}_{Sd,ijk} + & <\hat{z}\cdot\vec{\chi}^{(2)}_{q\alpha,ijk}>_{\mathrm{Int}} \\ \chi^{(2)}_{B,ijk}\left(\vec{k}\neq\vec{k}_1+\vec{k}_2\right) = \chi^{(2)}_{d,ijk} & - i\vec{k}\cdot\vec{\chi}^{(2)}_{q,ijk} + \vec{\chi}^{(2)}_{q1,ijk}\cdot i\vec{k}_1 + \vec{\chi}^{(2)}_{q2,ijk}\cdot i\vec{k}_2\end{aligned} \tag{1-124}$$

$f_x(\Omega,z) = f_y(\Omega,z) = 1$, $f_z(\Omega,z) = \varepsilon(\Omega,z)/\varepsilon_2(\Omega)$, $\chi_{sd}^{(2)}$ is the susceptibility from electric dipole (ED) due to the lack of inversion symmetry of the interface layer, $\chi_{qi}^{(2)}$is the susceptibility from electric quadrupole (EQ) due to field variation resulting from the change of the dielectric constant at the interface. $\chi_s^{(2)}$ used to study the interface determining nonzero and independent elements of $\chi_s^{(2)}$. For example for a *C4v* interface, the nonzero elements are $\chi_{s,zzz}^{(2)}$, $\chi_{s,zxx}^{(2)} = \chi_{s,zyy}^{(2)}, \chi_{s,xzx}^{(2)} = \chi_{s,yzy}^{(2)}, and\ \chi_{s,xxz}^{(2)} = \chi_{s,yyz}^{(2)}$. In the case of no inversion symmetry existing inside of the bulk, the amplitude of $\chi_b^{(2)}$ is allowed by electric dipole and much larger than $\chi_s^{(2)}$. In the inverse case, $\chi_b^{(2)}$ is electric dipole is forbidden and they obtain the ratio $\left|\frac{\chi_b^{(2)}}{\Delta k_z^{II}}\right| / \left|\chi_s^{(2)}\right| \sim \left|\frac{k^{II}\chi_q^{(2)}}{\Delta k_z^{II}\chi_s^{(2)}}\right|$. For reflected SFG, $|(\Delta k_z^{II})_R| \geq |k^{II}|$, surface nonlinear polarization source becomes the main contribution of SFG response and $\left|\chi_s^{(2)}/\chi_q^{(2)}\right| > 1$ allowing SFG measurement to characterize the surface using

both ω_1 and $\omega_1 + \omega_2$ on resonances in which a tunable IR pulse is scanned to match the vibrational frequency of atoms, and molecules. The sum-frequency vibrational spectroscopy (SFVS) uses a continuously tunable IR pulse as a pump source with a visible pulse. The signals show the vibrational spectra of absorbed molecular monolayers equal to the IR spectra. The SFVS spectra reflect the molecular orientation, conformational change of polymer chains, and vibrational spectra of liquid interfaces. The efficient nonlinear susceptibility of reflected surface SFG $\left(\left|\chi^{(2)}_{s,eff}\right|\right)$ is measured using the phase sensitive SFVS technique for the imaginary part of $\chi^{(2)}_{s,eff}$.

$$\chi^{(2)}_{\mathrm{s},eff}(\omega_{IR}) = \chi^{(2)}_{\mathrm{NR}} + \int \frac{A(\omega_q)\rho(\omega_q)}{\omega_{IR} - \omega_q + i\Gamma_q} d\omega_q$$

$$Im\chi^{(2)}_{\mathrm{s},eff}(\omega_{IR}) = \pi A(\omega_q)\rho(\omega_q) \qquad (1\text{-}125)$$

$\chi^{(2)}_{\mathrm{NR}}$, $A(\omega_q)$, ω_q, and Γ_q are the non-resonant susceptibility part, and the amplitude, frequency, and damping constant of the q-th vibrational resonance, respectively. $\rho(\omega_{IR})$ is the density of modes at the input IR frequency. Nonzero elements of nonlinear susceptibilities of surface (table 6) are measurements applying the circular intensity difference and linear intensity difference for different surface symmetries and beam polarizations. [58], [59]

Table 6. Independent Nonvanishing Elements of χ^2 ($\omega_s = \omega_1 + \omega_2$) of various surface symmetries in the electric dipole approximation

Group Symbols Schönflies	Orientation of Symmetry Axes	Nonvanishing Independent Tensor Elements	
		Achiral	Chiral
C_1	any	all 27 elements are nonvanishing and independent	
C_s	$\bar{2}\|y$	$xxx,\ xxz,\ xzx,\ xyy,\ xzz,\ yxy,\ yyx,$ $yyz,\ yzy,\ zxx,\ zxz,\ zzx,\ zyy,\ zzz$	–
C_2	$2\|z$	$xxz,\ xzx,\ yyz,\ yzy,\ zxx,\ zyy,\ zzz$	$xyz,\ xzy,\ yxz,\ yzx,\ zxy,\ zyx$
C_{2v}	$\bar{2}\|x, \bar{2}\|y$	$xxz,\ xzx,\ yyz,\ yzy,\ zxx,\ zyy,\ zzz$	–
C_3	$3\|z$	$xxy = xyx = yxx = -yyy,$ $xyy = yxy = yyx = -xxx, xxz = yyz,$ $xzx = yzy, zxx = zyy, zzz$	$xyz = -yxz, xzy = -yzx, zxy = -zyx$
C_{3v}	$3\|z,\ \bar{2}\|y$	$xyy = yxy = yyx = -xxx,$ $xxz = yyz, xzx = yzy, zxx = zyy, zzz$	–
$C_4;C_6;C_\infty$	$4\|z;\ 6\|z;\ \infty\|z$	$xxz = yyz, xzx = yzy, zxx = zyy, zzz$	$xyz = -yxz, xzy = -yzx, zxy = -zyx$
$C_{4v};C_{6v};C_{\infty v}$	$4\|z,\ \bar{2}\|y;\ 6\|z,\ \bar{2}\|y;$ $\infty\|z,\ \bar{2}\perp y$	$xxz = yyz, xzx = yzy, zxx = zyy, zzz$	–

1.2. Nonlinear optical microscopy for the bio-material study

Atoms and molecules can easily absorb photon energy because the weakest bond electrons are delocalized and thus interact with the electromagnetic field. Nonlinear optical (NLO) microscopy is one of the most art-of-modern technologies to study the physio-pathological processes in live samples because of its non-destructive investigation, selective location, and sensitive measurement. NLO such as two-photon excitation fluorescence (2PEF) experimental observed first time in 1961, [60] second and third-harmonic generation (SHG, THG), and coherent Raman scattering (CRS) (Figure 11) are thought to be the techniques most suitable for the biological applications. [61]–[67]

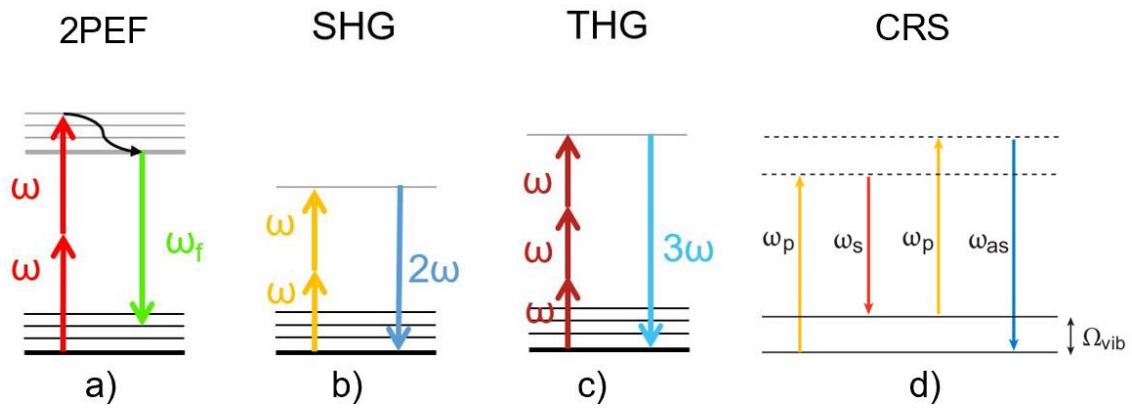

Figure 11. Energy level diagram of (a) two-photon excited fluorescence (2PEF), (b) second harmonic (SHG), (c) third harmonic (THG) generation, and (d) coherent Raman scattering (CRS).

The development of the femtosecond laser allows NLO microscopy to be conducted in biological laboratories and clinical environments. The application of NLO microscopy has resulted in many important experimental studies in the imaging of living cells, tissues, embryos, and organisms. Two-photon excitation microscopy produces deep tissue imaging and spectroscopy due to its enhanced confinement of the focal volume, the deeper penetration of the near-infrared radiation, and the reduced phototoxicity of the pulsed infrared radiation are all exploited. NLO microscopy includes multiphoton excitation microscopes that have advantages such as less photodamage and more spatial resolution than the other technique (confocal microscopy). Figure 11 shows the two-photon excitation (2PE) processes applied to microscopy to study various materials in many fields.

Properties of two-photon excitation microscopy (2PEM)

(1) One of the most crucial features of 2PEM is the limitation of fluorescence excitation within an extremely femtoliter size focal volume. The incident laser source interacts with the material at the focal plane where two-photon-induced absorption occurs with the highest and is proportional to the square of incident laser intensity. Since femtosecond pulsed laser is used in a two-photon excitation microscopy, emitted light is generated at the vicinity of the focal spot by absorbing two photons (Figure 12 (b)). It is an outstanding advantage of 2PEM over the one-photon excitation microscopy (OPEM) case because of the wider point spread function (PSF) of the 2PEM.

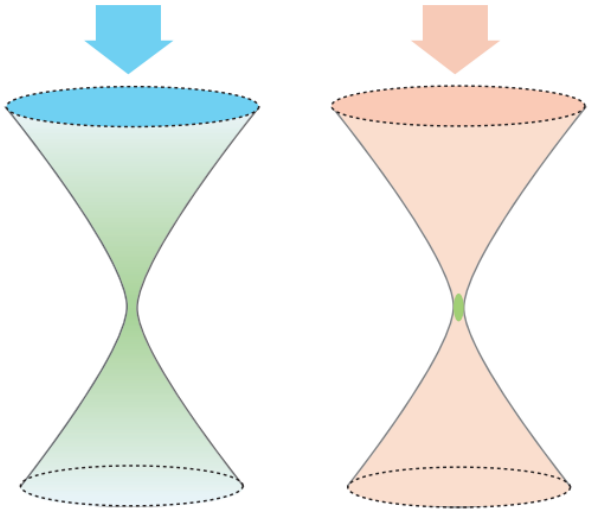

a) b)

Figure 12. Spatial confinement of signal generation with nonlinear excitation. a) one-photon process, b) two-photon process

The contribution of fluorescence at a given z-plane follows the PSF. [68] Total fluorescence generating equal fluorescence intensity is constant without depth discrimination in the one-photon case. In the two-photon case, the integrated intensity decreases rapidly away from the focal plane as shown in Figure 12. The localized excitation volume has other crucial consequences: (i) reducing the region of photo-interaction leads to a significant decrease in total specimen photobleaching and photodamage, (ii) photo-initiated chemical reaction can be locally triggered in 3-D-resolved volumes.

(2) Biological samples reduce scattering and absorption in the NIR region more than UV or blue-green light. The NIR light being used in 2PEM is able to image thick biological specimens. Comparing the scattering event between the two-photon and one-photon transition in equivalent wavelengths, the scattered light of 2PE is much smaller than OPE, and 2PE's cross-section is inversely proportional to the fourth power of

wavelength. It is able to create the advantage of deeper penetration of the excitation source into the scattering samples.

(3) High signal-to-background ratio fluorescence detection: in the OPEM case, the limitation of reduction in microscopy sensitivity is because of the excitation wavelength spectrally close to the fluorescence emission band. In contrast, the excitation and emission bands have a far spectrally distance and can approximately remove the excitation from the emission band. The 2PEM is highly efficient in the elimination of the excitation and minimum attenuation of the signal.

4) A wider gap between excitation and emission makes it easier to reject excitation light, with minimal loss of emission photons.

5) The flip side of the fact that photodamage takes place only in a very small volume, is the inherent capacity to cause photochemical reactions, for example, chemical photoactivation, or to be used for activation of optogenetic 'switches', in targeted sub-femtoliter volumes with high localization precision.

2PEM microscopy configuration

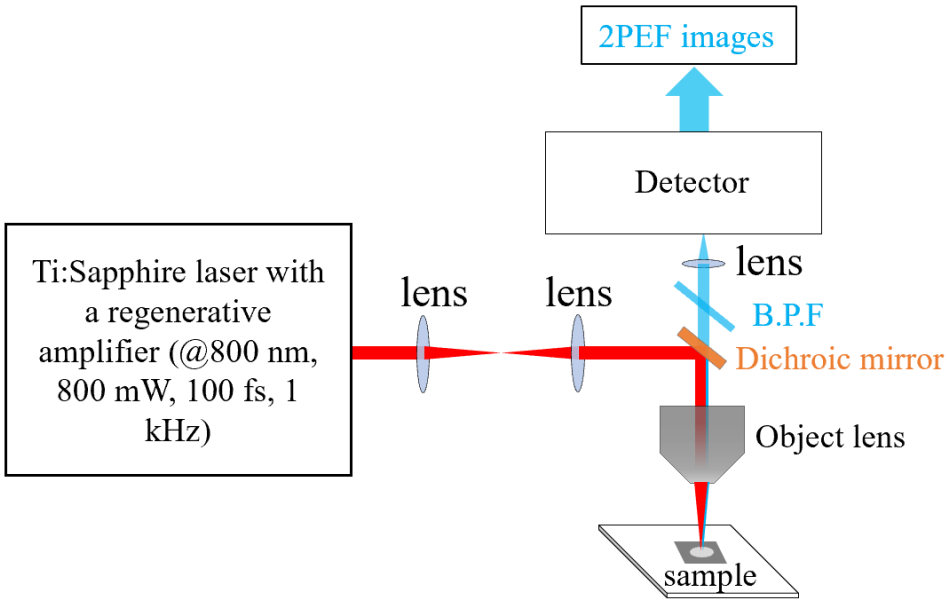

a)

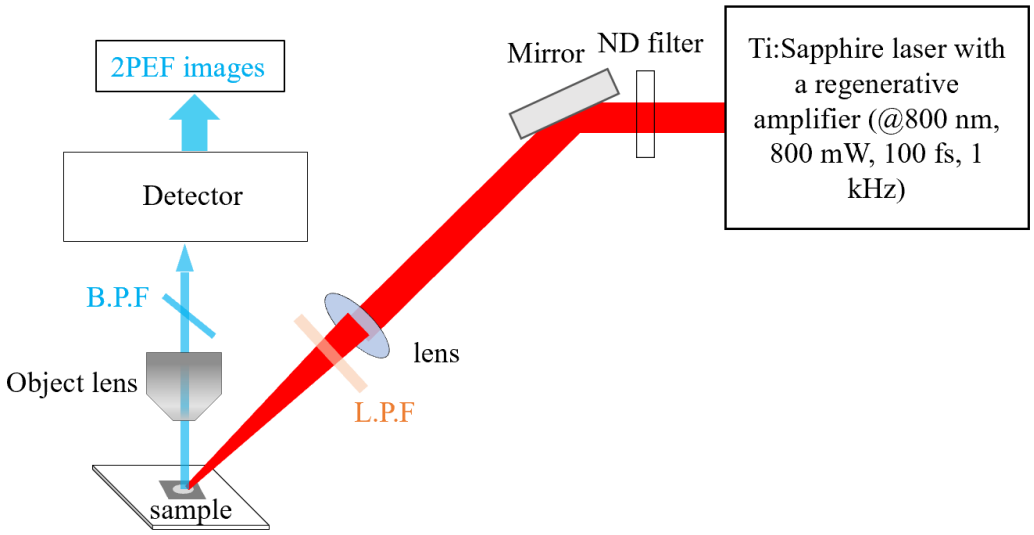

b)

Figure 13. 2PE microscope setup, a) collinear configuration, b) noncollinear configuration

2PEM microscopy is used to observe numerous biological samples and provides imaging penetration depth because the dependence of fluorophore excitation on the second power of laser light intensity confines photon absorption to a narrow region at the plane of focus, where photon flux is highest.

Figure 13 shows the 2PE microscopy setup in which the collinear configuration (Figure. 13 (a)) is the most populated and adapted confocal microscope for 2PE microscopy. [61], [69]–[73]

Two-photon excitation source

In 2PE microscopy, generated signals pass through the objective lens. The two-photon absorption and generating efficient emission are typically achieved using an ultrashort pulsed laser source. The number of photons absorbed per fluorophore per pulse is given by

$$n_a \approx \frac{p_0^2 \delta}{\tau_p f_p^2} \left(\frac{(NA)^2}{2hc\lambda} \right)^2 \qquad (1\text{-}126)$$

where p_0 is the average laser intensity. h and c are Planck's constant and the speed of light. The (1-126) gives the contribution of numerical aperture *NA* and the pulse width of the

laser source. Commonly available femtosecond laser for microscopy in general and 2PEF microscopy in specific is titanium-sapphire laser system (100 fs, 700 – 1000 nm, 1 kHz – 80 MHz), Cr-LiSAF and pulse-compressed Nd-YLF lasers. The average power of a pulsed laser can be used in the range of a few milliwatts for live samples to several hundred milliwatts for non-living materials.

Detectors

In various studies, the 2PEM shares the same optical elements and same detection system as a confocal microscope or noncollinear configuration. The photomultiplier tube (PMT) is often used in previous studies due to its high sensitivity and low cost. The PMT can convert an incident photon into a photo-electron at the photocathode. [74]–[77] The PMT's continuing superiority stems from three main features: (i) large sensing area, (ii) ultra-fast response and excellent timing performance, and (iii) high gain and low noise. Light is absorbed on a photocathode and generates free photoelectrons (external photoelectric effect). The electrons are subsequently accelerated with a high voltage (hundreds of volts) to a first dynode (an electrode), where they generate several secondary electrons. Those are accelerated towards further dynodes, where the number of electrons is getting several times larger each time. Finally, a strongly amplified photocurrent is collected with an anode near the last dynode. The newest development of photocathode PMT uses GaAsP semiconductor material improving quantum efficiency and short transit time spreads.

The Image Intensifier-Charge Coupled Device (II-CCD) camera is also used as a detector device in the microscope system in general and in the 2PEF microscope system in specific. The II-CCD cameras contain millions of photodiodes, which each have semiconductor sensors that convert light into electrical current. These offer low noise,

rapid frame rates, wide dynamic range, high resolution, and a large field of view simultaneously.

1.2.1. Two-photon excitation fluorescence (2PEF) microscopy

Two-photon excitation fluorescence (2PEF) is a nonlinear optical three-wave process, [78] nonlinear material simultaneously absorbers two incident photons and generates a new photon with smaller energy than the total energy of two incident photon energy as shown in Figure 14. In 1961, the first fluorescence light at a wavelength of 425 nm was generated from the crystal of CaF_2:Eu^{2+} using an excitation laser beam at a wavelength of 694.3 nm. [60] The principle of 2PEF microscopy originates from the two-photon absorption (2PA) and two-photon excited emission (2PEE) processes that involve the electrical and vibrational state of the molecules and/or atoms. The energy of two incident photons approximately matches the energy difference between the excited state and the ground state. The excitation of molecules from the ground state to the highly excited state by absorbing two-photon energy will take place around the attosecond ($\sim 10^{-18}$ second). From there, the molecules undergo a lost energy process by internal conversion to transit to the lowest vibrational level of the first excited state. For a while on the nanosecond scale, most molecules come back to the ground state without emitting a photon. However, in some cases, the transition of electrons back to the ground state could give an emitted photon. This emitted photon is known as the fluorescence photon with photon energy lower than the energy of the incident photon. On the other hand, there is also the other transition that emits the phosphorescence light as shown in Figure 12. [79]–[82] Today, the vast majority of multi-photon microscopy (MPM) uses the pulsed laser in the near-infrared (NIR) region (mode-locked titanium sapphire lasers Ti: sapphire, Ti: Al_2O_3) as an excitation source [83] [84] allowing 2PEE in the visible region, and three-photon excited

emission (3PEE) into the deeper ultraviolet (UV). Applying the femtosecond pulsed laser into the NLO microscopy technique, in general, had much improved the two-photon rate because of the proportion to the square of the incident photon flux. The local photon flux strongly influences the rate of reaction of photons and materials. A high reaction rate is recorded when the photons concentrate at the focal point both temporally and spatially. The temporal condition is satisfied using the mode-locked laser technique, while the spatial is by focusing through an objective lens of a microscope.

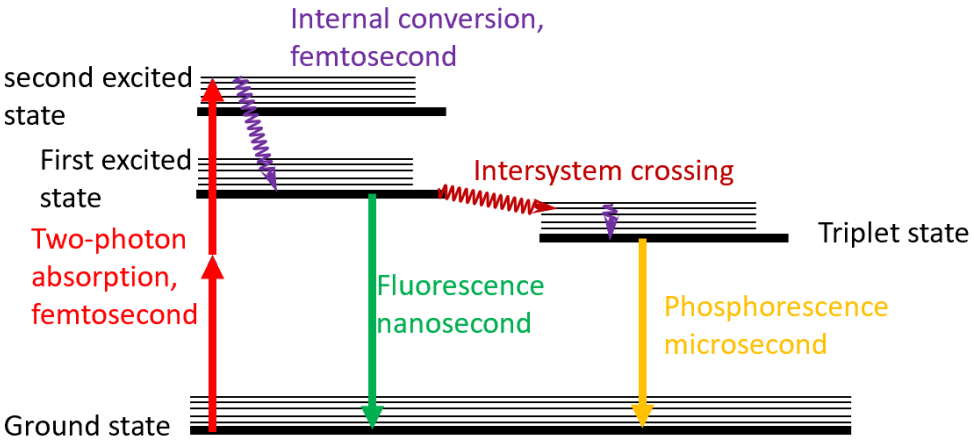

Figure 14. Jablonski diagram of two-photon excitation

The molecular ability of the TPA process is reflected by the TPA cross-section δ and can be calculated by.

$$\delta = \frac{h\nu}{N_0} = \frac{10^3 h\nu\beta}{N_A C} \tag{1-127}$$

where N_0 is the number density of absorption centers, N_A is the Avogadro constant, C is the solute molar concentration, and β is the value of the two-photon absorption coefficient. Considering the 2PA process, the average ($\langle\ \rangle$) rate over time of generated fluorescence photons is proportional to the average square of the instantaneous incident light intensity $I(\boldsymbol{r}, t)$.

$$\langle n_F(\boldsymbol{r})\rangle \propto \delta C \langle I(\boldsymbol{r}, t)^2\rangle \tag{1-128}$$

The source is a pulsed laser with parameters such as average power of laser ***P(r)***, pulse length τ, and repetition frequency *f*. The average rate of generated fluorescence photons over an interaction area (*A*) is

$$\langle n_F(\boldsymbol{r})\rangle \propto \delta C \frac{P(\boldsymbol{r})^2}{A^2 f \tau} \tag{1-129}$$

Disadvantages of 2PEFM

Obviously, the resolution of a microscope system is inversely proportional to the wavelength of light used. So, for a given fluorophore, as two-photon excitation uses approximately twice the one-photon wavelength, the result will be approximately half the resolution.

Understandably, two-photon microscopy has become especially popular with researchers wanting to observe cells in tissue cultures (for example, in organotypic brain slice cultures, which can be around 300 μm thick) or even peek into the living brains of anesthetized animals. A small piece of bone is replaced with a cover glass, which is sealed permanently in place using dental acrylic, thus creating an imaging window with a large field of view, which can be visited repeatedly.

Under optimal conditions, imaging can be extended to several hundred micrometers depth, typically 6-fold deeper than confocal microscopy, for a given sample and fluorophore. Imaging of mouse cortical vasculature has been achieved in vivo with a record imaging depth of 1.6 mm. [85] The absorption is much less compared to one-photon excitation. This leads very often too high intensities which can destroy the cell (boiling)

The 2PEFM is a non-coherent process, so the emitted fluorescence light isotropically scatters and has a broad, sample-dependent spectrum.

1.2.2. Harmonic generation microscopy

The second-order symmetry of SHG imposes restrictions on active molecular arrays and requires the nonlinear materials to be non-centrosymmetric at the excitation wavelength scale. SHG signals occur because of induced nonlinear polarization instead of absorption phenomena. The SHG signal expresses a well-dependence polarization that anisotropic properties have used to determine the hierarchical organization of crystal-like structures, oriented structures, and proteins in tissues. Therefore, the scattering nature of the SHG signal drives its intensity emission within a preferential direction. Imaging microscopy that uses harmonic generation provides enhanced transverse and longitudinal resolution. The harmonic generation is selected at the focus region of the objective lens and hence improves the resolution. An advantage to the 2PEF, the SHG is an energy conservation process. SHG process is specifically appropriate to biological materials because of their highly polarized, ordered, and large noncentrosymmetric structures. Therefore, SHG microscopy can image surface potentials without phototoxicity effects or photobleaching limited in 2PEF microscopy. [86]

The interaction between external electric field ($\vec{E}$) and the molecule of biomaterial is described by dipole moment.

$$\vec{\mu} = \vec{\mu}_0 + \alpha \cdot \vec{E} + \frac{1}{2}\beta : \vec{E}\vec{E} + \frac{1}{6}\gamma : \vec{E}\vec{E}\vec{E} + \cdots \quad (1\text{-}130)$$

where $\vec{\mu}_0$ is the permanent molecular dipole, α is the molecular polarizability, β is a tensor describing the first hyperpolarizability term that governs the SHG, and γ is the second hyperpolarizability term that drives THG and 2PEF processes. [11], [87], [88] The third term of the (1-130) equation gives information on the second-order process that depends on the hyper-Rayleigh scattering (HRS). In order to generate the SHG signal in the biomaterial, the value of β has to be nonzero which equals an asymmetry of charge

distribution. The asymmetry involves the donor (D) and acceptor (A) electron moieties producing induced electron oscillation that generates a double-frequency light. In contrast, a Rayleigh scattered light at the same frequency as the incident light happens in a symmetric dipole. [89] If molecular dipoles are parallel to each other, the SHG signal will be enhanced and be zero in versa.

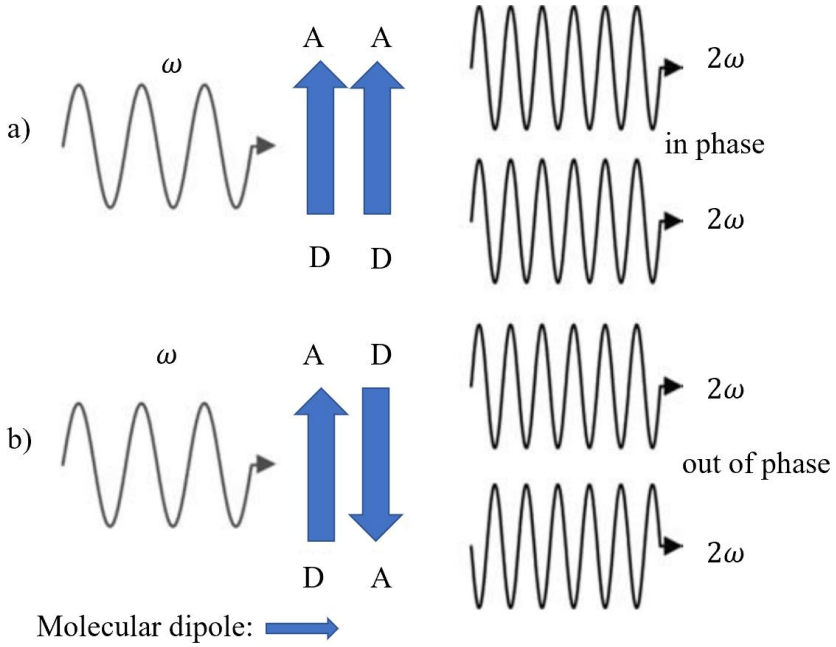

Figure 15. The constructively and destructively interfere with the SHG signal in the parallel (a) and antiparallel (b) configurations of the molecular dipoles, respectively.

Figure 15 shows the enhancement of the SHG signal that results from the in-phase of HRS and the cancellation of the SHG signal due to the out-of-phases of HRS. Therefore, the total SHG signal intensity of material includes a population of N molecules not only depending on the SHG intensity of an individual molecule but also the oriented structure of N molecules. The molecular nonlinear optical properties are characterized by a third-order tenser $\boldsymbol{\beta}^{(2)}$ in which the SHG intensity in the *i*-axis is driven by the magnitude of β_{ijk} element describing the efficiency of generating *i*-polarized SHG. SHG microscopy has been used to study most naturally formed biopolymer assemblies, lipid bilayers, fibrous

tissues, and fibrils (collagen, myosin, tubulin, cellulose) that express local uniaxial symmetry. The elements of the tensor β_{ijk} reduces to the four nonzero elements in the uniaxial system: β_{zzz} , $\beta_{zxx} = \beta_{zyy}$, $\beta_{xzx} = \beta_{yzy} = \beta_{xxz} = \beta_{yyz}$, and $\beta_{xyz} = \beta_{xzy} = -\beta_{yxz} = -\beta_{yzx}$.

The first application of SHG to study biomaterials or a living cell is conducted by I. Freund et al. [66] He used scanning SHG microscopy to observe the polarity of the rattail tendon (RTT) and indicate the oriented structures also generate the SHG signal. The SHG microscopy measurements are considered to provide prediction and analysis at the molecular level from polarization-dependent images. The origin of the SHG signal in tissue reflects polarization properties and has been demonstrated [90]–[92] to study the polarization-dependence of generated SH signals on the fundamental excitations. Using femtosecond laser pulses as an excitation source of SHG microscopy, Gauderon et al. have conducted a three-dimensional imaging technique. [93]

The third-harmonic generation (THG) has also been used in nonlinear microscopy for imaging applications. Live neurons in cell culture are depth-resolved imaged by laser scanning THG microscopy. [94] THG microscopy is particularly suitable for studying transparent samples and is non-limited to noncentrosymmetric media like SHG microscopy. [62] The difference in multi-harmonic generation (MHG) intensities come from a different location in the sample. It can be solved using the laser scanning technique producing large MHG images of biosamples.

The molecular harmonic scattering cross-section of a microscopy system is given by

$$\delta_{SHG} = \frac{4\hbar\omega^5}{3\pi n\varepsilon_0^3 c^5}|\beta|^2 \qquad [\mathrm{m}^4(\mathrm{photon/s})^{-1}] \qquad (1\text{-}131)$$

$$\delta_{THG} = \frac{3\hbar^2\,\omega^6}{2\pi n^2\varepsilon_0^4 c^6}|\gamma|^2 \qquad [\mathrm{m}^6(\mathrm{photon/s})^{-2}] \qquad (1\text{-}132)$$

In the multi-harmonic generation (MHG) processes, the cross-section (δ_{mHG}) is much smaller than those (δ_{2PEF}) in the 2PEF. However, δ_{mHG} can be enhanced by exciting molecules at near resonance. Therefore the δ_{mHG} is proportional to the N as a quadratic function while the δ_{mHG} is linearly proportional to N.

1.2.3. Raman scattering microscopy

Raman scattering microscopy (RSM) is a powerful approach for label-free, chemically specific imaging since it unveils the characteristic intrinsic vibrational contrast of molecules, a fundamental interaction in materials. RSM has been widely used to visualize the spatial and temporal evolution of a broad spectrum of materials: polymers, ceramics, 2D material, and biomaterials. The Raman scattering effect is experimentally discovered by Raman and Krishnan in 1928. [95] A monochromatic incident light of frequency ω_f interacts with molecules and gives scattered light containing the Rayleigh component (same frequency as the incident light) and shifted bands (Raman scattering). Raman shifts include the Stokes band (red-shifted frequency) and the anti-Stokes band (blue-shifted frequency). The shifted frequencies $\pm\omega_{osc}$ correspond to characteristic frequencies of molecular motions (oscillation frequencies). Therefore, Raman scattering can be used to study and characterize molecules. The materials' absorbed energy from incident photon energy depends on the (ro-) vibrational frequencies of each molecule. All molecules have specific Raman frequencies, typically given in wavenumbers, which span from 100 cm^{-1} to 3500 cm^{-1}.

There are many types of Raman spectroscopy techniques including spontaneous Raman (SR), stimulated or coherent Raman scattering (S/CRS), and coherent anti-Stokes Raman scattering (CARS)… shown in Figure 16.

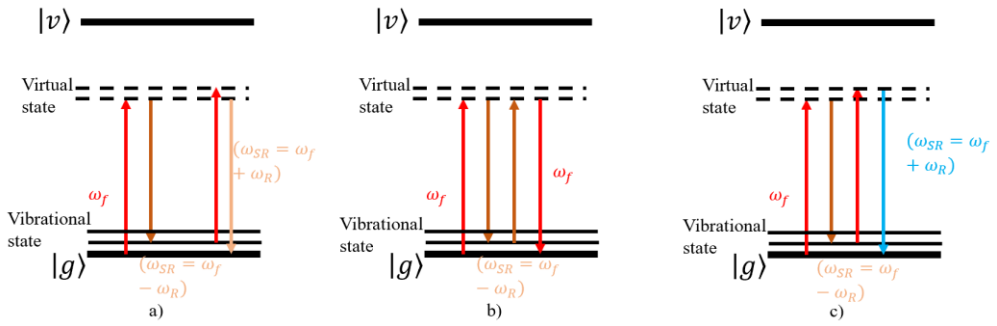

Figure 16. Energy diagrams of Raman interactions: (a) Spontaneous Raman (SR), (b) SRS, and (c) CARS.

Spontaneous Raman scattering microscopy

Figure 16 (a) shows the SR scattering with the Stokes and anti-Stokes sidebands in which their scattered photon energies are lower and higher than the incident photon energy of vibrational energy, respectively. The pump field of SR is inelastically scattered off molecular vibrations of the sample. The spontaneous Raman scattering (SR) phenomenon generates a feeble signal with less than 10^{-6} percent of incident light distributed to the spontaneous Raman scattering. Because the transition from the virtual state to the final state can take place at any time, SRS is an incoherent process. The scattered light of SR has isotropic properties and occurs only in molecules in which the applied field brings about a polarizability change along the nuclear mode. The external electric field – molecules interaction induces a dipole moment. [89]

$$\mu(t) = \alpha(t)\boldsymbol{E}(t) \tag{1-133}$$

where $\alpha(t)$ is the polarizability of molecules as a function of the nuclear coordinate $Q(t) = 2Q_0\cos(\omega_{osc}t)$ and the external electric field $\boldsymbol{E}(t) = \boldsymbol{E}(r)e^{-i\omega_P t}$.

$$\alpha(t) = \alpha_0 + \frac{\partial\alpha}{\partial Q}Q(t) \tag{1-134}$$

The dipole moment becomes.

$$\mu(t) = \alpha_0\boldsymbol{E}(r)e^{-i\omega_f t} + \frac{\partial\alpha}{\partial Q}Q_0\boldsymbol{E}(r)\left\{e^{i(\omega_P+\omega_{osc})t} + e^{-i(\omega_P-\omega_{osc})t}\right\} \tag{1-135}$$

The (1-135) equation describes the elastic Rayleigh scattering as the first term, the Stokes scattering as the term of $\omega_P - \omega_{osc}$, and the anti-Stokes scattering as the term of $\omega_P + \omega_{osc}$. The SR scattering intensity depends on the differential scattering cross-section [96] [97] given by

$$\delta_{R,diff} \equiv \frac{\partial \delta}{\partial \Omega} = \frac{\omega_P \omega_{osc}^3}{16\pi\hbar^2\varepsilon_0^2 c^4} |\alpha_R|^2 \quad (1\text{-}136)$$

where $d\Omega$ is the elementary solid angle, α_R is the Raman transition polarizability as a function of dipole moment when molecules transit between ground, final, and intermediate states. The SR scattering strength is proportional to the fourth-order frequency, which is linearly dependent on the incident frequency, the scattered frequency, and the remaining square of scattered frequency comes from the density of photon modes. The SR becomes very strong when the resonance Raman phenomenon happens – the incident frequency closely increases into the frequency of the electronic state $|\, v\rangle$.

The spontaneous Raman scattering can combine with confocal detection that allows studying the localization of nanomaterials in the cell molecules: proteins, DNA, and lipids. [98], [99] The SR scattering microscopy usually uses the collinear configuration shown in Figure 17.

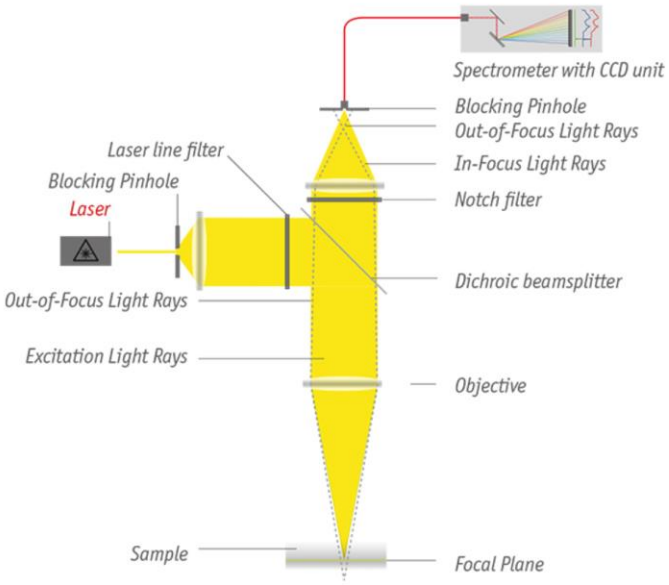

Figure 17. Confocal Raman microscopy setup

The sources of SR are usually SHG or THG of Nd: YAG (532 nm, 355 nm) and HeNe (632.8 nm) lasers. The backscattered configuration is used to move off elastically scattered light (Rayleigh scattering). The signal will be filtered and propagated into a spectrometer with a CCD camera.

SR imaging microscopy is a powerful tool used to study chemical bonds in materials. However, SR microscopy suffers a weak Raman cross-section and requires a long accumulation time and low chemical sensitivity because of the Raman scattering's intrinsically weak process.

Stimulated Raman scattering (SRS) microscopy.

Figure 16 (b) shows the nonlinear optical four-wave mixing process of the SRS phenomenon - material interacting with two incident light fields to induce a Raman-active transition. The temporal resolution of SRS microscopy ($\sim 1\ \mu s/\text{pixel}$) is much larger than SR scattering microscopy and has a spatial resolution of ~ 100 nm. SRS is driven by the third-order nonlinear susceptibility $\chi^{(3)}(\omega_R; \omega_P + \omega_s - \omega_P)$ in which the oscillation's modes are in phase to coherent modulate. The probe beam is an extra laser beam that

coincides with the Raman shift called the Stokes beam (ω_s) that is spatially and temporally synchronized with the pump beam shown in Figure 18. [100] The Stokes beam takes the role of light-induced molecular motions from the virtual states to the corresponding vibrational band of the ground state.

Each photon that undergoes SRS is shifted in color from pump to Stokes color. Thus, the SRS signal is proportional to the decrease or increase in the pump or Stokes beams intensities, respectively.

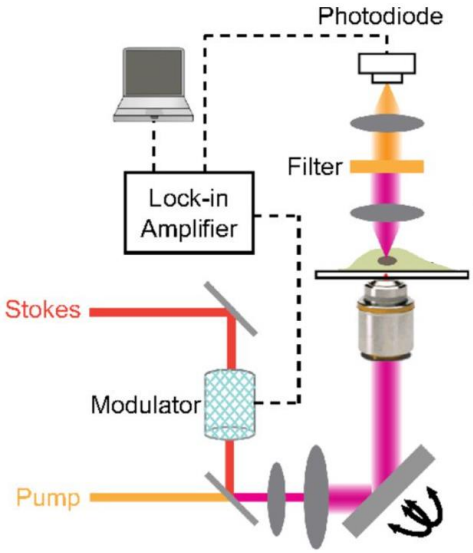

Figure 18. Stimulated Raman scattering (SRS) microscopy experimental scheme.

The SRS microscopy requires two laser sources, the initial incident beam as an excitation beam and the stimulating beam as the Stokes beam. The Stokes beam is generated from the initial beam using the optical parametric oscillator (OPO). There is a delay time device to modulate the temporal synchronization between the pump and the Stokes beam. Two incident laser beams are focused on the sample using the objective lens. The scattered signal intensity is inversely the fourth order of the incident beam intensity (pump loss and Stokes gain).

The SRS intensity is the result of the product of molecular density, Raman cross-section (interaction area), and the intensity of the pump and Stokes beams.

The common point between the SRS and SR is dependence on the Raman cross-section, the spectral linewidth, the path length of the light-field-material interaction, and the incident light intensity. Both SSR and SR suffer diffraction-limited leads to equivalent spatial resolution. However, the crucial difference between SRS and SR is the stimulation effect in the SRS. The chemical sensitivity of SRS microscopy is much higher than that of SR microscopy.

Therefore, SRS microscopy has several advantages: (i) significantly amplifies the Raman scattering signal, higher chemical sensitivity, faster imaging speed, and fine spatial resolution that have great help to study the ion diffusion process. (ii) SRS microscopy does not require fluorescent dyes as in the prevailing fluorescence imaging technique. (iii) SRS is also a non-invasive approach and does not require any specialized labels or probes that are like fluorescence microscopy.

Coherent Anti-Stokes Raman Scattering (CARS) microscopy.

CARS is a third-order nonlinear optical four-wave Raman mixing process that generates a newly shifted wave to the shorter wave region called the anti-Stokes wave. The energy difference between the pump and Stokes beam matches a molecular vibration of the sample. The pump and probe beam are mixed with the Stokes beam to produce the anti-Stokes (AS) scattering $\omega_{AS} = \omega_P - \omega_S + \omega_{pr}$. The third-order susceptibility $\chi^{(3)}(\omega_{AS}; \omega_P - \omega_S + \omega_{pr})$ with 48 elements [101] drive the CARS and is given in the following equation in resonant CARS. [102], [103]

$$\chi^{(3)} = \frac{\delta_R}{\omega_{osc} - (\omega_P - \omega_S) - i\Gamma_R} + \chi_{NR}^{(3)} \tag{1-137}$$

where Γ_R is the half maximum for the Raman line, δ_R is the Raman scattering cross-section. The first term of the (1-137) equation indicates that the vibration mode $\omega_{osc} = \omega_P - \omega_S$ will result in the CARS vibrational resonance. The nonresonant term $\chi_{NR}^{(3)}$ describes a nonresonant background susceptibility and causes distinctive distortion of CARS spectra. The distribution of real and imaginary parts to the CARS spectra is expressed in Figure 19 below.

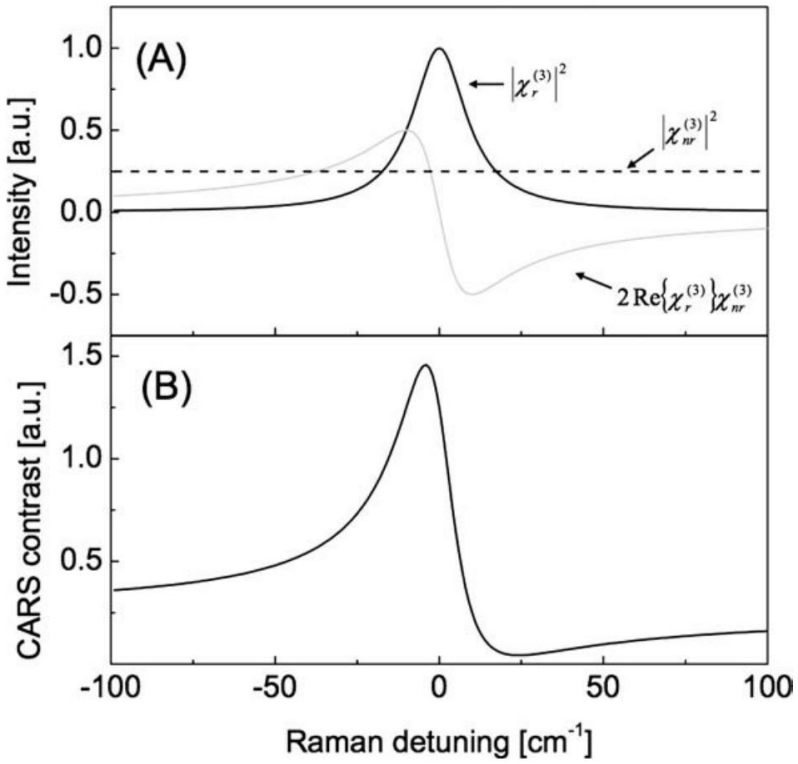

Figure 19. a) contribution of real and imaginary parts of $\chi^{(3)}$ to the CARS spectra (stimulation with a single Lorentzian line with $\Gamma_R = 10$ cm^{-1}, b) Total CARS signal of both real and imaginary parts.

The anti-Stokes intensity is proportional to the pump, Stokes, and probe beams intensity as below.

$$I_{AS} = \left|\chi^{(3)}\right|^2 I_P I_S I_{pr} \left(\frac{\sin\left(\Delta k.\frac{z}{2}\right)}{\frac{|\Delta k|}{2}}\right)^2 \quad (1\text{-}138)$$

where $\boldsymbol{z}$ is the vector normal of the sample's surface, representing the sample thickness. $\boldsymbol{k}_i$ is the wavevector of laser beams (i =P, S, pr, AS), $\Delta\boldsymbol{k} = \boldsymbol{k}_P - \boldsymbol{k}_S + \boldsymbol{k}_{pr} - \boldsymbol{k}_{AS}$ is the

wavevector mismatch. When the phase-matching condition is satisfied ($\Delta \boldsymbol{k} = 0$), the CARS signal will scatter unidirectional. In CARS microscopy, high numerical aperture (NA) lenses are used to save the phase-matching condition.

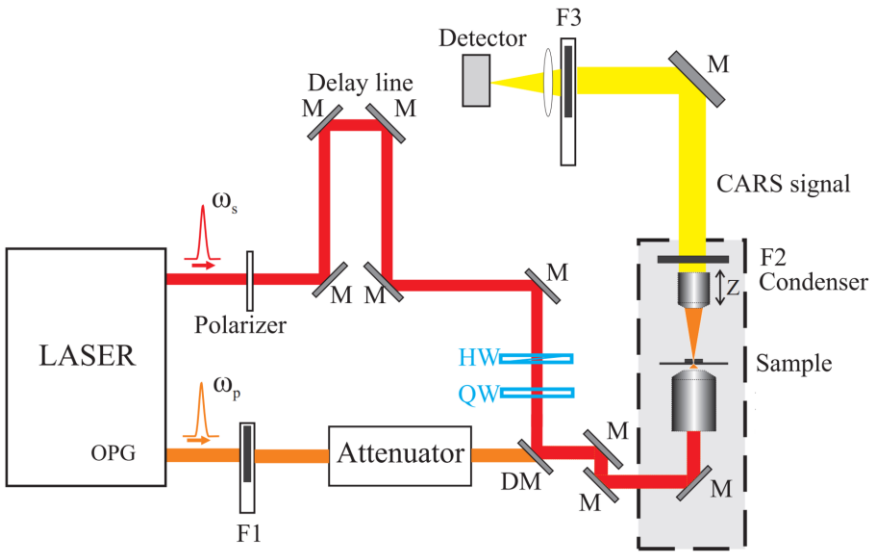

Figure 20. Coherent anti-Stokes Raman scattering (CARS) microscopy experimental setup.

The CARS technique uses the Stokes beam like the SRS microscopy, the pump, and Stokes beams are tightly focused into the sample in CARS microscopy shown in Figure 20, [104] and a CARS image characterizes the intrinsic vibrational contrast of the molecules.

The SRS and CARS techniques rely on the same Raman coherences in that it is driven by different frequency $\omega_P - \omega_S$. However, there are several differences between them as (i) SRS is background-free, non-background non-resonant, and SRS is usually proportional to the concentration of chemical bonds. (ii) SRS is detected in the phase-matched direction of the probe, but CARS is not. (iii) SRS signal is the self-heterodyning that is proportional to the nonlinear polarization P. On the other hand, CARS is not self-heterodyning that is proportional to the absolute square of the induced nonlinear polarization. (iv) SRS signal has the same spectral line shapes as probed in SR scattering, but CARS signal is a function of $\left|\chi^{(3)}\right|^2$, giving the difference to the measured spectral line shapes as in SR scattering.

Therefore, SRS microscopy is a better choice for frequency-domain experiments and is superior to CARS microscopy.

Summary of general advantages of Raman scattering microscopy

(i) The detailed Raman spectrum reflects the chemical structure of materials but is mostly unaffected by the local environment. Due to this, Raman spectroscopy is not only specific but also robust to environmental variability.

(ii) Raman spectroscopy is an intrinsically noninvasive technique, and the tunable excitation laser wavelength to avoid damage to samples like cells and tissues. The focusing spot size can be down to the sub-micron level, enabling micro-spectroscopy of tiny structures.

(iii) Unlike IR spectroscopy, Raman spectroscopy is capable of analyzing aqueous solutions because water does not present significant signals or absorption.

Disadvantages

(i) The low scattering cross-section of the SR effect still requires a relatively long integration time on the detector, typically from seconds to hours. The acquisition time for a Raman spectrum depends on several parameters, including the scattering direction of the sample, the volume of the measured sample, the spectral quality required, and the wavelength selected.

(ii) Techniques like line-scanning or wide-field imaging have been applied to improve the throughput, yet they suffer from other problems like field-curvature artifacts and spatial resolution, and the imaging speed is still not enough for most clinical applications.

(iii) nonresonant background can either distort or even saturate the resonant signal of Raman peaks, which reduces the image contrast.

1.3. Polysaccharide sacran material: properties and applications

Background of polysaccharide sacran

Polysaccharide sacran is an ampholytic mega-molecule extracted from the cyanobacteria Aphanothece sacrum (*A. sacrum*). [105] The very high-water absorption capacity of *A. sacrum*, [106] its amazing nonlinear response, [107]–[109] and its many applications in food, [110] cosmetics and medical products [111], [112] that make sacran have interested attention in studying and applications in many fields even in biomaterial and optical device. The raw sample, *A. sacrum*, comes from artificial cultivation on a river farm that undergoes many steps of manipulation with fresh water, ethanol, and hot alkaline to precipitate white fibrous material. The dilution in hot water and reprecipitation of the fiber sample will then be done several times to result in sacran solutions with a pH value of about 6.0 – 7.0. The molecular weight of sacran was analyzed using GPC (Jasco HPLC system with a Shodex OHpak SB-806MHQ column, 80 mmID x 300 mmL), is $M_W \approx 1.6 \times 10^7$ Da [113], [114] much higher than other supergiant polymers such as hyaluronic acid (4×10^6 Da), [115] xanthan gum ($M_W \approx \times 10^6$ Da), [116], [117] Cellulose ($M_W \approx 20 - 150$ kDa), [118]–[120] and Chitin (3,800 - 20,000 Da). [121] The polysaccharide sacran chain comprises various monosaccharides units as shown in Figure 21.

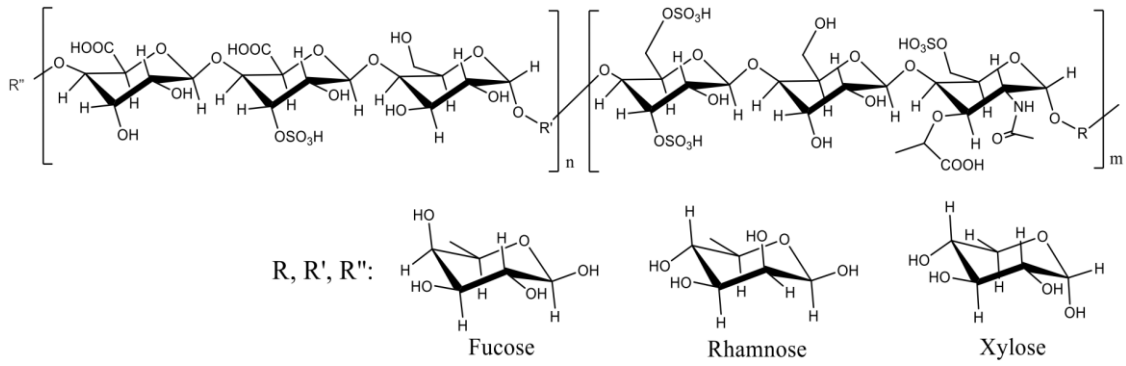

Figure 21. The partial structure of sacran

Chemical structure of sacran

Functional groups, such as carboxyl and sulfate, are the typical groups of sacran molecules and are used to distinguish polysaccharide sacran from other polysaccharides. Sacran has been of great attention in applications such as pharmaceuticals, drugs, cosmetics, and food because of numerous sugar residues in the molecular structure. [105], [113] The chemical elements of polysaccharides sacran were analyzed by using the spectroscopic study and indicated the percentage of C, H, N, and S elements equivalent to the ratio of 36.04%: 5.91%: 0.03%: 2.07%. The FTIR shows the peak of the carboxylate group at a wavenumber of 1613 cm^{-1}, while those of the sulfate group are at wavenumbers of 1223 cm^{-1} and 1363 cm^{-1}, and hydroxyls are at 1022 cm^{-1} and 3354 cm^{-1} as shown in Figure 22. [122], [123] Sacran contains anionic groups such as carboxylate and sulfonate in high concentrations (32% mol of the total sugar).

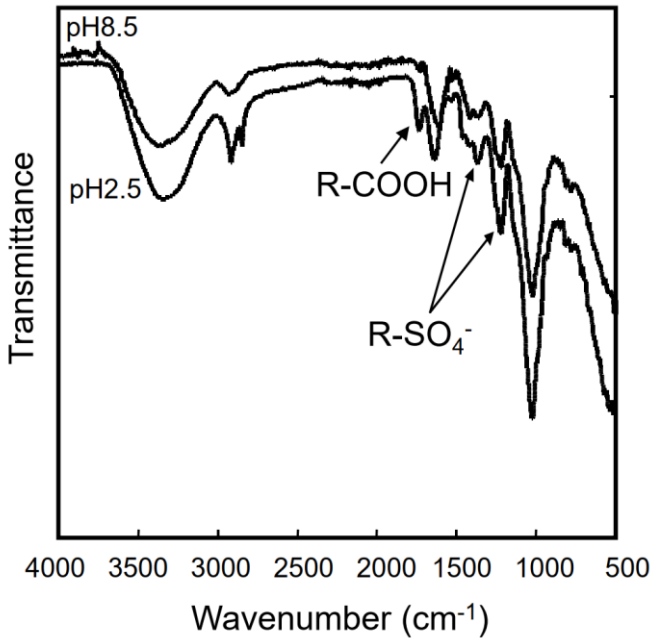

Figure 22. FT-IR spectra of sacran aqueous solution of pH 2.5 and pH 8.5

Polysaccharide sacran is confirmed that includes many monosaccharides such as Glc, Gal, Man, Xyl, Rha, Fuc, GalA, GlcA, Ara, GalN, and Mur. The presence of the N element

in the saran chain demonstrated that sacran is an ampholytic sugar chain with an anions/cation ratio of 30/1, the anions were suggested that originate from the sulfate (~27 %) and carboxylic (~22 %) groups while cations were from amino sugars (less than 1 %).

Properties of sacran

Viscosity: The viscosity (η) of sacran aqueous solutions varies in the concentration, molecular weight, and temperature of solutions. The viscosity property of a solution is usually studied by shear thinning at a concentration in advance. For example, the viscosity of 1 wt% sacran solutions with an initial viscosity of 83 000 cP is inversely proportional to the shear rate shown in Figure 23. [113], [124], [125]

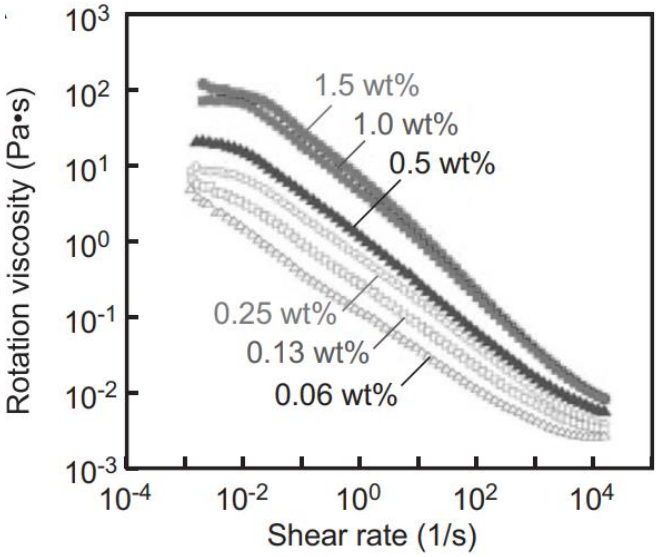

Figure 23. Shear rate dependence of apparent viscosity for 1 wt% sacran solution at 25 °C

Self-assembled property: This property is expressed by the intrinsic changing conformation of sacran chains depending on changing sacran solution concentration. At very low concentrations (c < 0.01 wt%), sacran chains form a rod-like structure with a length of 3 μm. That conformation will change to a double helixes structure at a concentration larger than 0.09 wt% and then achieve the liquid crystal phase at a concentration higher than 0.5 wt%. [124], [126] The sacran chains can twist each other to

make the twisted micro-fibers structure established by many other nano-fibers structures, flexible changing conformation from 2D to 3D structures and self-assembled dependence of sacran chains on adsorbing divalent metal ions, [125], [127] and creating microdomains in the surface of sacran cast film during the drying process (Figure 24). [125], [127]–[133] Sacran cations and anions are thought to be the main factor in the self-assembly of the sacran aqueous solutions.

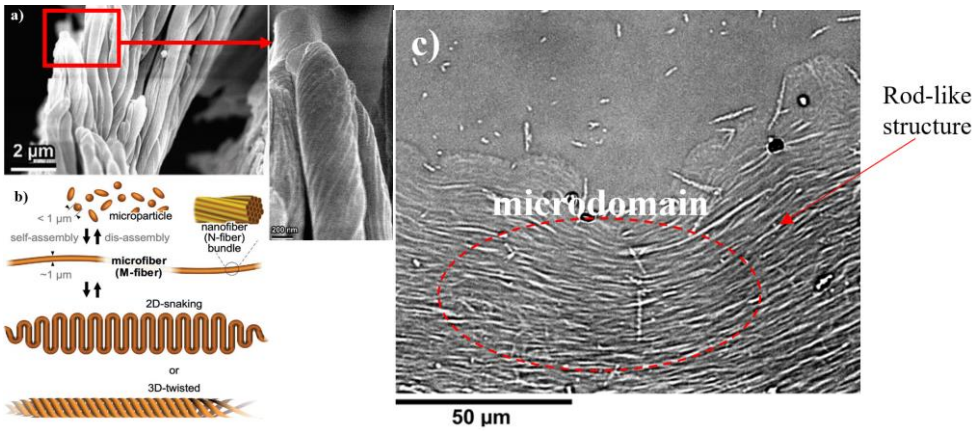

Figure 24. Sacran chains' conformation. a)micro- and nanofibers, b) snaking and twisted-like structure, c) microdomain in the surface of sacran cast film.

Oriented structure: The well-oriented structure of sacran molecules or sacran micro-rods is reported in various previous studies using SHG microscopy and polarized light microscope. [107], [108], [125], [133] These studies suggest that the sacran rod-like structures form parallel in a meniscus curve at the boundary of the cast film or in the vertical membrane at the contact line. [132]

Efficient absorption of pure water and adsorption metal ions: Sacran molecules have ultrahigh absorbent capacity for water (6100 ml/g) and 0.9 % saline (2700 ml/g). [113] The LC phase of sacran solutions can efficiently adsorb not only divalent but also trivalent metal ions, especially rare earth metal ions. [114], [134]–[140]

Nonlinear optical response: SHG phenomenon is one of the most amazing optical properties of sacran because of the chirality in their structure (Figure 21) [113] and was

first reported by Zhao et al. [107], [108] SHG from macroscopic media is enhanced when the polarization of the constituent molecules is oriented in the same direction within the wavelength scale. According to Zhao et al., the SHG signals from sacran molecules appear mostly as spots with sizes in the range from a few to tens of micrometers, and it had a core part with the strongest intensity at the near center. Except for these spots, most sacran molecules emit no SHG. The SHG intensity of the spots had an incident polarization dependence. Zhao et al. also detected SHG signals around a negative electrode of - 4.5 V when the sacran aqueous solution was put in an electrode cell, applied voltage, and dried. Hence this SHG from the saran films is not a trivial phenomenon, such as those from impurity or imperfection.

Application of sacran

Sacran is thought to be a biomaterial, and that is demonstrated once again by the moisture effect, anti-inflammatory effect, and anti-allergic effects of hydrogel sacran film applied for wound healing. [141] [142]–[147] The sacran's efficient adsorption of metal ions is attracting scientists' close attention because of its potential applications for issues related to polluted environments and application in material science. [148]–[150] The industrial application of sacran is the capability to fabricate transparent electrodes using the ability efficient adsorption of metal ions such as In^{3+}. [151]

Motivation to study

Previous studies such as surface morphology studying, changing conformation of sacran chains, the biological functions, and biomaterial function of polysaccharides sacran provided important information about the structure and behavior of sacran molecules in variant environmental conditions. However, there is still a lack of necessary information about the complicated asymmetric structures of sacran aggregates that can create the

strange phenomenon of the second-order optical response. There is an issue with the nonlinear optical response of sacran molecules that is the origin of the SHG activity of sacran aggregates is still mysterious and attracts my interest. This phenomenon is interesting not only as a property of sacran but also as a property of a general self-organizing polymer. Hence in this study, my main purpose is to clarify molecular orientation and the morphology of sacran aggregates at the micro-scale at the surface of cast film during the drying process of sacran solution by controlling sacran molecular weight, concentration, and temperature. In order to discover the origin of the SHG signal, SHG microscopy is an appropriate approach to studying the SHG response of sacran molecules. Besides that, sum-frequency generation (SFG), scanning electron microscopy (SEM), and diffractive X-ray scanning electron microscopy (EDX-SEM) are potential solutions for studying sacran cast films.

1.4. Conclusion

The benefits from the study of sacran molecules are extremely practical not only in the applications already in the food, medicine, pharmaceuticals, and cosmetics but also in the potential applications of materials in industry, environment, and optics. SHG microscopy is a powerful research method that, combined with other approaches such as SEM, EDX-SEM, and SFG spectroscopy, can form continuous studies that further uncover the structure of sacran molecules.

2. Chapter 2. Second-harmonic (SHG) microscopy for polysaccharide sacran

2.1. Experiment setup

SHG experiment

The SHG experiments are the main experiments of the whole project: the study of the self-assembled structure of polysaccharide sacran using second harmonic generation microscopy. In this section, I will introduce the experimental procedure and the main devices used in the SHG experiment. The excitation source is the commercial Ti: sapphire laser with a pulse width of 100 femtoseconds. The Ti: sapphire laser system includes three main parts as shown in Figure 25: (i) the seed beam system is a Ti: sapphire mode-locked laser, (ii) the pump beam system, and (iii) the Ti: sapphire regenerative amplifier laser system.

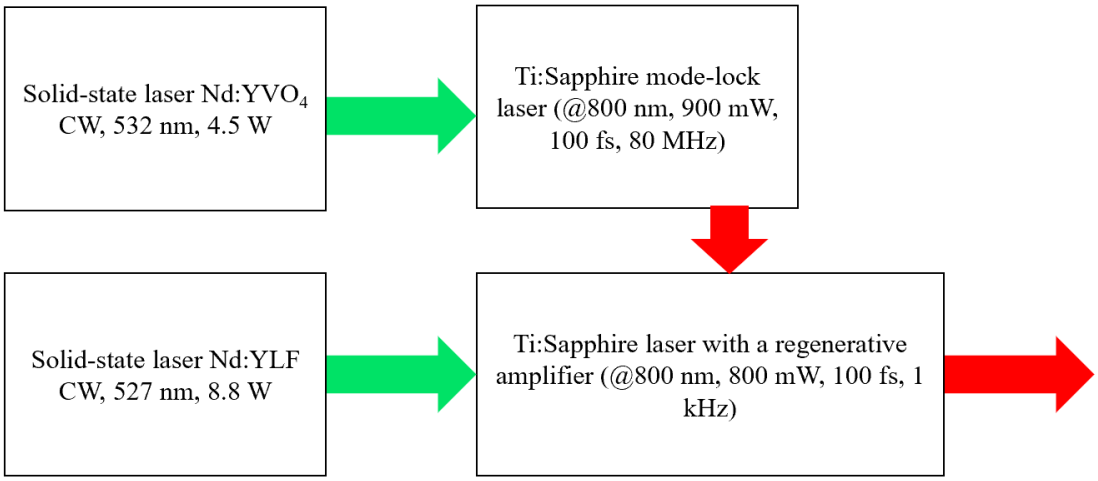

Figure 25. Block diagram of the Ti: sapphire laser system

Ti: sapphire laser is a solid-state laser in which the laser medium is a Titanium-doped sapphire crystalline material produced by introducing Ti_2O_3 into a melt of Al_2O_3. Ti^{3+}:sapphire laser was first developed in 1986 [152]–[154] and is a widely used transition-metal-doped gain medium for tunable lasers and femtosecond solid-state lasers. [155],

[156] The lasing action in Ti: sapphire laser corresponds to the transition level energy of Ti^{3+} as shown in Figure 26.

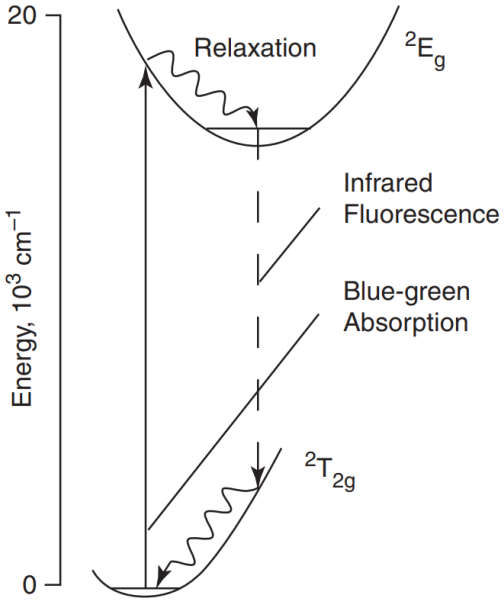

Figure 26. Energy Level diagram of Ti: Sapphire

Ti: sapphire laser quickly replaced most dye lasers and is very convenient for pumping test setups of new solid-state lasers because of its several advantages: (1) sapphire (monocrystalline Al_2O_3) has excellent thermal conductivity, alleviating thermal effects even for high laser powers and intensities. (2) The Ti^{3+} ion has a very large gain bandwidth allowing the generation of very short pulses and wide tunable wavelength. A lot of Ti: sapphire lasers operate with emission wavelengths between about 700 nm and 900 nm, where maximum gain and laser efficiency are obtained at around 800 nm. (3) Ti: sapphire lasers have an absorption range over a broad range of wavelengths from 400 to 600 nm. It is very appropriate to pump with a green laser as 514-nm argon ion lasers and frequency-doubled solid-state lasers based on neodymium-doped laser gain media. (4) The upper-state lifetime of Ti: sapphire is short (3.2 μs), and the saturation power is very high. A very high laser intensity can be used as an excitation source of Ti: sapphire.

(i) The Ti: sapphire mode-locked laser provides a central wavelength of 800 nm and is pumped using a solid-state laser Nd: YVO_4 with a central wavelength of 532 nm (green laser) as shown in Figure 27. [157] The output pulsed laser has a pulse width of about 100 fs and a repetition frequency of 80 MHz. In fact, the output wavelength depends on the specific purpose and has a range of NIR from 690 to 1040 nm.

Figure 27. Solid-state laser Nd: YLF system

A kind of passive mode-locking method called Kerr-lens mode-locking was used to obtain a train of mode-locked pulses of 100 femtoseconds (fs) duration from a solid-state laser as shown in Figure 28. The 532 nm laser pulses come into Ti: sapphire crystal and is reflected by a series of mirrors in the laser cavity. Photons emitted by the Ti: sapphire crystal are guided through the resonator cavity by reflection from the surface of routing mirrors. Other elements in the 10-mirror folded cavity include rod-focusing mirrors, an output coupler, a high reflector, beam-folding mirrors, dispersion control prisms, and a tuning slit for adjusting the output wavelength. The folded beam is finally passed through an acoustic-optic modulator (AOM), which ensures a constant frequency for mode-locked operation at laser start-up.

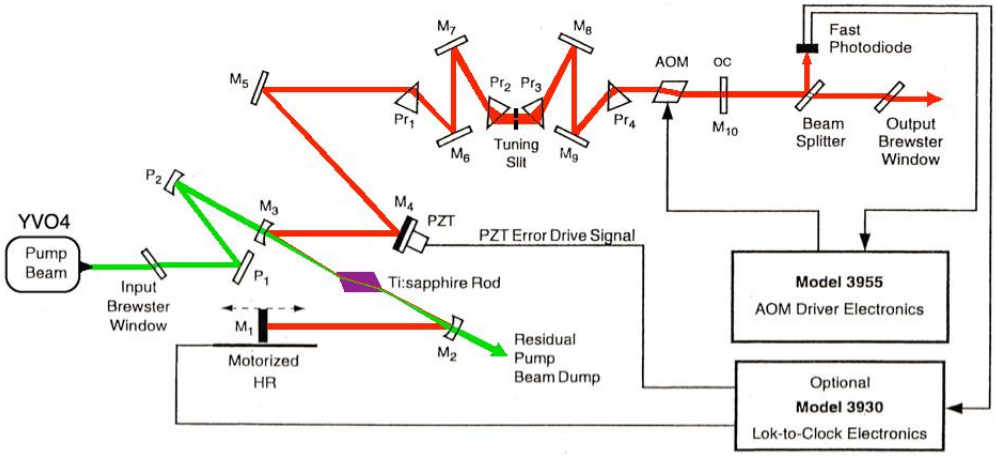

Figure 28. Schematic of the Ti: sapphire laser cavity used in the passive mode-locking technique

(ii) The pump beam system is a YLF (yttrium lithium fluoride-$YLiF_4$) laser based on neodymium-doped YLF (Nd3+:YLF) crystals. The gain and the emission wavelength of Nd: YLF is polarization-dependent: there is a stronger 1047 nm line for π polarization and a weaker one at 1053 nm for σ polarization. [158] A pulsed laser with a pulse width of 12.5 ns and a repetition frequency of 1 kHz is generated by the Q switch technique, the oscillation wavelength is 1053 nm, and the output is at a wavelength of 527 nm using the internal cavity SHG method.

(iii) The Ti: sapphire regenerative amplifier laser system is seeded by a low-energy laser pulse. [159] The seed beam with low energy is designed to recirculate and be amplified to become high peak-power pulses. An individual pulse from the train of mode-locked seed pulses is selected by the spitfire cavity and reduced the repetition frequency from the megahertz mode-locked train to kilohertz rates of the amplified pulses. After 20 or more times passing through the Ti: sapphire crystal of the selected pulse, an input pulse of a few nanojoules of energy may be amplified to roughly a millijoule using the stretch-compressor technique. In Figure 29, the Ti: sapphire crystal is pumped by the green laser (527 nm) inside the regenerative amplifier device.

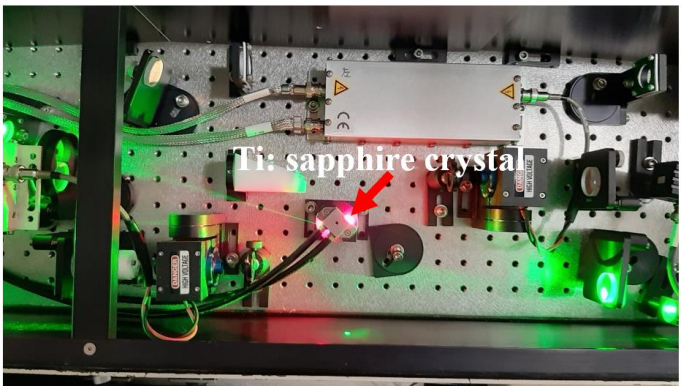

Figure 29. The green laser irradiates the Ti: sapphire crystal

The output laser pulses from the regenerative amplifier device are usually adjusted to make sure that the pulse width is always around 100 fs. The temperature and other similar parameters of the environment may affect the stability of the compressor to optimize the pulsed output. Changing the compressor length (within about 0.1 mm) using the motion controller can optimize the compressor. The full width at half maximum is monitored by an autocorrelation, Figure 30 while using the motion controller to adjust the horizontal retroreflector.

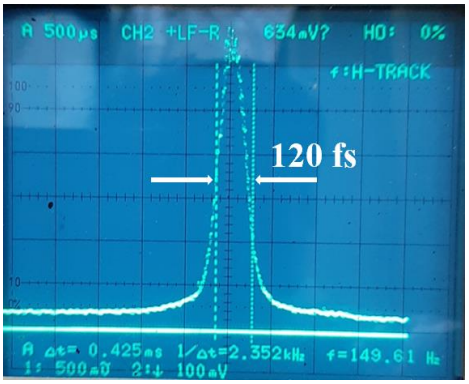

Figure 30. The full width at half maximum (FWHM) of Ti: Sapphire laser with a regenerative amplifier.

The observation part uses a microscope combined with the image intensifier-charge coupled device (II-CCD) camera (Hamamatsu Photonics PMA-100) through an objective lens (Olympus UMPlan Fl) and a CMOS (Complementary Metal-Oxide-Semiconductor) camera (Lul35M manufactured by Lumenera). The parameters of microscopy are shown in table 7. [160]

Table 7. Specification of Olympus UMPlanFI objective lens

Objective lens	magnification	Numerical aperture (NA)	Working distance (mm)	Resolution (μm)	Depth of focus (μm)
Olympus UMPlan Fl	5x	0.15	20.0	2.24	43.3
	10x	0.30	10.1	1.12	10.8
	20x	0.46	3.1	0.73	3.84
	50x	0.8	0.66	0.42	1.27

The experimental setup to determine the accurate position of the SHG-active aggregates in the cast films is shown in Figure 31.

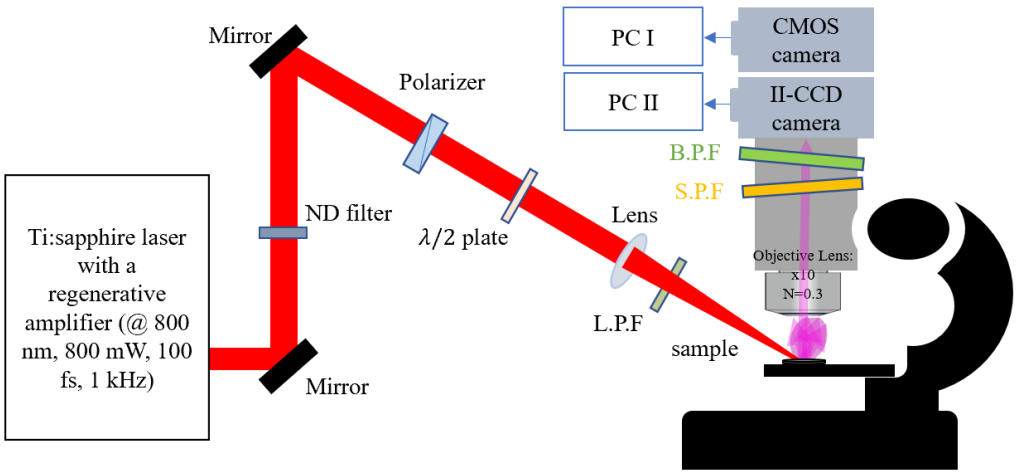

Figure 31. The experimental setup for SHG observation

The incident laser is the regenerative amplifier Ti: sapphire laser with a repetition frequency of 1 kHz, a pulse width of about 100 fs, and a central wavelength of 800 nm. The incident power of this pulsed laser is adjusted using an ND (Neutral Density) filter. In order to avoid damage to the samples, samples are placed at the stage microscope and have a distance of several millimeters from the focusing plane of the incident laser beam. I focused the beam onto the sample with a lens with a focal length of 200 mm. A long-pass filter (L.P.F) is located between the lens and the stage of the microscope to lock

wavelengths below 780 nm. SHG images were observed by using a bandpass filter (B.P.F) of 400 nm wavelength and an II-CDD camera with an accumulation time of 300 seconds. Two-photon excited fluorescence images were observed by using a bandpass filter of 438 nm wavelength and an II-CDD camera with an accumulation time of 60 seconds. A short pass filter (S.P.F) was used to pass through a short wavelength from 350 to 785 nm and reject 800 nm wavelength. Linear images of the sample were observed in the same setup as the SHG observation above using white light illuminations and a CMOS camera.

Figure 31 also indicates that the combination of the polarizer and half-wave plate ($\lambda/2$) is used to investigate the polarization-dependence of SHG intensity of SHG-active sacran aggregates. The polarizer controls the polarization of the incident laser pulse. The original polarization of the incident laser pulse is marked by the blue arrow shown in Figure 32a. The p-polarization illustrated in Figure 32b corresponds to the angle of the polarizer plate at 238.7º.

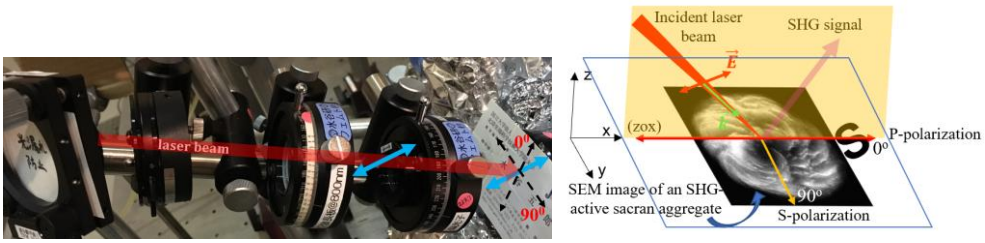

a) b)

Figure 32. The polarization-dependence experimental setup. a) illustration of incident polarization of laser beam, b) illustration p-polarization irradiates to the sample.

The saturation may occur at the high incident laser power and sacran aggregate's high concentration and strong local electric dipole. Saturation occurs at a charge collection site causing the accumulation of additional photo-generated charge and overflow of the excess electrons into adjacent device structures. For example, Figure 33 below shows the saturation phenomenon from a sacran aggregate at the incident laser power of 7 mW.

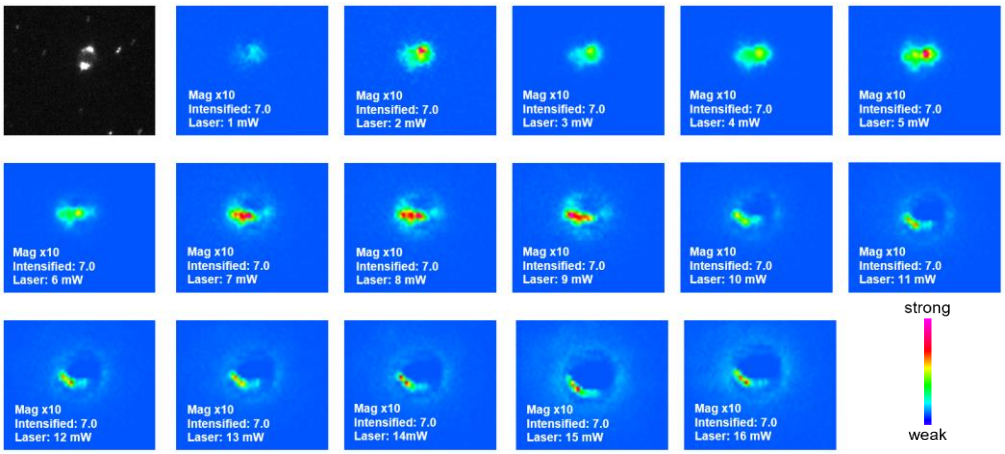

Figure 33. The saturation phenomenon at low incident laser power

The saturation causes the change in peak position and the number of peaks. At the initial peak position, SHG intensity becomes zero (at 7 mW picture) and establishes a circle shape non-signal area. This non-signal area increasingly extends and brings the changing of the peak position.

The changing of peak position and even the drop of SHG intensity at saturation point is not only causing damage to the camera but also causing challenges to the investigation of power dependence of SHG intensity. Hence all experiments in this study were performed so that the observed signals were well below the saturation threshold.

2.2. Materials and samples

For all the experiments in this study, I used sacran biomaterials at a concentration of 0.5 wt%. For several reasons (i) the nematic liquid crystalline (LC) phase may form with high potential [124] and (ii) microfiber sacran self-assembled together and well oriented on a drying interface. [131]

The ultrasonication treatment

The original sacran aqueous solutions (60 ml, 0.5 wt%), were prepared at Kaneko Laboratory and were applied sonication with an ultrasonic tip 13 mm diameter made of a titanium alloy (Ti-6Al-4V) controlled by a SONICS Vibra cell VCX750 ultrasonicator

(Sonics & Materials Inc. USA, Frequency: 20 kHz). The ultrasonication time was 10, 20, 30, 40, 60, 300, 600, and 1800 seconds. Magnetic stirring was carried out during the ultrasonication process. This ensures that the entire sacran aqueous solution is exposed to the ultrasound probe, increasing the homogeneity needed for the entire sample. Ultrasonicated solutions had a 10-second cooldown time every 50 sec to avoid overheating. The ultrasonicated samples were centrifuged using centrifuge vaporizer equipment (EYELA CVE-200D) for 30 – 45 minutes to separate the metal fragments having a mass greater than the molecular weight of sacran molecules. To remove micro-scale dust particles possibly emitted from the irradiance probe of the sonic device, the syringe filter with a 5 μm of pore size was used.

Sacran molecular weight was calculated by using a multi-angle static laser light scattering device (MALLS; Dawn Heleos, II, Wyatt Technology). MALLS system (Laser wavelength: 665.2 nm) was equipped with a size exclusion chromatography (SEC) system with the SEC columns (Shodex OHpak with a dimension of 8.0 mmID x 300 mmL, SB-807G (Guard), SB-807 HQ, and SB-804 HQ) under a column temperature of 40^{o} C. The connection of injected sacran solution in $NaNO_3$ aqueous solution (0.1 M) was 0.01% (injected volume is 100 μm), and then the sample was released at a rate of 1 ml/min.

The molecular weight of sacran chains and viscosity of ultrasonicated sacran solutions

After ultrasonic treatment, the molecular weight was a logarithmic function of sonication energy. The average molecular weight of the sacran molecule decreased to less than one-third of its original after 30 seconds of ultrasonication time as shown in Figure 34.

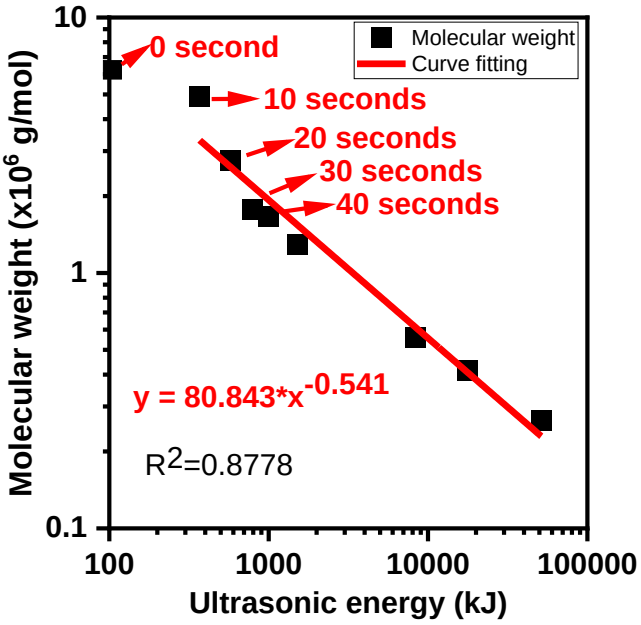

Figure 34. The molecular weight of sacran molecules depends on the ultrasonication energy as a logarithmic function.

The viscosity of the sacran aqueous solution looked remarkably decreased and is estimated using the following equation. [161]

$$\eta = \eta_0[1 + 0.67\alpha\phi + 1.62(\alpha\phi)^2] \quad (2\text{-}1)$$

where η and η_0 are the viscosities of the suspension and dispersion medium (water, $\eta_0 =$ 0.89 cps), respectively, ϕ, α, are the volume fraction of the disperse phase (sacran), and the ratio of chain length to width of the dispersing sacran chains, respectively, with a concentration of 0.5 wt %, $\phi = 5\,x\,10^{-3}$ based on assumptions for the suspension density, α= 4300. The size of the sacran chain was estimated to be 8.6 x 10^4 nm in length {the number of sugar residues (size 0.5 nm) = 1.7 x 10^5} and 20 nm in width by electron microscopy. [124] Table 8 shows the estimated molecular weight of the sacran molecule. Table 9 shows the estimated viscosity of the ultrasonicated sacran solution at different ultrasonication times.

Table 8. The estimated molecular weight of the ultrasonicated sacran molecule

time (s)	energy (kJ)	Mn (10^6 g/mol)	Mw (10^6 g/mol)	Mw/Mn	Estimated length (nm)
0	0	5.45 (±11.20%)	6.640 (±12.17%)	1.22 (±16.54%)	8.6 x10^4
10	369	4.89 (±7.82%)	5.123 (±8.98%)	1.04 (±11.90%)	66.35 x10^3
20	579	2.77 (±3.55%)	2.931 (±3.39%)	1.06 (±4.91%)	37.97 x10^3
30	788	1.78 (±15.73%)	1.920 (±22.02%)	1.08 (±27.06%)	24.85 x10^3
40	995	1.67 (±6.23%)	1.990 (±10.74%)	1.19 (±12.41%)	25.76 x10^3
60	1524	1.29 (±4.8%)	1.650 (±7.55%)	1.28 (±8.95%)	21.07 x10^3
300	8369	0.56 (±0.67%)	0.629 (±0.84%)	1.12 (±1.08%)	8.127 x10^3
600	17788	0.41 (±0.96%)	0.461 (±0.87%)	1.11 (±1.30%)	8.041 x10^3
1800	51363	0.26 (±0.84%)	0.303 (±0.91%)	1.14 (±1.24%)	3.923 x10^3

Table 9. The estimated viscosity of the ultrasonicated sacran solution

Estimated length (nm)	The ratio α	Viscosity (cps)
8.6 x10^4	4300	680.18
66.35 x10^3	3317.5	407.48
37.97 x10^3	1898.5	136.47
24.854 x10^3	1242.7	60.26
25.757 x10^3	1287.85	64.51
21.07 x10^3	1053.5	44.04
8.127 x10^3	406.35	8.05
8.041 x10^3	402.05	7.92
3.923 x10^3	196.15	2.86

The dependence of molecular length and viscosity of ultrasonicated sacran solutions on the ultrasonication time is a logarithmic function and is shown in Figure 35.

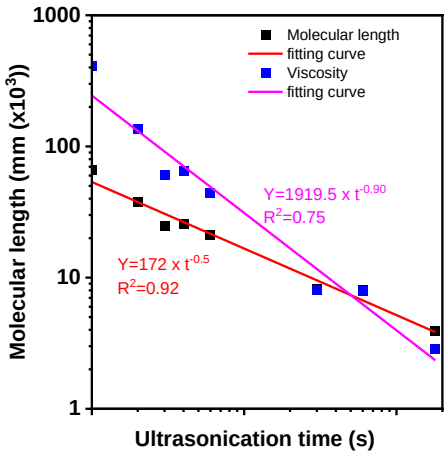

Figure 35. The estimated molecular length (black dots) and viscosity (blue dots) of ultrasonicated sacran solutions and their fitting lines (red and purple colors), respectively.

Sacran adsorbing Er^{3+} and Nd^{3+} metal ions

Hydrated crystals $NdCl_3.6H_2O$ and $ErCl_3.6H_2O$ were soluted using pure water for a concentration of 0.06 M. I dropped the hydrated crystals into a volume of 50 mL of pure water and shook them by hand to completely solute of salt crystals. Metal ion aqueous solutions are then separated into five equivalent parts for each type of metal ion and stored in each different small glass bottle. The original 0.5 wt% sacran solutions, 10 seconds, 20 seconds, and 30 seconds of ultrasonicated sacran solutions are dropped into the metal ion solutions and shaken by hand to form stable gel beads of sacran droplets. Gel beads are kept inside the metal ions' aqueous solutions for about 24 hours and taken out to make cast films (Figure 36).

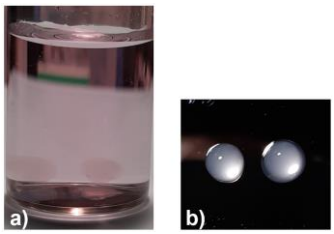

Figure 36. (a) droplets of original 0.5 wt% sacran solutions in the metal ions aqueous solutions, (b) on the surface of a silicon substrate.

Finally, ultrasonicated sacran aqueous solutions and sacran absorbing Er^{3+} and Nd^{3+} metal ions are dropped onto the surface of silicon substrates to create dried cast films at room temperature. Silicon wafers with native surface oxide layers are used as substrates because of the centrosymmetric crystalline structure of silicon. The second-order nonlinear optical phenomena are forbidden. [162] [163] The surface SHG signals from the silicon substrate are almost zero.

2.3. Results and discussions

2.3.1. Power dependence of second-harmonic generation signal generated from sacran aggregates

The observed SHG spots of the sacran cast films are proposed to originate from the nucleus-like structure created from positive charges sacran at the center and negative charges sacran at the surrounding area of the spot. [107]–[109] This hypothesis has partly shown the origin of the SHG response of sacran molecules. Motivated by previous studies, I investigated the SHG response of ultrasonicated sacran solutions.

SHG spot of ultrasonicated sacran solutions

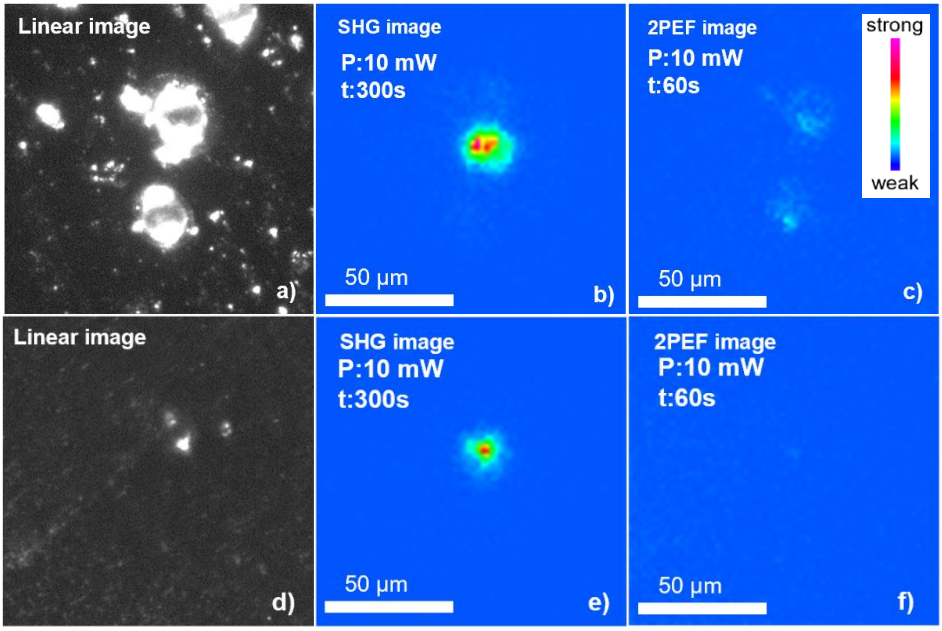

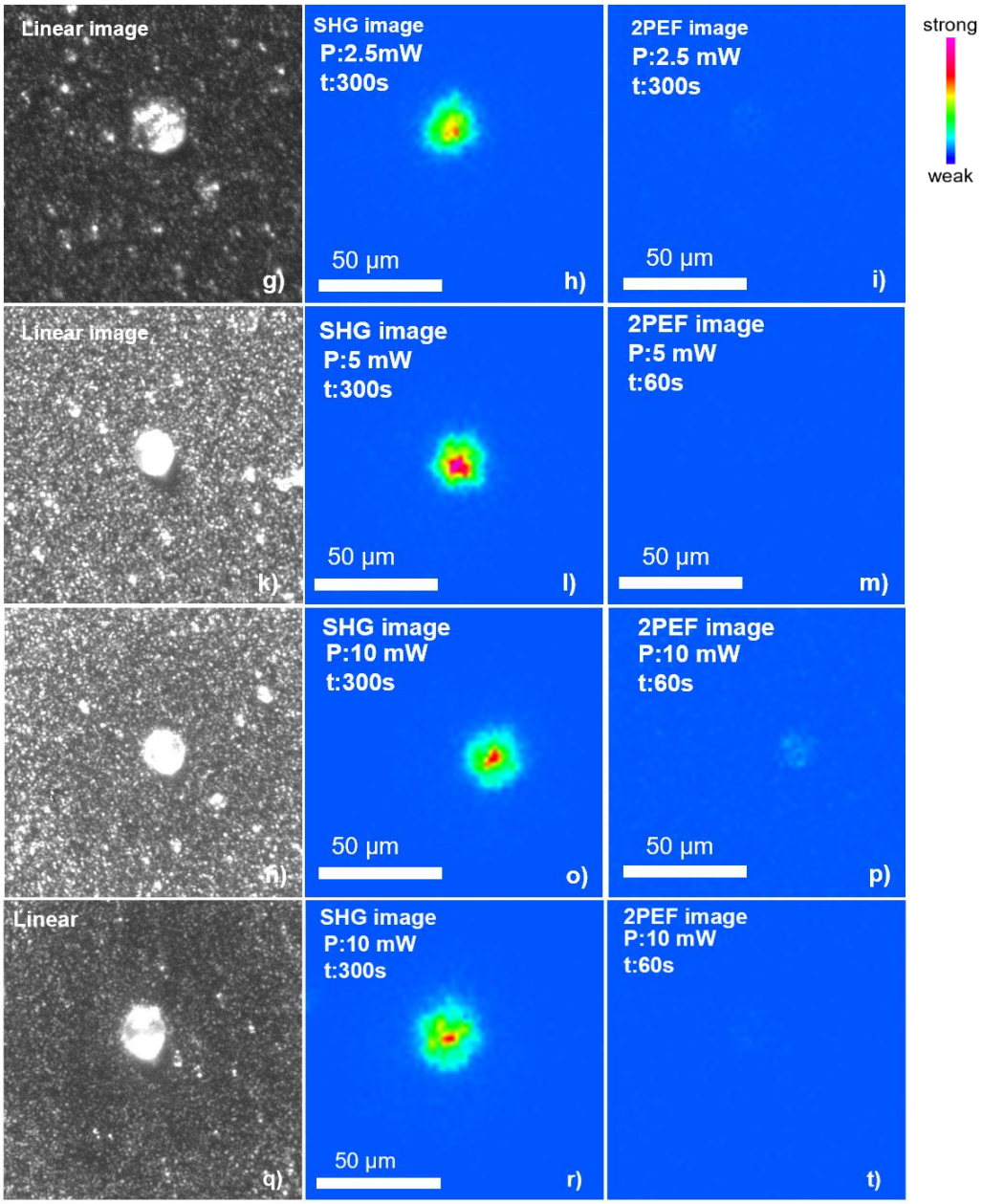

Figure 37. The linear, SHG, and 2PEF images of original sacran solutions (a-c) and ultrasonicated sacran aqueous solutions after zero (d-f), 10 seconds (g-i), 20 seconds (k-m), 30 seconds (n-p), and 40 seconds (q-t) ultrasonication time, respectively.

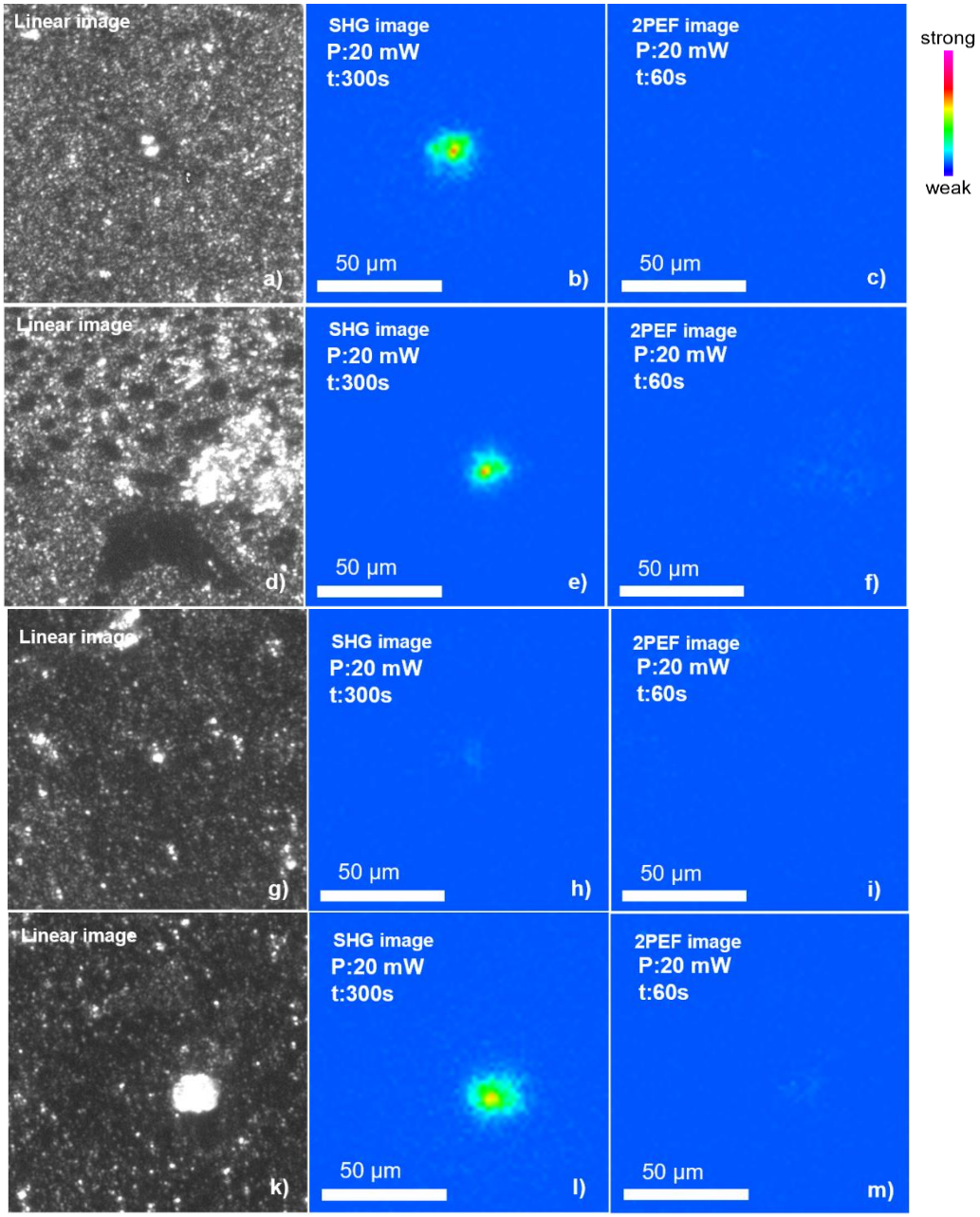

Figure 38. The linear, SHG, and 2PEF images ultrasonicated sacran aqueous solutions after 60 seconds (a-c), 300 seconds (d-f), 600 seconds (g-i), and 1800 seconds (k-m) ultrasonication time, respectively.

Figures 37 and 38 show the SHG spots detected from correlated linear areas in the corresponding linear images. Linear spots are sacran aggregates like the cluster structures that emerge from the surface of cast films. These cluster-like structures especially become different from surrounding areas in the ultrasonicated sacran solutions. For SHG-active sacran aggregates with only one peak of SHG intensity near the center of the SHG spots,

near the center of SHG-active sacran aggregate should have a strong electric dipole. Thus, it can't separate into new spots even at high resolutions of microscopy. For the complex SHG spots with two or more peaks near the center of the SHG spot, the SHG-active sacran aggregate may consist of several neighborly electric dipoles. When using a high-resolution microscope, these peaks may separate into vicinity isolated peaks, but they are not new spots.

When the asymmetric structures have a size smaller than the scale of the wavelength, nonlinear polarization of two vicinity asymmetric structures can be in opposite directions. The SHG signal generated from two vicinity asymmetric structures can have canceled each other. Therefore, SHG of asymmetric structures with the average size in wavelength scale is forbidden. Therefore, the size of asymmetric structures should be much larger than the wavelength scale.

The resolution of 1.12 μm is used to observe the SHG signal corresponding to the magnification of x10. This resolution value is still smaller than the molecular scale (Tables 8 and 9 in the main theses). SHG microscopy with an objective lens of x10 is good enough to distinguish the SHG signal from two sacran molecules if the distance between these two sacran molecules is larger than several micrometers. However, in fact, there are many sacran molecules arranged parallel with each other in the width of several nanometers, and the microscope with a magnification of x10 can't distinguish this distance. Thus, microscopes with higher spatial resolution should be used such as TEM to distinguish the molecules. At low spatial resolution, the total SHG intensity of a pair of opposites dipoles will be canceled.

In general, the spatial resolution of a microscope depends on the objective lens, and laser beam. I assume that a laser beam after a focusing lens has a Gaussian distribution. The electric field profile for a linear polarization is expressed as [164], [165]

$$\mathbf{E}_{\omega}(x,y,z) \propto E_0 exp\left(-\frac{-2(x^2+y^2)}{w^2} - \frac{z^2}{w_z^2} - i(\boldsymbol{\xi} k_{\omega} z + \varphi)\right)\hat{\boldsymbol{y}} \tag{2-2}$$

where ω is the angular frequency of the fundamental, $\hat{\boldsymbol{y}}$ is the polarization direction, $k_{\omega} \propto 2\pi/\lambda_{\omega}$is the wave vector, $\boldsymbol{\xi}$ is the wave vector reduction factor, x,y, and z are coordinates in the object plane, φ is the phase of the external electric field. The w is the 1/e radii of the focal ellipse in the lateral direction and is calculated by:

$$w = \frac{0.32\lambda_{\omega}}{NA} \propto R \tag{2-3}$$

where R is the spatial resolution of the microscope.

The intensity of the SHG signal in the image plane of the detector can be calculated by: [166]

$$I_{SHG,image}(X,Y,Z) = I_{SHG,O}(X,Y,Z) \otimes F_{PSF}(X,Y,Z) \tag{2-4}$$

where$I_{SHG,O}\,(X,Y,Z)$ is the SHG intensity of an individual noncentrosymmetric molecule in the objective plane detected in the image plane, $F_{PSF}(X,Y,Z)$ is the point spread function.

The theoretical distribution of $I_{SHG,O}\,(X,Y,Z)$is an exponential function of the spatial resolution (R) of the microscope. [165]

$$I_{SHG,O}\,(X,Y,Z) \propto |\mathbf{E}_{2\omega}|^2 \propto |\mathbf{E}_{\omega}|^4 \beta^2 \times \iiint C^2(x,y,z) \times exp\left(\frac{-4(x^2+y^2)}{R^2} - \frac{4z^2}{w_z^2}\right) \times \exp\left(-2ik_{2\omega}(X+Y+Z)\right)\cos(2\varphi)dxdydz \tag{2-5}$$

where $C(x,y,z)$ is the spatially heterogeneous concentration of scatterer, R is the resolution of the microscope, $w_z = \frac{0.53\lambda_{\omega}}{n_{\omega}(1-\cos\Theta)}$, Θ is equal to one-half of the objective's opening angle, β is the hyperpolarizability of the medium.

The point spread function for the microscopy is given by:

$$F_{PSF}(X,Y,Z) = \int_0^1 J_0\left[\frac{0.61\,\lambda_{2\omega}k_{2\omega}}{R}\rho \times ((X-x)^2+(Y-y)^2) \times \sin\left(k_{2\omega}(Z - z)\left\{\left[1-\left(\frac{0.61\,\lambda_{2\omega}}{nR}\rho\right)^{\frac{1}{2}}\right]^2\right\}\right)\right]d\rho \quad (2\text{-}6)$$

where J_0 is the zeroth-order Bessel function, ρ is the normalized radius in the back focal plane of the objective lens, n is the index of refraction of the medium, and $k_{2\omega} \propto 2\pi/\lambda_{2\omega}$.

$$I_{SHG,image}(X,Y,Z) \propto \sin(\varphi)\,|\mathbf{E}_\omega|^4\beta^2 \times \iiint C^2(x,y,z) \times exp\left(\frac{-4(x^2+y^2)}{R^2} - \frac{4z^2}{w_z^2}\right) \times \exp\left(-2ik_{2\omega}(X+Y+Z)\right)\cos(2\varphi)\,dxdydz \otimes \int_0^1 J_0\left[\frac{0.61\,\lambda_{2\omega}k_{2\omega}}{R}\rho \times ((X-x)^2 + (Y-y)^2) \times \sin\left(k_{2\omega} \times (Z-z) \times \left\{\left[1-\left(\frac{0.61\,\lambda_{2\omega}}{nR}\rho\right)^{\frac{1}{2}}\right]^2\right\}\right)\right]d\rho \quad (2\text{-}7)$$

Considering two non-centrosymmetric molecules located at a distance much smaller than an optical wavelength. If the spatial resolution is very low, the total SHG signal integrates over the region including two non-centrosymmetric molecules. When two non-centrosymmetric molecules are oriented in parallel directions (two molecular diploes are in the same direction). SHG signals generated from these two non-centrosymmetric molecules are in phase (φ). Therefore, the total SHG signal is enhanced $I_{2\omega,tol} = I_{SHG,O1}(X,Y,Z) + I_{SHG,O2}(X',Y',Z')$. In other words, if two non-centrosymmetric molecules are oriented in anti-parallel directions (two molecular diploes are in opposite directions). SHG signals generated from these two non-centrosymmetric molecules are out of phase ($\varphi + \pi$). The total SHG signal integrated from the SHG signal generated from two anti-parallel non-centrosymmetric molecules will be canceled $I'_{2\omega,tol} =$

$I'_{SHG,O1}(X,Y,Z) - I'_{SHG,O2}(X',Y',Z')$ In order to avoid the cancellation of the SHG signal, the spatial resolution of the microscope is high enough to observe the SHG signal from an individual non-centrosymmetric molecule. For example, if the distance of two non-centrosymmetric molecules is in a distance much smaller than an optical wavelength (~ 100 nm). The spatial resolution of the microscope should be smaller than 0.1 µm.

The most common property of SHG spots is having a very sharp shape (Figure 39), which means very high SHG intensity at the center of the SHG spot. The 2PEF images show nothing at the same correlation position as SHG pots.

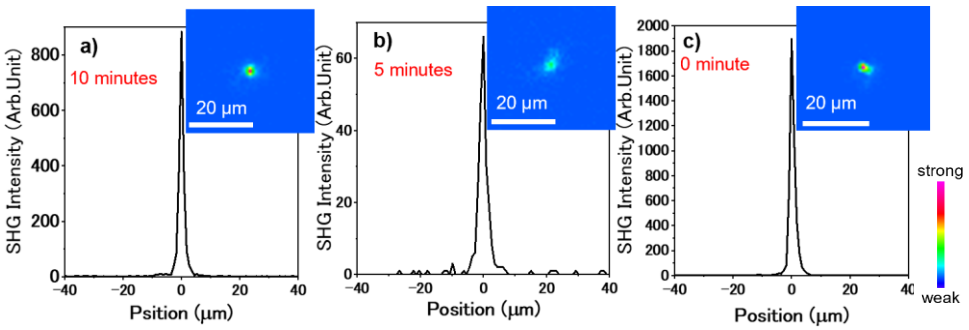

Figure 39. The intensity profiles of the SHG micro-spots of sacran solution which ultrasonicated for 10 minutes (a), 5 minutes (b), and zero minutes (c).

Multi-photon fluorescence was investigated by using a bandpass filter of 370 nm and 390 wavelengths and no signal was seen at all (Figure 40). Hence there is no three or four-photon-excited fluorescence under the current excitation power. These indicate that the signal in SHG images detected in Figures 28 and 29 are SHG signals.

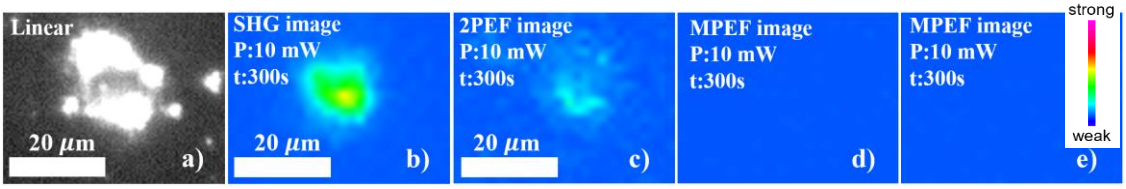

Figure 40. The linear, SHG, 2PEF, and multi-photon excited fluorescence images of another SHG-active aggregate of the original sacran solution. The observation wavelengths are 370 and 390 nm for multi-photon excited fluorescence.

Figure 40 (c) indicates that the 2PEF signal has broadband instead of a sharp peak. This demonstrates that the signal in Figure 40 (a) is the SHG signal. (d) and (e) show multi-photon excitation fluorescence observed using band-pass filters of center wavelengths 370 nm and 390 nm. These results show that there is a negligible contribution of three- and four-photon fluorescence.

The power dependence of SHG intensity

The power dependence of SHG intensity of ultrasonicated sacran aggregates is investigated controlling incident power of the ND filter. Here, I selected the sacran cast film made from 20 seconds of ultrasonicated sacran solutions shown in Figure 41. Because these SHG-active sacran aggregates become visible and easy to determine by a CMOS camera.

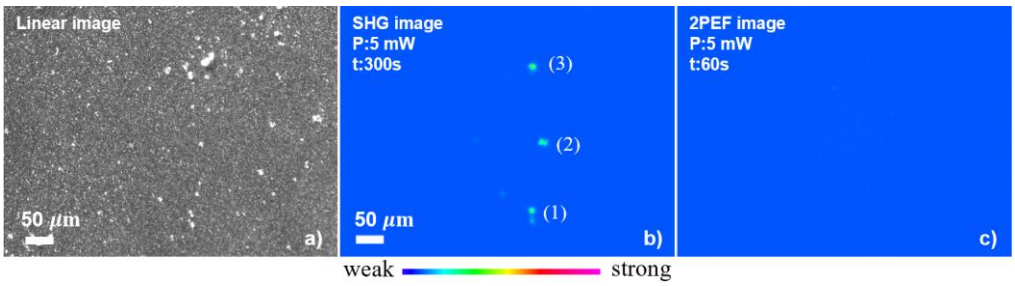

Figure 41. SHG signal from corresponding clear linear spots

The range of incident laser power from 1 to 28 mW because of the higher incident power may cause damage to the sacran cast film and the saturation of SHG intensity. The power dependence of the 2PEF signal was not investigated because nothing was observed in the correlated 2PEF images. Three SHG spots in Figure 41 b were figured out simultaneously and pointed out the homogeneous increase of SHG intensity. The results are shown in Figure 42 a, while the 3-D shape of SHG spots is illustrated in Figure 42 b.

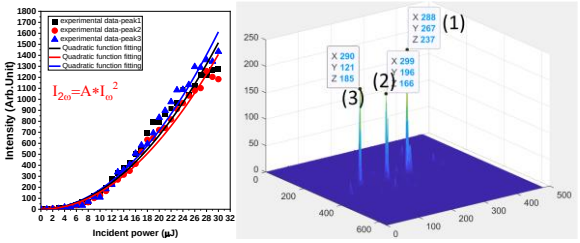

a) b)

Figure 42. a) Quadratic proportional power dependence of SHG intensity of SHG-active sacran aggregates, b) the 3-D shape of SHG spots.

The SHG intensity ($I_{2\omega}$) of sacran aggregates shows the tendency of a quadratic function of incident laser intensity (I_{ω}) (see table 10). Experimental data were fitted using a quadratic function and the coefficient of determination (R.squared) for each SHG spot is shown in Figure 42 b.

Table 10. Quadratic function fitting of SHG intensity

SHG spot	Quadratic function	R-square	Standard Error (%)
Spot 1	$I_{2\omega} = 1.792 * I_{\omega}^{2}$	0.98043	3
Spot 2	$I_{2\omega} = 1.68 * I_{\omega}^{2}$	0.96594	3.7
Spot 3	$I_{2\omega} = 1.57 * I_{\omega}^{2}$	0.97785	2.8

When the SHG intensity is high, several possibilities such as (i) the SHG-active sacran aggregate has a very high concentration of both sacran cations and anions in which sacran cations take a role as a nucleus and are surrounded by sacran anions. This structure creates a strong local electric field that mainly contributes to the SHG intensity. (ii) sacran molecules are well oriented with each other and parallel with the external electric field vector.

2.3.2. Polarization dependence of second-harmonic generation active sacran aggregates

Sacran aggregates have a nucleus-like structure with the positive sacran at the center. However, the structure of the surrounding negative sacran is still a mystery. The

polarization dependence of SHG intensity is one of the powerful tools to survey the oriented structure of sacran aggregates.

The polarization angle of incident light was defined as $\theta = 0^o$ when it was P-polarized after a polarizer (Figure 43 (a)). The output SHG polarization was not specified. The SHG intensity as a function of θ is shown in Figure 43 (b) in red and black dots for (1) and (2) sample configurations, respectively.

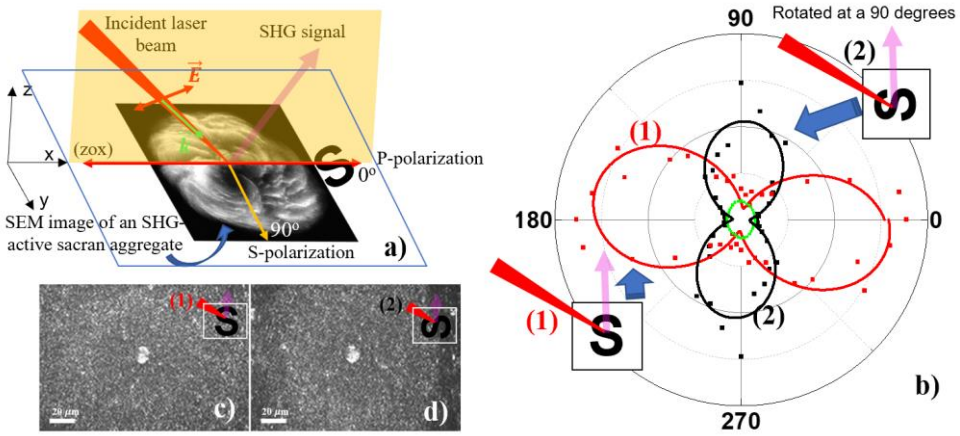

Figure 43. a) Polarization of incident laser beam for $\theta = 0^o$ (P-polarization), b) the polarization-dependent SHG intensity of the SHG-active sacran aggregates. Red and black dots and curves labeled (1) and (2), respectively, are data for the samples in two different configurations shown at the edges. The green square dots are 2PEF intensity. c) and d) S-polarized linear images corresponding to the (1) and (2) cases.

In Figure 43 (b) the red and black curves are fitting data using the formulation of

$$I_{SHG} \propto a\{(\sin^2\theta + b\cos^2\theta)^2 + c\sin^2\theta\cos^2\theta\} \text{ [167]} \quad (2\text{-}3)$$

Here a, b, and c are constants related to the third-rank tensor of the second-order nonlinear susceptibility $\chi^{(2)}$. One can see in Figure 43 (b) that the SHG intensity pattern is clearly anisotropic and that it rotates according to the sample is rotated. The reason for the different maximum intensity between (1) and (2) patterns is the difference in Fresnel factors when the incident electric field is in the optimum SHG emitting direction of the aggregate. The SHG intensity is determined as a function of the second-order susceptibility $\chi^{(2)}$. For the second-order optical phenomena on the surface, $\chi^{(2)}$ is a function of hyperpolarizability tensor $(\boldsymbol{\beta}^{(2)})$. [168], [169]

$$\chi_{ijk}^{(2)} = N_s \langle T_{ia} T_{jb} T_{kc} \rangle \beta_{abc}^{(2)} \quad (2\text{-}4)$$

Here N_s is the number density of contributing molecules, $\langle T_{ia} T_{jb} T_{kc} \rangle$ is the average transformation from the molecular coordinate frame (a, b, c) to the surface coordinate frame (*i, j, k*). Considering a molecular monolayer, the molecular orientation can be expressed based on the nonlinear susceptibilities $\chi_{zzz}^{(2)}$ and $\chi_{zyy}^{(2)}$ along a certain molecular axis $\hat{a}$

$$\chi_{zzz}^{(2)} = N \langle \cos^3 \phi \rangle \beta_{aaa} \quad (2\text{-}5)$$

$$\chi_{zyy}^{(2)} = \frac{1}{2} N \langle \sin^2 \phi \cos\phi \rangle \beta_{aaa} \quad (2\text{-}6)$$

where ϕ is the polar angle between aˆ and the surface normal $\hat{z}$

The 2PEF intensity shown in green in Figure 43 (b) has a circular shape as a function of the incident polarization angle and is much weaker than the SHG intensity. S-polarized linear images of the same SHG-active aggregate using white light as a function of the sample rotational angle around its surface normal are shown in Figures 43 (c) and (d). The last two results show that the aggregate looks isotropic in the linear optical and 2PEF phenomena.

Figure 43 (b) shows that the SHG intensity spots have a strong incident polarization dependence but the 2PEF intensity does not. It means that permanent dipoles of sacran molecules' aggregates are suggested to be aligned in one direction. The SHG pattern as a function of the polarization angle rotates by 90^o when the sample is rotated by 90^o. This confirms that permanent dipoles of sacran molecules' aggregates are aligned in one direction. The driving force of the alignment of the dipoles of sacran molecules is not clearly known yet. We can think of three candidate origins for such forces. The first one is a branching of sacran molecules like that in amylopectin. Amylopectin and amylose in starch are composed of α-D-glucose polymer with α -(1,4) glycosidic bonds. Amylopectin is SHG and SFG active because all the reducing ends are oriented in the same direction by

the effect of the branching by α -(1,6) glycosidic bonds. [170], [171] Amylose is SHG and SFG inactive because the saccharide chains have their reducing ends up and down by 50% each and the nonlinear polarization cancels. It is a probable candidate because it has been pointed out that multi-valent metal ions (like Ca in this paper) bind with carboxylate and sulfate groups in the sacran chain and serve as crosslinkers of different chains. [127] However, why there are two kinds of bundle structures with and without macroscopic dipole is not known yet.

The second candidate is a Coulomb force induced by the central cation. If the positive charge of the central cation is large it creates a Coulomb potential, and the potential will align the sacran molecules and their dipoles. However, this candidate has a problem in that it does not explain the uni-directional alignment of the dipoles in the SHG spot. The third candidate is a possible ferroelectric liquid crystal phase of sacran molecules. Sacran has abundant chiral units giving possible structures to form a ferroelectric liquid crystal (FLC). [172], [173] Permanent electric dipoles of the sacran chain can occur if the chain takes a spiral structure by the effect of the alternate alignment between non-chiral molecules and chiral ones. This random organization of molecules creates a layer dipole moment, and a helicoidal structure of chiral smectic C (SmC*) liquid crystal ferroelectric phase. [174] As another ferroelectric liquid crystal phase, a splay nematic phase is also reported. [175]–[177]

Figure 43 (b) shows that the symmetrical SHG patterns will change by 90^{o} when the sample is rotated by 90^{o}. It means that there exists an in-plane anisotropy in the SHG-active sacran aggregate. The hexagonal shape of SHG-active sacran aggregates is due to following the morphology of crystalline ice of water molecules. Still, water molecules have a degree of freedom of taking random directions, hence the average dipole of the water

molecules can be in one direction. The two-fold polarization dependence of SHG intensity explains the well-orientation of anion sacran chains around cation sacran chains that make the electric dipole. Changing the incident polarization of the laser, I found that SHG intensity will reach maximum when the external electric field parallels the molecular axis of sacran molecules. Figure 43 (b) shows the highest SHG intensity when incident polarization is at -30 degrees and repeats at 150 degrees (red pattern) or is near 90 degrees and repeats at 270 degrees (black pattern). That explains that numerous sacran molecules orient in the radial direction as an optical axis shown in figure 43 (b). This optical axis expresses the electric field vector of the local electric dipole. This electric dipole is the origin of a strongly observed SHG signal and is much higher than the SHG signal generated from oriented water molecules. Therefore, the SHG intensity reaches a maximum when external electric polarization is parallel to the local electric field vector and forms a two-fold polarization dependence of SHG intensity. The linear polarization dependence of this linear image of SHG-active sacran aggregate on incident white light was investigated and shown in Figure 44. An incident white light beam was S-polarized by using a polarizer and illuminated the surface of the sacran cast film. The SHG-active sacran aggregate was rotated around its surface normally with the steps of thirty degrees. Linear images in Figure 44 (e) indicate that the linear image does not depend on the rotational angle remarkably. When I rotate the sample, the incident polarization dependence of SHG intensity will not be affected.

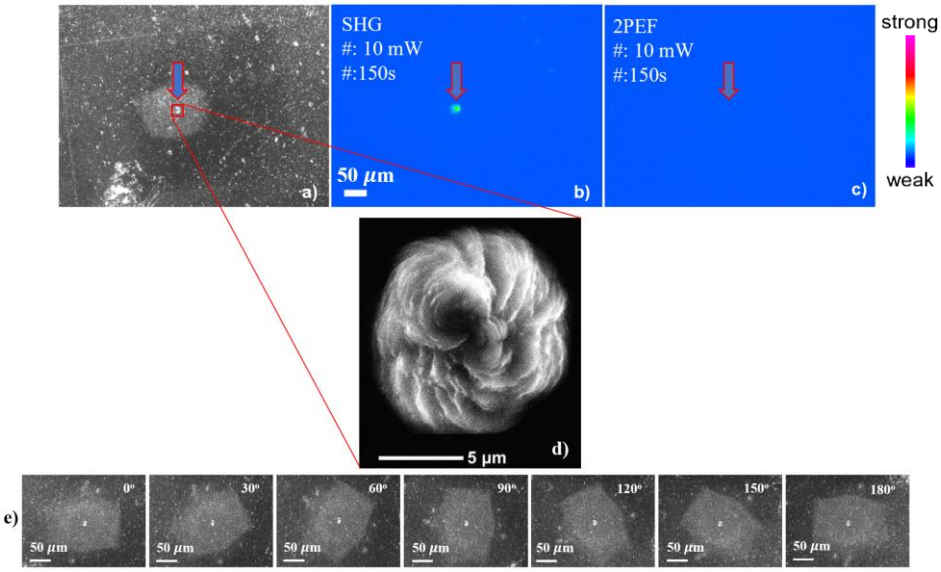

Figure 44. a) Linear, b) SHG, c) 2PEF, d) SEM images of an SHG-active sacran aggregate, e) sample rotation angle dependence of linear images under s-polarized white light illumination.

2.3.3. Nonlinear optical behavior and collecting heavy metal ion ability of sacran molecules

Here, I investigate the optical characteristics of ultrasonicated sacran solution using SHG microscopy. The original sacran solutions (0.5 wt%) were ultrasonicated at different sonication times (zero, 10, 20, 30, 40, 60, 300, 600, and 1800 seconds). The sacran cast films were created from ultrasonicated sacran solutions by drying at room temperature on the surface of silicon substrates. Sacran cast films were placed into the stage of SHG microscopy to scan the number of SHG spots and their density.

The density of SHG-active sacran aggregates

Using the microscopy imaging technique, I clarified the position of SHG spots from SHG images by comparing them with the corresponding linear and 2PEF images. The observed SHG spots are marked by the red circle in Figure 45, which shows the distribution of the SHG spots, linear white spots on the surface of the sacran cast films.

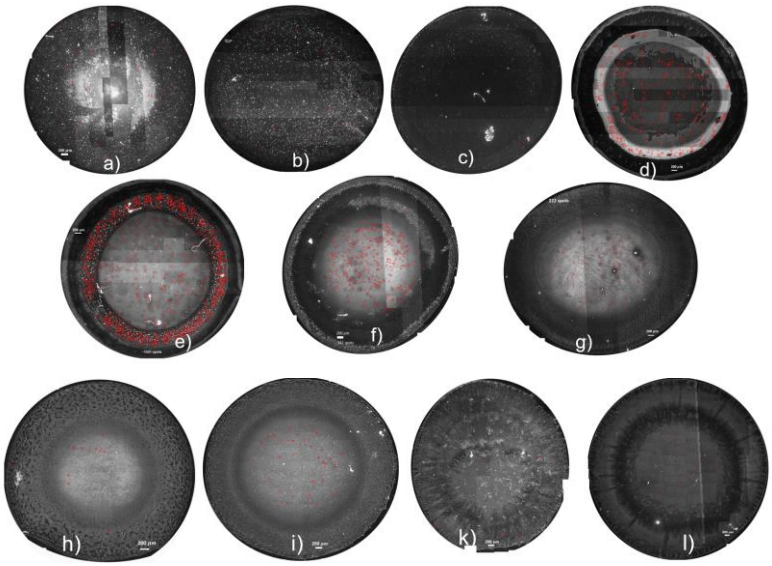

Figure 45. The linear image of sacran cast film undergoing different ultrasonication times and SHG micro-spots position (marked by the red circle). a) the residue part, b) the original sacran solution, c) after filtrated by membrane filter with 5 μm of pore size, d) 10 seconds, e) 20 seconds, f) 30 seconds, g) 40, h) one minute, i) 5 minutes, k) ten minutes, and l) 30 minutes of ultrasonication time.

In Figure 46, the density of the SHG spot over the entire area of the film with a diameter of 5 – 7 mm depends on ultrasonic energy is shown.

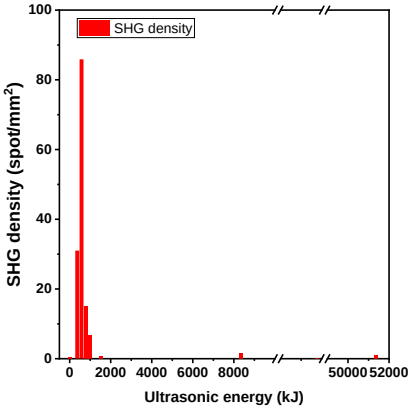

Figure 46. Ultrasonic energy-dependence of SHG spot density

Table 11. Ultrasonic energy in the ultrasonication treatment

time (s)	energy (kJ/mL)
0	0
10	7.2
20	12.2

30	16.9
40	22.7
60	41.2
300	359.57
600	1000.3
1800	5476.97

Figure 46 indicates the highest SHG spot density around the ultrasonic energy of 12.2 kJ/mL which corresponds to the SHG spot distribution in Figure 45 (e). In the case of 20-second ultrasonication time, the morphology of sacran cast film separates into two parts which are central and edge regions. I focused on the SHG response of sacran molecules with SHG spot distribution in the edge region (~176.23 spots/mm^2) much larger than the central region (~24.5 spots/mm^2). The SHG density roughly decreased after around ultrasonic energy 42 kJ/mL and got relative stability when the sonication time was longer than 1 min.

The nonlinear optical property of ultrasonicated sacran solutions

There are many studies conducted on the drying process of sacran, and structures of macrodomains in oriented uni-direction orientation have been pointed out. [125], [130]–[133] According to them, the mobility of microdomains of sacran aggregates can be controlled by controlling sacran molecular weight, concentration, and temperature. The macrodomains can extend up to milli-scale during drying and originate from the gas-liquid interface. Condition dependence of nonlinear optical properties of sacran molecules is investigated by combining the comparable second-harmonic generation (SHG), two-photon excitation fluorescence (2PEF), and linear imaging microscopy. The nonlinear optical action of sacran aggregates in cast films has been analyzed in which the distribution of SHG spots and linear sacran aggregates follow the coffee-ring effect law (Figure 47).

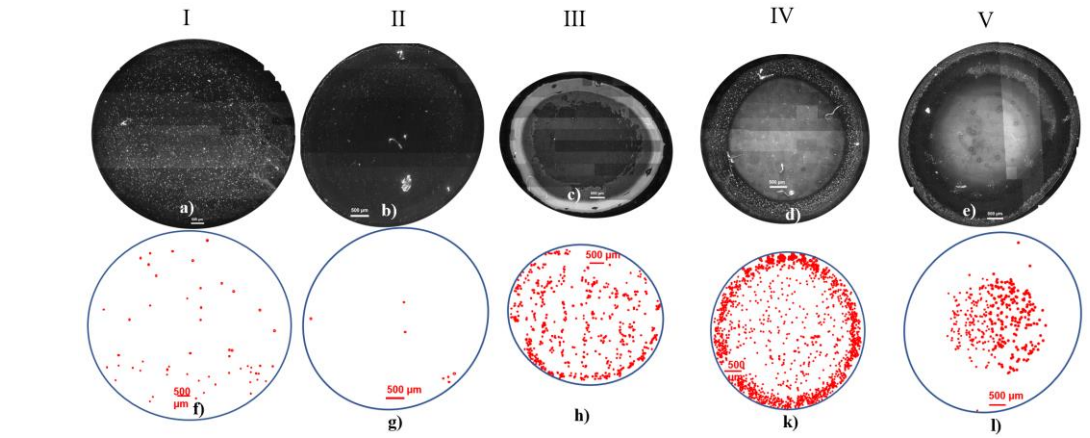

Figure 47. Linear and SHG spot distribution. I – Original sacran solution (0.5 wt%), II – zero seconds (the original sacran solution is filtered using membrane filter with 5 µm pore size), III – 10 seconds, IV– 20 seconds, and V – 30 seconds of ultrasonication time. (a) – (e) images show the distribution of white linear spots, and the distribution of SHG spots.

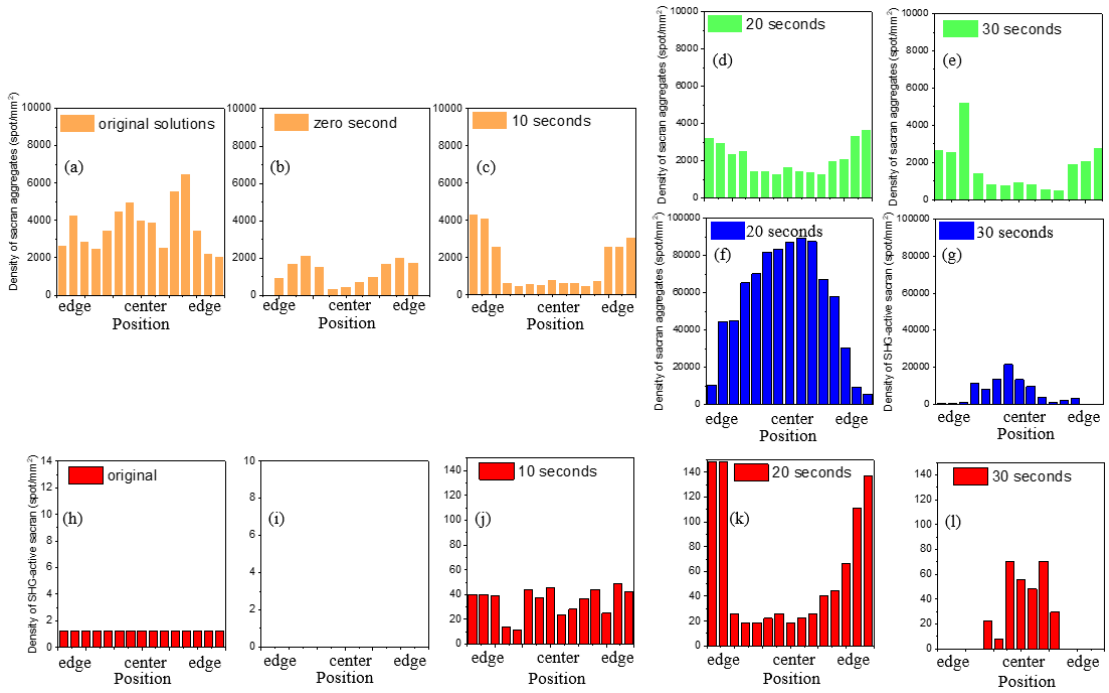

Figure 48. Illustration of sacran particle distribution by the bar diagram, linear (■:white sacran aggregates, ■:sacran aggregates size > 20 µm, ■: sacran aggregates size < 20 µm) and SHG-active (■) sacran aggregates

A scale bar of 500 µm is drawn below each figure. Figure 48 is a bar graph showing the particle number distribution and the SHG spot distribution in Figure 47. Particles are counted in successive squares of 600 x 300 µm on the equatorial line of each circle in

Figure 47. For samples of 20 seconds or longer ultrasonication time, particles with a diameter larger than 20 μm and particles with a diameter smaller than 20 μm were distinguished by two different color bar graphs.

First, I look at the black-and-white CMOS camera image in which the sample is excited only with a white lamp. In Figure 47 (a), the white particles are uniformly distributed over the entire area of the film with a diameter of several mm. In the film, not only this granular structure but also a continuous component that does not appear in the image is deposited over a thickness of about 50 μm. In Figure 47 (b), there are not many particulate components, but a detailed count reveals a ring-like distribution, as shown in Figure 48 (b). Figs. 48 (a) to (g) show the bar graphs of white spot distribution in the cast films made from (a) the original sacran solution, (b) non-ultrasonicated sacran solution filtered by membrane filter of 5 μm pore size, (c) 10 seconds, (d, f) 20 seconds, and (e, g) 30 seconds of ultrasonication time. The orange bar graphs imply the density of white spots. The green bar graphs represent the density of white spots of sizes larger than 20 μm. The blue bar graphs show the density of white spots of sizes smaller than 20 μm. Figs . 48 (h) to (l) show the bar graphs of SHG-active spot distribution in the cast films made from (h) the original sacran solution, (i) non-ultrasonicated sacran solution filtered by membrane filter of 5 μm pore size, (j) 10 seconds, (k) 20 seconds, and (l) 30 seconds of ultrasonication time. All the ultrasonicated sacran solutions were filtered by membrane filter of 5 μm pore size.

Here we note that the distribution of white spots in Figs. 48 (a) to (g) and that of SHG spots in Figs. 48 (h) to (l) are not the same as each other. Namely, the uniform distribution of white spots is observed in only Fig. 48 (a), while the uniform distribution of SHG spots is seen in Figs. 48 (h) and (j). The ring distribution of white spots is observed in Figs. 48

(b) to (e), while the ring distribution of SHG spots is observed only in Fig. 48 (j). Center bump shapes of white spots are observed in Figs. 48 (f) and (g), while center bump shapes of SHG spots are seen in only Figs. 48 (l). These results suggest that the sacran molecules behave in different ways in the solution before they become white spots in the linear image and SHG spots in the nonlinear images after drying. The particles whose number increased due to sonication observed in linear images are likely to be micro balls. [128]

The coffee ring effect has been modeled by many researchers; Figure 49 shows a typical example by Bhardwaj et al. [178], [179]

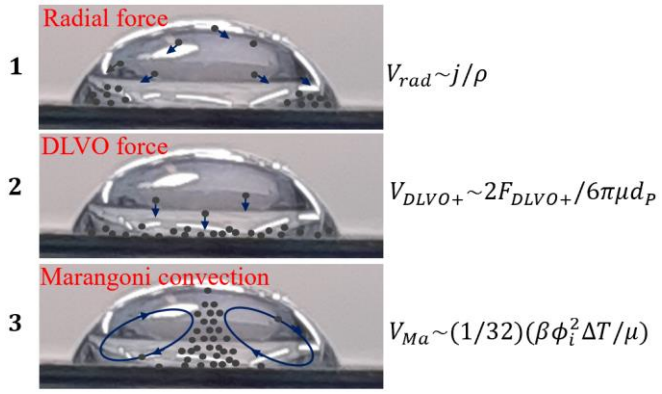

Figure 49. Three convective mechanisms compete to form the deposition patterns of cast films.

According to this model, particles in an aqueous solution undergoing the drying process are affected by three types of effects: (1) a ring-like structure at the edge of the cast film due to radial flow driven by a maximum evaporation rate, (2) a uniform deposit form is driven by DLVO (Derjaguin-Landau-Verwey-Overbeek) attractive force between the particles and the substrate, and (3) Marangoni recirculation forms a central bump structure. The DLVO attractive force is proposed by four physicists Boris Derjaguin, Lev Landau, Evert Verwey, and Theodoor Overbeek. The DLVO force is the sum of the electrostatic and van der Walls forces. [179] The effect (1) occurs because the edge region of the droplet dries faster than the central region and a concentration gradient occurs. The

osmotic pressure difference causes the inner aqueous solution to move toward the edge. The effect (3) is called Marangoni convection, and the speed at which particles gather at the center is due to differences in surface tension depending on the location. These three effects occur in competition, and their relative strengths can be arranged using a phase diagram (Figure 50). [179]

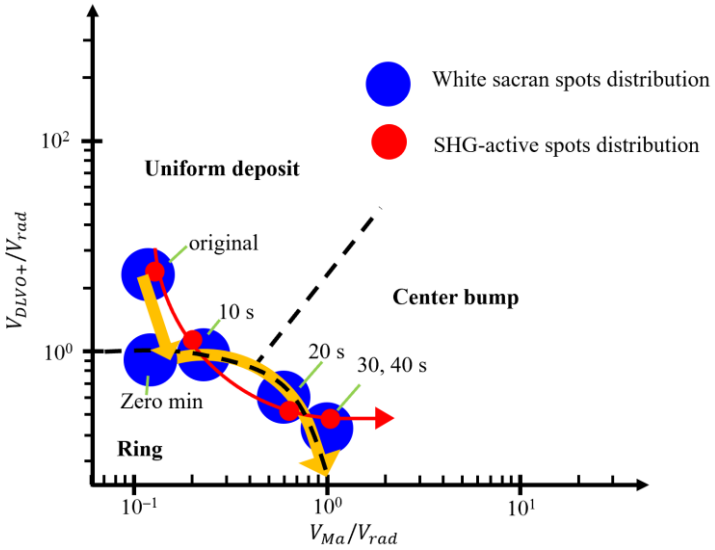

Figure 50. Changing linear and SHG-active sacran aggregates on ultrasonication time and correlated to the velocity ratio V_{DLVO+}/V_{rad}, V_{Ma}/V_{rad}

Figure 50 is a phase diagram presented by Bhardwaj *et al*. The horizontal axis in Fig. 7 represents the Marangoni convection velocity (V_{Ma}) divided by the radial velocity (V_{rad}), and the vertical axis is the DLVO+ velocity (V_{DLVO+}) divided by V_{rad}. The phase diagram in Fig. 7 is assumed to be separated into three zones based on the equilibrium condition of velocity ratios of V_{DLVO+}/V_{rad} and V_{Ma}/V_{rad}as uniform deposit zone (upper left), ring-shaped zone (lower left), and central bump zone (upper right). We schematically plot the status of each cast films with blue and red filled circles. As noted by the paper's authors, these phases are supposed to leave behind the drying marks that authors give to their names.

Deposit patterns of linear white sacran spots in blue areas (●) and deposit patterns of SHG-active spots in red areas (●) change from uniform to the ring and then central bump according to the increase of ultrasonication time from 0 to 40 seconds. The orange and red arrows are guide to the eyes of these changes. The orange arrows express the change of deposition of linearly observed white sacran spots in the cast films. The orange arrows indicate that the ring shapes and central bumps coexist for ultrasonication time longer than 40 seconds. The red arrow implies the change of deposition patterns of SHG spots in the cast films. On this phase diagram, the patterns of the linearly observed white spots of sacran split into two shapes for the sonication time of equal or longer than 20 seconds. The phase of the patterns of the SHG spots is in the ring domain at the sonication time of 20 sec, but enters the central bump domain at 30 and 40 sec. The distribution of SHG spots of sacran cast film, made by sacran aqueous solution passed through a filter with a pore size of 5 μm, is not shown in Fig. 50 because of its SHG response was very weak (Figure 47 (g)).The particles (including linear and SHG spots) are in a uniform distribution in the non-sonicated sacran membrane (Figure 47 (a, b), 48 (a, h, and j)). There is a uniform distribution and ring-shaped mixing (Figure 47 (c), 48 (c)) for 10 seconds of ultrasonic treatment, center bump and ring-shaped mixing for 20 seconds (Figure 47 (d), 48 (d) and (f)), and 30 seconds (Figure 47 (e), 48 (e) and (g)). Red circles indicate the distribution of SHG spots excited by femtosecond laser light with a wavelength of 800 nm. Uniform SHG spot distribution for 10 seconds of treatment (Figure 47 (h), 48 (j)), ring-shaped SHG spot distribution for 20 seconds of treatment (Figure 47 (i), 48 (k)), and central center bump shaped SHG spot distribution for 30 seconds of treatment (Figure 47 (k), 48(l)).

For example, the transition of the state of SHG spot distribution as the increase of ultrasonication time will be the one drawn by the red arrow in Figure 50. This red arrow

implies the tendency of sacran particle distribution. At longer ultrasonication times, the distribution of dried sacran aggregates of the sacran film changes from the top left to the right of the phase diagram. On this phase diagram, it seems that the transition of the phase of the SHG spot has a slightly delayed effect on the treatment time than the phase of the linear fine particle distribution.

Next, I will consider why the phase of the SHG spot has a temporal delay with respect to the ultrasonic treatment time due to the linear distribution of fine particles. The SHG spot moved along the surface of the sacran aqueous solution film. On the other hand, linear microparticles are generally considered to move freely up and down in the aqueous solution bulk. [125] When the ultrasonicated treatment is applied, the molecular weight of sacran decreases markedly (Table 9) because ultrasonic energy disrupts sacran chains into much shorter ones. The viscosity of ultrasonicated sacran solution decreases when treated with ultrasonic waves, the evaporative mass flux j in $V_{rad} \sim \mathrm{j}/\rho$ becomes larger, and therefore V_{rad} also increases. Here ρ is the density of drop liquid. However, it is conceivable that the SHG-emitting fine particles caught on the surface are subject to two-dimensional interference from other particles on the surface so that V_{rad} does not increase. However, if the treatment time is longer than 20 seconds, V_{Ma} also increases, and if the effect is greater than the effect on V_{rad}, V_{Ma}/V_{rad} will increase, and the state of the aqueous solution and drying marks will shift to the right in Figure 49. The localization of sacran microparticles exhibiting SHG spots on the surface of the aqueous solution is thought to be due to the electrochemical effect of the cation at the center. [180]

For ultrasonication time longer and equal to 40 seconds, the SHG spot's distribution is kept at the central region because the Marangoni effect is much more effective than radial force and because of the very low viscosity of ultrasonicated sacran solutions. Linear

sacran spot distribution is still separated into two groups (i) center-bump with the smallest size sacran aggregates and (ii) ring-like structure at the edge region with larger size sacran aggregates.

Sacran adsorbing Er^{3+} and Nd^{3+} metal ions.

Sacran aqueous solution at a concentration of 0.5 wt% is dropped into solutions of Nd^{3+} and Er^{3+} metal ions and formed gel beads of sacran/metal ions. According to the previous study, [137] the metal-adsorbing process of sacran chains is a substitution of one or two Cl^- anions of $NdCl_3$ or $ErCl_3$ molecules with the polysaccharide sacran anions. Metal ions adsorption capacity is evaluated by the ratio between the residual metal ions of original metal ions solutions and metal ions adsorbed from the gel. Metal ions are thought to bind to the polysaccharide anions and take the role of a bridge to connect sacran chains together. [124], [140] Although the orientation of the sacran chains suggested that they did not change in the gel beads, the effect of metal ions on the SHG response of sacran aggregates hasn't been studied yet. The bonds between sacran chains formed by metal ions can disturb the initial orientation of sacran chains of the SHG-active and change the strength of the local electric dipole and/or establish a new local electric dipole. Trivalent efficient metal-adsorbing (Nd^{3+} and Er^{3+}) of sacran aqueous solutions is investigated using SHG microscopy, and the results are shown below.

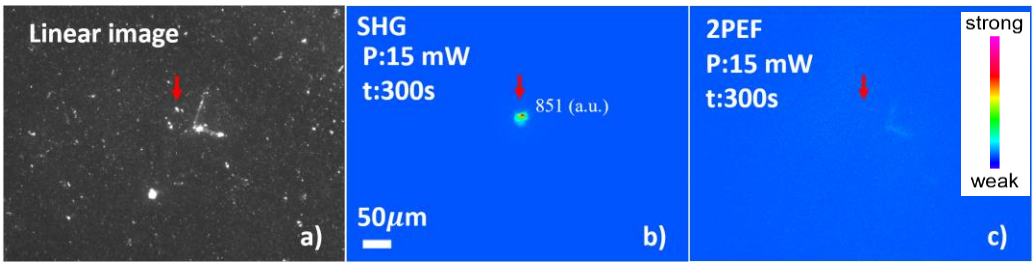

Figure 51. Linear, SHG, and 2PEF images of the original 0.5 wt% sacran solutions (13 spots)

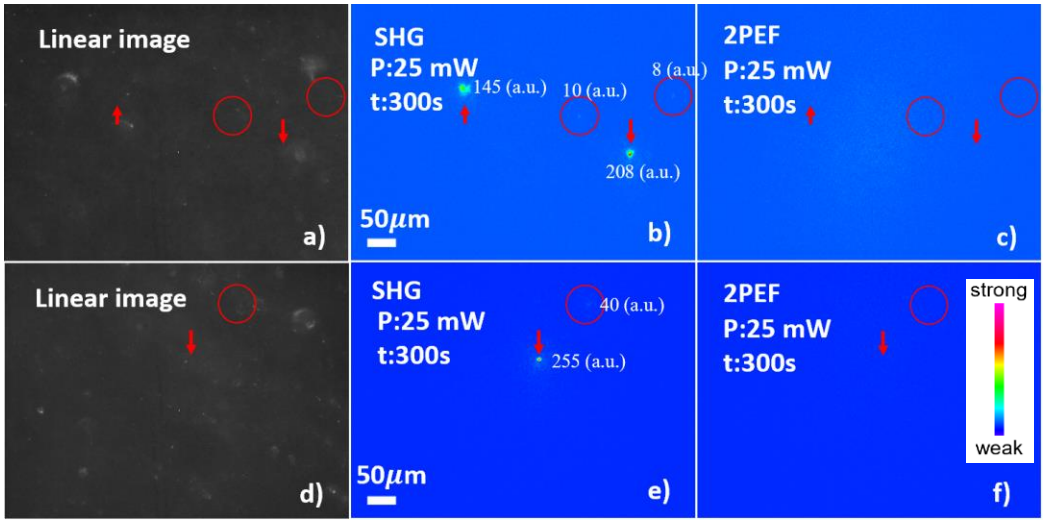

Figure 52. Linear, SHG, and 2PEF images of the original sacran solutions absorbed metal ions, (a-c) Er^{3+} (32 spots), (d-f) Nd^{3+}(23 spots)

Figure 51 shows the SHG spots observed from SHG-active sacran aggregates in cast film made from original sacran aqueous solutions (0.5 wt%) and their linear, 2PEF images. Figure 52 shows linear, SHG, and 2PEF images of the original sacran (0.5 wt%) absorbed Er^{3+} (Figure 52 (a) – (c)) and Nd^{3+} (Figures 52 (d) – (f)). In the first linear image of the original sacran solution (Figure 51 (a)), the white spots are quite clear and not blurred. The SHG spots at the corresponding position of the SHG image (Figure 51 (b)) also have the highest intensity and the narrowest peak. That means that the SHG-active sacran aggregates are located nearly on the surface of the cast film and are adjusted to match the focus plane of the objective lens. However, there is little difference in the metal-adsorbing of sacran cases. The very sharp peak of the SHG spot in Figures 52 (b) and (e) indicates the SHG-active sacran aggregates are located at the focus plane of the objective lens. However, those correlated white spots in linear images (Figures 52 (a) and (d)) are out of high resolution. That means that the SHG-active sacran aggregates are below the surface layer of the sacran cast film and the film thickness is much greater than the objective lens' depth of focus (table 7). The depth of the SHG-active sacran spot is estimated around 80 -

90 μm. I investigated the position of SHG-active sacran aggregates and whether they are on the surface of the cast film. The sample is sacran cast film made from metal-adsorbing of original sacran aqueous solutions (0.5 wt%). The result indicates that some SHG-active sacran aggregates are completely located within the cast film shown in Figure 53.

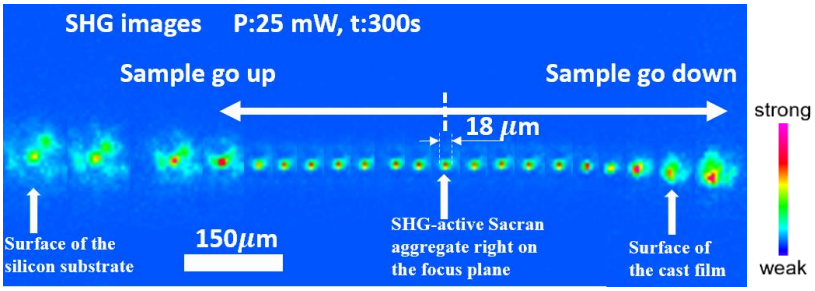

Figure 53. Position dependence of the shape of the SHG spot when the stage of microscopy is adjusted to go up and go down using the fine focus adjustment knob.

I changed the stage position of the microscope to go up and down (z-direction). I found that the SHG-active sacran aggregate is located between the surface of the cast film and the silicon substrate at the position in which the size of the SHG spot is the smallest (estimated at around 18 μm) (Figure 53). In this study, the thickness of the cast film made from absorbing metal ions sacran solution (0.5 wt%) estimated at around 180 μm which is larger than the thickness of cast film made from original sacran aqueous solutions (0.5 wt%) estimated to be around 50 – 70 μm.

The number of SHG spots and their intensity will also reflect the effect of adsorbed metal ions on the nonlinear response of sacran molecules. The number of SHG spots in metal-adsorbed sacran aqueous solutions slightly increases compared to the original sacran aqueous solutions. Nevertheless, although incident laser power was adjusted around two times higher, the observed SHG intensities in Figures 52 (b) and (e) (208 a.u. and 255 a.u.) are lower than the observed SHG intensity in Figure 51 (b) (851 a.u.). Adsorbed metal cations combine with the sacran anions and reduce the strength of the initial local electric field of the original SHG-active sacran aggregates. On the other hand, several weak SHG

spots are also observed in the SHG images. There is a candidate suggested that multi-cations $[NdCl_2]^+$, $[NdCl]^{2+}$, $[ErCl_2]^+$, $[ErCl_2]^{2+}$, and even Nd^{3+} and Er^{3+} link to the sacran anions and fabricate the new weak electric dipoles that generate weak SHG signals.

2.4. Conclusion

The SHG response of original, ultrasonicated sacran solutions and metal-adsorbed sacran are observed by using SHG microscopy. Sacran molecules simultaneously allow the SHG phenomenon because of noncentrosymmetric and chiral structures and the third-order nonlinear phenomenon – two-photon excitation fluorescence (2PEF). The imaging microscopy combines SHG, 2PEF, and linear images to determine the SHG-active sacran aggregates in the sacran cast films. On the other hand, the second-order nonlinearity of the SHG signal is demonstrated by the power-dependence investigation of SHG intensity. The SHG intensity of sacran molecules is proportional to the incident laser intensity square. Multiphoton excitation fluorescence experiments are also performed to ensure no three- and fourth-photon excitation fluorescence process.

The shape of SHG spots has a spotty-like structure with the highest intensity at the center of the spot. It reflects the structure of the local electric dipole with sacran cations at the center of the SHG spot and sacran anions oriented around. The one-dimensional oriented structure of sacran chains in the SHG-active sacran aggregates is demonstrated by the polarization dependence experiment. The intensity of the SHG spots has a strong incident polarization dependence because of several reasonable candidates as (i) the branch structure of sacran chains, (ii) the Coulomb force from the electric dipole orient the sacran anions, (iii) the ferroelectric liquid crystal phase might have existed inside the SHG-active sacran aggregates. By contrast, the 2PEF intensity shows the incident polarization independence.

The distribution of SHG spots and linear sacran spots in the cast films is analyzed. SHG spot distribution changes from the uniform deposition (the original sacran solution and 10 seconds of ultrasonicated sacran solution) to the ring shape at the boundary of cast film (20 seconds of ultrasonicated sacran solutions) and finally transit to the center-bump structure when ultrasonication time is longer than 20 seconds. However, the distribution of linear sacran travels from uniform (the original sacran solution) to ring-like after 10 seconds of ultrasonication time and then separates into a center bump with a spot size of fewer than 20 μm and a ring shape at the edge of the cast film with a spot size larger than 20 μm.

In the trivalent metal-adsorbed sacran solutions, there are more observed SHG spots but weaker intensity, where Nd and Er ions are absorbed. The hypothesis is that metal ions connect with the sacran anions and take them away from the initial SHG-active sacran aggregates reducing the intensity weaker and might constitute new electric dipoles that give extremely weak SHG spots.

3. Chapter 3. Modeling oriented structure of SHG-active sacran aggregates on a molecular scale

3.1. Combining optical experiments and electron microscopy experiments

SFG experiment

SFG microscope is a powerful tool for the analysis of the structure of biomaterials. Derived from the second-order nonlinear optical response of sacran molecules, the surface structure of sacran cast film should have included the chiral structure and contribution of functional groups such as CH_2, CH_3, and OH, ... This dissertation involves demonstrating the SFG-activity of sacran aggregates by using a sum frequency generation spectroscopy shown in Figure 54.

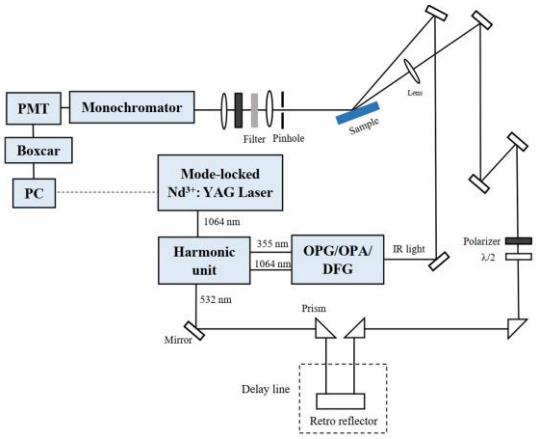

Figure 54. SFG experimental setup

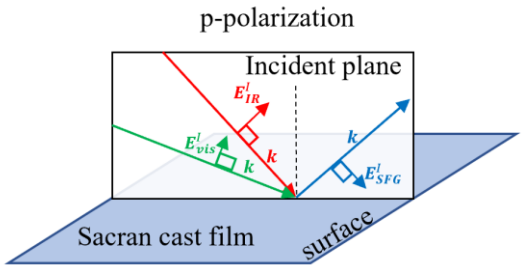

Figure 55. Schematic illustration of PPP combination

One of the excitation lights is the visible (Vis) light at a fixed wavelength of 532 nm with a pulse width of 30 ps generated from a mode-locked Nd3+:YAG laser (PL2143B,

EKSPLA). The other is the IR light generated from an optical parametric generator (OPG) (PG401/DFG2-18P, EKSPLA) scanned in the range from 2600 cm^{-1} to 3500 cm^{-1}. The pulse energy of the visible light was set up at 80 μJ, and that of the IR pulse was about 150 μJ. The observation area was ~1mm^2 on the film surface so it contained many SHG and hence SFG-active spots. The SFG spectra were measured with different input/output polarization combinations (PPP) shown in Figure 55.

Scanning electron microscopy and dispersive X-ray – scanning electron microscopy experiments

SEM images of SHG-active sacran aggregates were observed using a NeoScope JCM-6000Plus, JEOL. For energy-dispersive X-ray - scanning electron microscopy (EDX-SEM) analysis, I used TM3030Plus Miniscope-Hitachi. For high-resolution SEM images, dried cast films of sacran were coated with a gold layer of around 25 nanometers.

3.2. Results and discussions

SHG of selected sacran aggregates

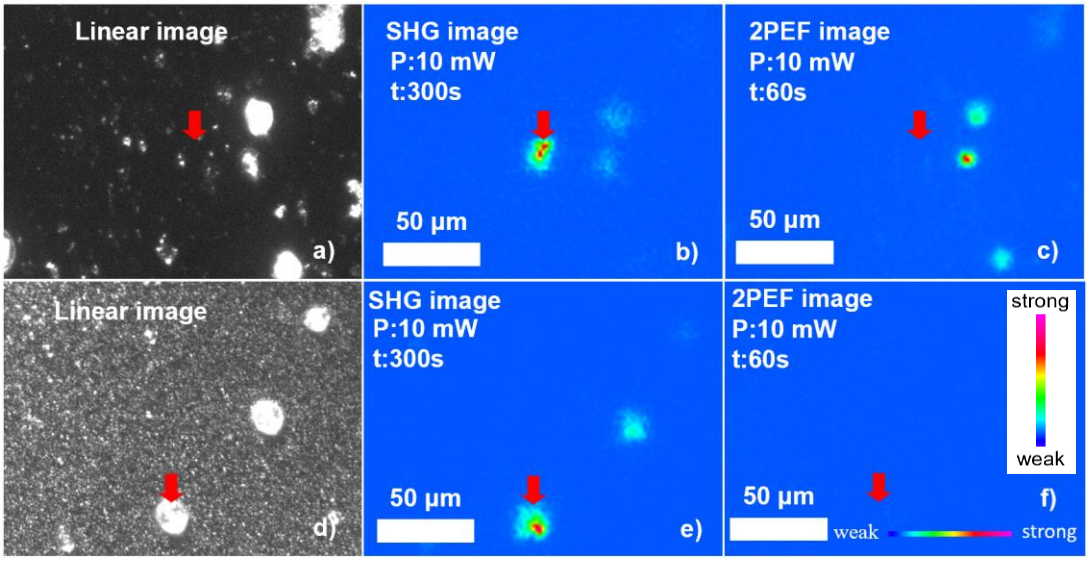

Figure 56. Linear, SHG, and 2PEF images observed from sacran cast films made from original sacran aqueous solutions ((a), (b), (c)), and from 30-second ultrasonicated sacran solutions ((d), (e), (f)), respectively. P and t represent excited laser power and integration time for image acquisition, respectively

Figure 56 shows optical linear, SHG, and 2PEF images of dried cast films made from original and ultrasonicated sacran solutions. In these figures, sacran is distributed in the whole scope of view. Yet, strong SHG signals in Figures 56 (b) and (e) were observed only near the center region of the cast film. The red arrows mark the positions of the spotty SHG signals in the SHG images (Figure 56 (b, e)). I do not see any 2PEF signal at the red arrowed positions in Figure 56 (c) or (f) and so I identified the spots in Figures (b) and (e) as SHG. If we see similar images at both 400 nm and 438 nm, the light at 400 nm can be from a tail of 2PEF. In the linear image Figure 56 (a) of the film made from the original sacran solution, nothing is seen at the position indicated by the red arrow. This is the reason why I could not try to see SEM images of this sample. On the other hand, in the linear image Figure 56 (d) of the film made from the sonicated sacran solution, a clear spot is seen at the position indicated by the red arrow. Hence, I did SEM observation of this sample as in the next section. The SHG active aggregates in the film made from sonicated sacran solution have the size of a few to 20 μm in the linear image.

In the case of 10 seconds of ultrasonicated sacran aqueous solution, SHG signals appeared with more complex shapes such as rod-shaped or with quite uniform intensity between the center and the edge regions. SHG intensity significantly decreased at ultrasonication time longer than 40 seconds.

The hexagonal structure of SHG-active sacran aggregates

Figure 57 shows linear, SEM, SHG, and 2PEF images of SHG-active sacran aggregates of ultrasonicated sacran solution of 20 seconds (a) to (d) and 30 seconds (e) to (h). Figures 57 (a), (c), (d) as a group, and (e), (g), (h) as a group is shown on the same scale, and Figures 57 (b) and (f) are expanded. In the linear image of Figure 57 (a), I see a particle with a diameter of 13 μm, although its contrast is not uniform. The SEM image shows

some multilayer symmetric structures with different diameters. In the SHG image of Figure 57 (c), I see two spots. The left spot has an intense peak at its center and its position is indicated by a white arrow. Figure 57 (g) shows a spot with higher intensity near the center of the spot. In the 2PEF images in Figures 57 (d) and (h), almost nothing is seen. Sacran sometimes gives both SHG and 2PEF as in Figures 57 (g) and (h). However, the 2PEF intensity in Figure 57 (h) is much weaker than the SHG intensity (Figure 57 (g)) and has a broad distribution instead of a sharp peak (Figure 58 (d)).

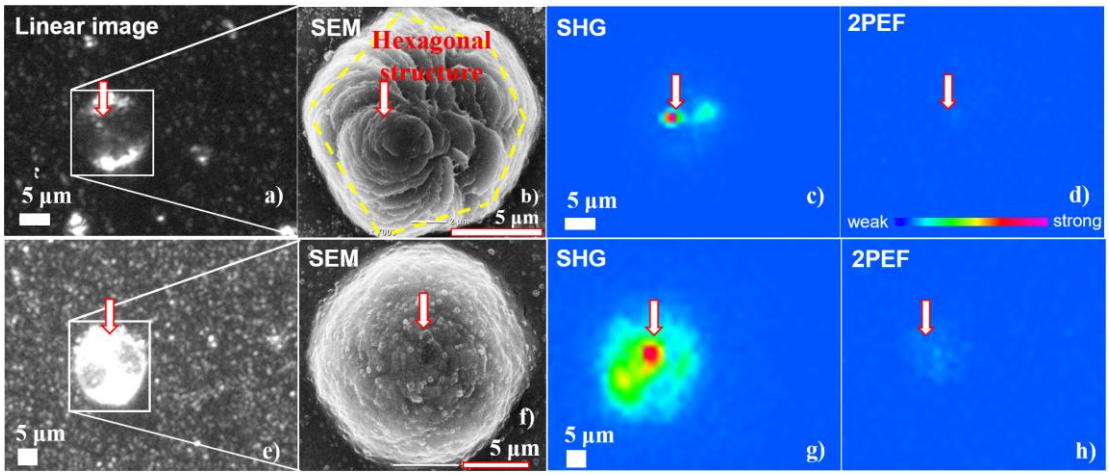

Figure 57. The linear, SEM, SHG, and 2PEF images of SHG-active sacran aggregates with the size of 13 µm (b), and 15 µm (f).

The power dependence of the SHG signal was a quadratic function (Figure 58 (e)). Multi-photon fluorescence was investigated by using a bandpass filter of 370 nm and 390 wavelengths and no signal was seen at all (Figure 58 (h) and (k)). Hence there is no three or four-photon-excited fluorescence under the current excitation power. These indicate that the signal detected in Figures 57 (c) and (g) is SHG. SEM images in Figures 57 (b) and (f) are observed frequently for ultrasonicated sacran solutions.

Figure 58 (d) shows the 2PEF image in Figure 57 (h) multiplied by a factor of 5. Figure 58 (d) indicates that the 2PEF signal has a broad shape instead of a sharp peak as in Figure 58(c). While in Figure 58 (c) (SHG image) shows a yellow part (pointed out by the red

arrow) near the center of the spots with much higher intensity than the surrounding area and the signal intensity at the correlation position in the 2PEF image. It indicates that the observed signal of Figure 58 (c) is the SHG signal.

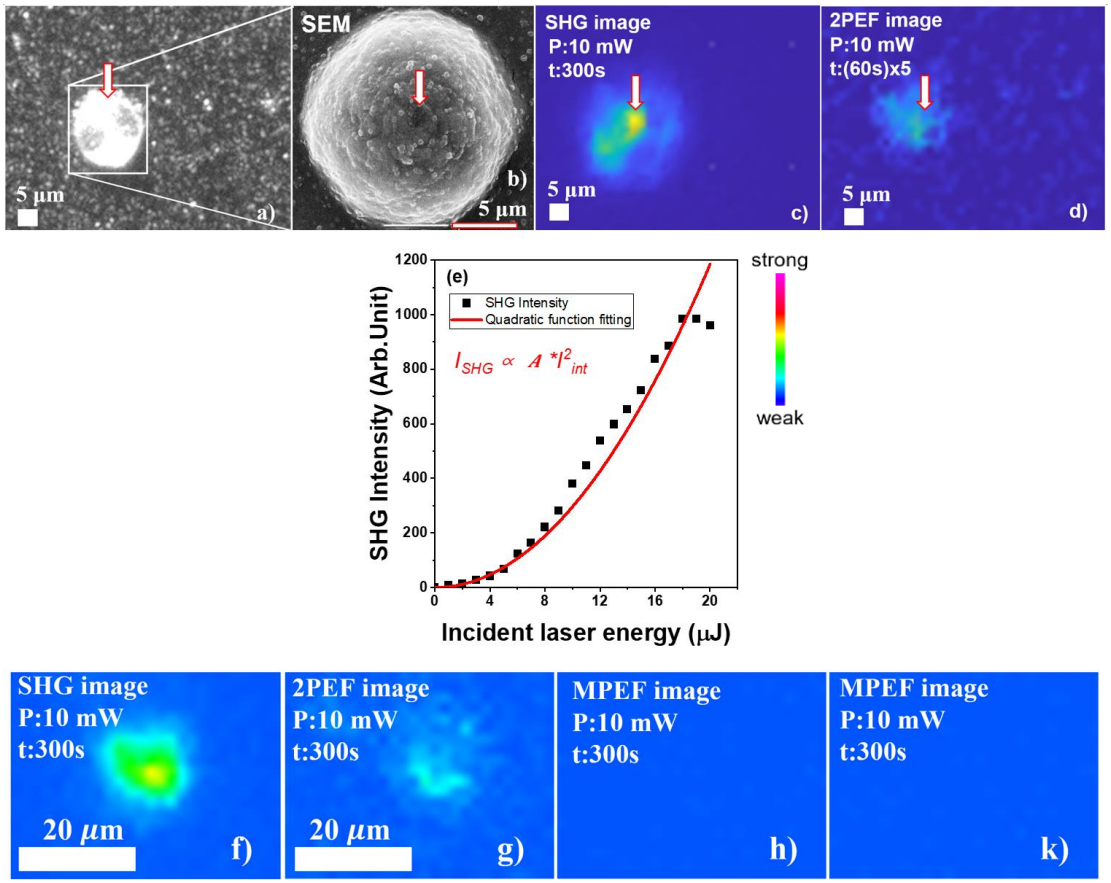

Figure 58. a)-d) the linear, SEM, SHG, and 2PEF (multiplied by 5) images. e) the incident power dependence of the SHG intensity of the SHG-active aggregate in Figure 7 in the main text. f)-k) the SHG, 2PEF, and multi-photon excited fluorescence images of another SHG-active aggregate of the original sacran solution.

The SHG intensity is proportional to the square of the incident laser power at less than 18 μJ: $I_{SHG} \propto A * I_{int}^2$. A is a constant (A= 2.963 ± 0.089) and the adjusted regression and residual (r-square) is around 0.957.

The SEM images in Figure 57 (b) and (f) show the shape of the SHG-active sacran aggregates frequently observed from ultrasonicated sacran solutions. The shape of the particle in Figure 57 (b) looks roughly hexagonal and is called a hexagonal structure.

Typical images of hexagonal structures are seen in Figures 59 (a), (c), (e), and (g), besides some other complex-shaped structures in Figures 59 (b), (d), (f), and (h), among the SHG active spots of ultrasonicated sacran aqueous solutions of 10, 20, 30, and 40 seconds, respectively. There are differences in the size of hexagonal structures observed, which range from ten micrometers to sixteen micrometers.

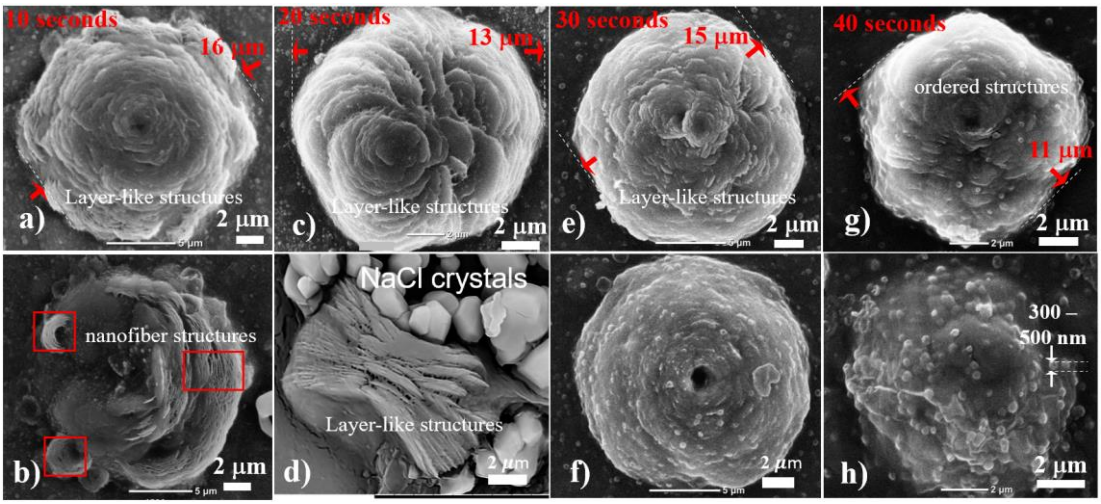

Figure 59. SEM images of hexagonal and highly ordered structures of the SHG-active sacran aggregates in the cast films made from sacran aqueous solutions of different ultrasonication times of (a, b) 10, (c, d) 20, (e, f) 30, and (g, h) 40 seconds.

In Figure 59 (a) at 10 seconds of ultrasonication time (input energy 7.2 kJ/ml), fibrous sacran is seen in the edge region of the hexagonal particle. [127], [125], [131]–[133] Microdomains, forming layer-like structures are arranged frequently around some centers, most typically holes as seen in Figures 59 (a), (b), (f), and (g). [161], [125], [181] Nanofiber sacran structures disappeared at higher ultrasonic energies than 12.2 kJ/ml (20 seconds of ultrasonication time). When ultrasonication time is 10, 20, and 30 seconds, hexagonal particles like those in Figure 59 (a), (c), and (e) appear prominently on the surface of the sacran cast film. With higher ultrasonic energy (~24 kJ/ml), many smaller particles with submicron sizes appear on the surface (Figure 59 (g, h)), and there were no hexagonal-shaped SHG-active aggregates. These hexagonal structures are rather 2D

particles or pancake shapes of roughly D_{6h} symmetry and the central holes look like the symmetry axes in Figures 59 (a), (b), (e), (f), and (g). In addition, in Figure 59 (d) the particle appears to have shrunk into a two-dimensional sheet when water was removed by drying, so its thickness is suggested to be thin.

These microdomain structures are speculated by assembled negative sacran well oriented around the central positive sacran. The organization of microdomain structures might follow the amorphous solid form of water molecules and is regularly arranged in a hexagonal lattice as a crystalline of ice. Besides that, the water molecules are aligned with a more polar-ordered hydrogen-bonding water network on the surface of sacran aggregates and allow the second-order nonlinear phenomena to occur. On the other hand, the hexagonal structure can be related to the crystalline phases containing hexagonal spiral structures of saccharide chains such as those of amylopectin. Therefore, the hexagonal structure can enhance the SHG signal.

The bottom row of Figure 59 shows some SHG-active sacran particles with complicated shapes in SEM images. The white polyhedral structures in Figure 59 (d) are believed to be NaCl crystals since chemical element analysis in Figure 60 showed Na species.

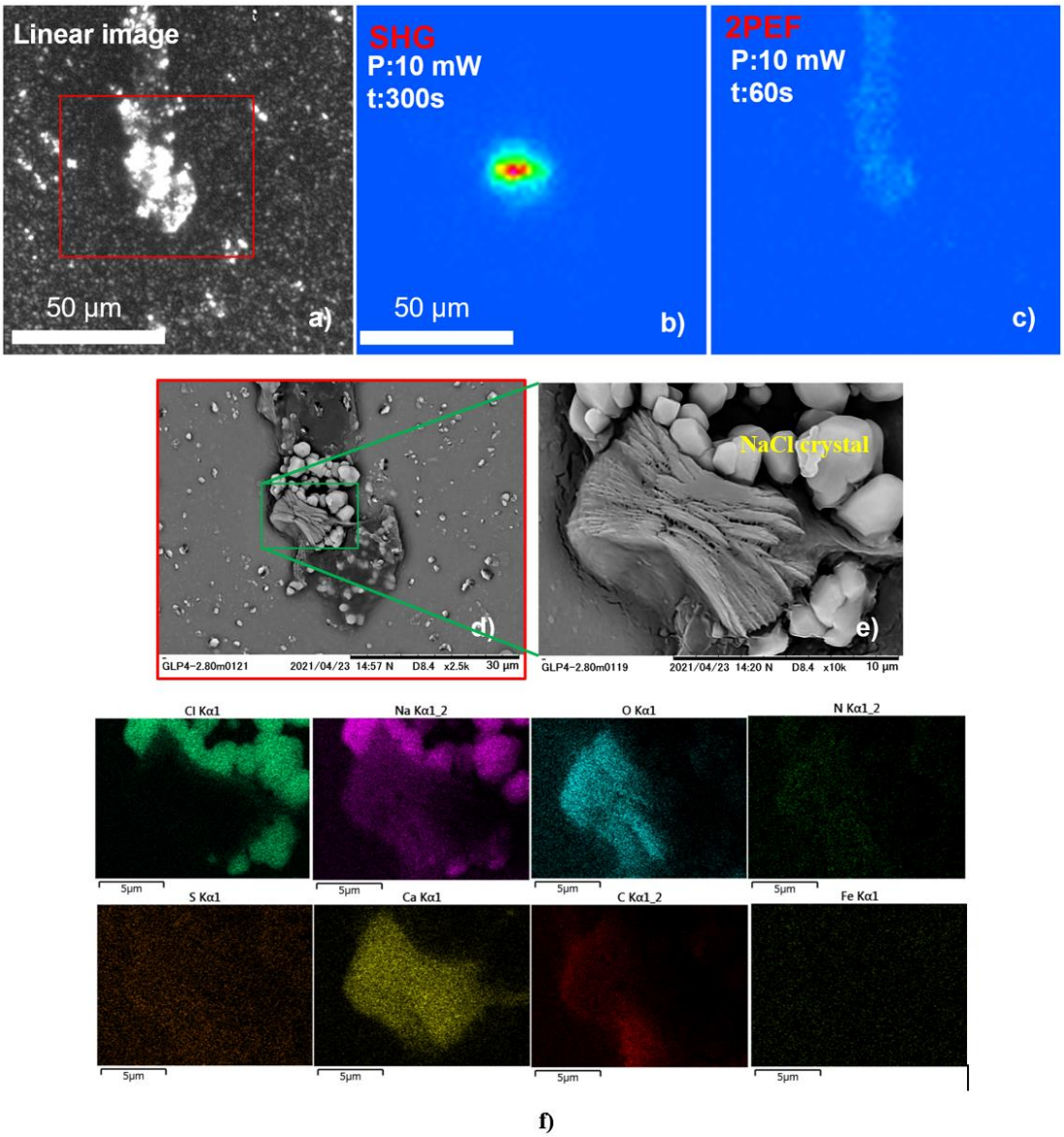

Figure 60. a), b), and c) Linear, SHG, and 2PEF images, respectively, d) and e) SEM images, f) the map data of the chemical element analysis, of an SHG-active sacran aggregate.

The sample is the sacran cast film as shown in Figure 59 (d) made from a sacran solution for 20 seconds. The chemical element data indicate that the white particles in Figure 60 (e) consist of Na and Cl elements. These particles should be sodium chloride salt crystals.

To examine the constituent chemical elements of the SHG-active hexagonal sacran aggregate in Figure 59 (c), I show its EDX-SEM element map in Figure 61. The four

elements C, O, S, and N are major elements making up sulfate, carboxyl, and amide groups in sacran. In particular, the existence of element S proves that the SHG-active hexagonal structures are sacran aggregates. EDX-SEM results of aggregates from other ultrasonicated sacran solutions were similar. From Figure 61 the atomic percentage ratio (r) between Na, Ca, and S was obtained. I found that the areas without SHG signals had the ratio $r_{Ca/S} <$ 1, while that with SHG-active spot had a ratio larger than 4 ($r_{Ca/S}$ >4). Those ratios for the Na element ($r_{Na/S} = 4 \sim 8$) were roughly uniform in all the areas.

$$r_{\mathrm{Na,Ca}/\mathrm{S}} = \frac{\text{Atomic \% of Na or Ca}}{\text{Atomic \% of S}} \tag{3-1}$$

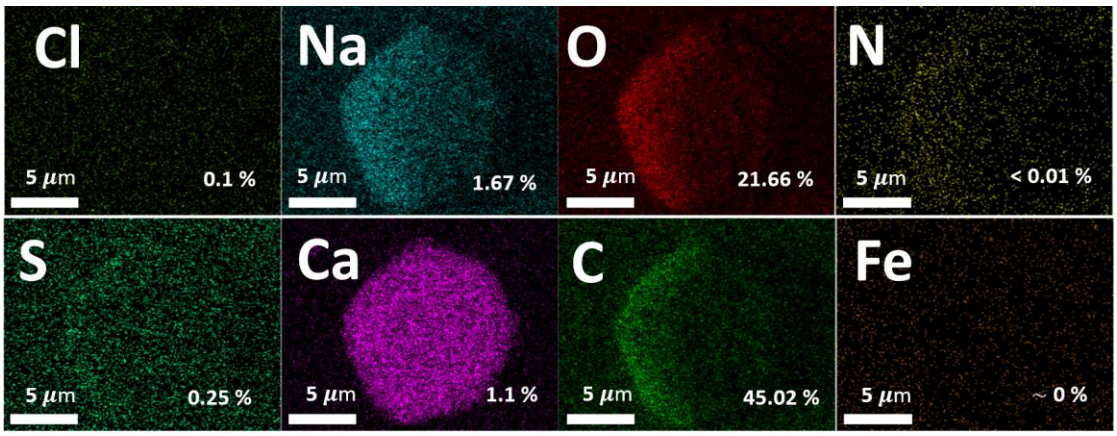

Figure 61. Map showing the chemical elements in a sacran aggregate shown in Figure 45 (c) by using the EDX-SEM technique.

Zhao et al. observed a strong anisotropy of SHG spots as a function of the incident polarization angle in a film made from ultrasonicated sacran aqueous solution. [107]

The SFG spectra

I obtained SFG spectra of dried sacran cast film made from 20-second ultrasonicated sacran solutions (12.2 kJ/ml of ultrasonic energy: Figure 62), as shown in Figure 63. Here I note that the cast films with no ultrasonic treatment show very weak SFG. I observed SFG spectra from two different regions of the sacran cast film; the first is the edge region and

the second is near the center. The edge region has a very high spotty SHG density (176.23 spots/mm^2). This region should have a high second-order nonlinearity and that is why I chose it for SFG measurement.

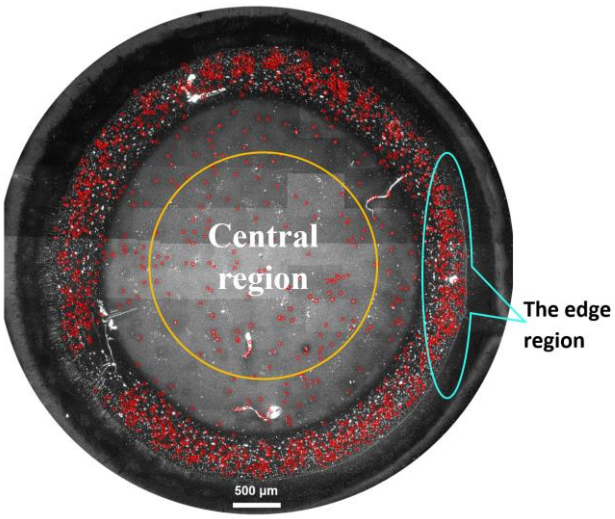

Figure 62. Schematic SHG image of a dried sacran cast film made from 20 seconds of ultrasonicated sacran solutions. The observed SHG spots are indicated by red dots. They are overlaid on a corresponding linear microscopic image.

Near the center, the density of SHG spots (24.5 spots/mm^2) was much less than in the edge region. Accordingly in Figure 63, I have a clear SFG spectrum for the edge region as in Figure 63 (a), while only a noise signal was detected near the center as in Figure 63 (c).

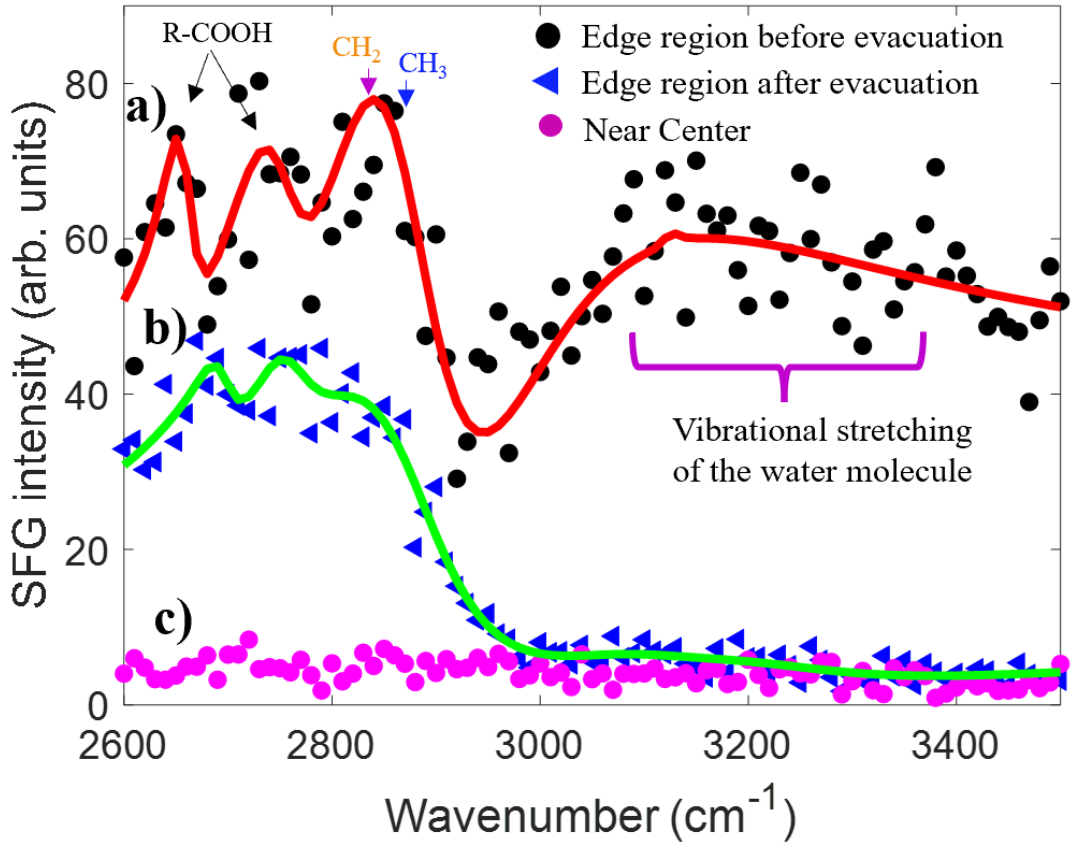

Figure 63. SFG spectra of a dried cast film made from 20 seconds of ultrasonicated sacran solution. (a) Black dots and the red curve are measured by SFG data and a fitting curve at the edge region of the cast film, respectively. (b) Blue triangles and the green curve are measured by SFG data and a fitting curve at the edge region of the cast film, respectively, after it was kept in a vacuum for 2 hours. (c) Purple dots are measured SFG intensity near the center of the cast film before the film was kept in a vacuum.

In Figure 63 (a) and (b), red and green fitting curves were drawn using the following equation [182]

$$S(\omega_{SFG}) \propto \left|\vec{\chi}^{(2)}_{NR} + \sum_n \frac{\vec{A}_n * e^{i\theta n}}{\omega_{IR} - \omega_n + i\Gamma_n}\right|^2 \quad (3\text{-}2)$$

Here, $\vec{\chi}^{(2)}_{NR}$, n, ω_n, ω_{IR}, $\vec{A}_n$, Γ_n are the non-resonant background in $\vec{\chi}^{(2)}$, the number of resonances, the frequency of the nth resonance, the frequency of infrared light, the amplitude, and the damping coefficient of the nth vibrational mode, respectively. In the red curve, the peak at around 2850 cm^{-1} is assigned as the symmetric stretching mode of CH_3 or CH_2 [122], [123], [183], and the peaks at 2650 and ~2750 cm^{-1} are assigned as the OH

stretching mode of the R – COOH group. [122] The broadband from 3100 to 3400 cm^{-1} is assigned as the vibrational OH stretching mode of water. This water band is not seen in the SFG spectra of the cast film kept in a vacuum for two hours (Figure 63 (b)). The water molecules would have been removed from the film in the vacuum.

Modeling of SHG-active sacran aggregates

I first summarize below the facts found out about sacran aggregates:

1) SHG-active sacran aggregates became visible in linear images after ultrasonication treatment of the source sacran aqueous solution, while it was not before the treatment.

2) The number of SHG spots increased after ultrasonication treatment up to 20 seconds (12.2 kJ/ml) and decreased for a longer ultrasonication time.

3) Hexagonal structures were observed in many of the SEM images of SHG active spots in the cast film made from 10 to 40-second ultrasonicated sacran aqueous solutions.

4) In the hexagonal structure Na, O, S, Ca, and C elements are uniformly distributed. The Ca to S ratio in the SHG-active region is four times higher than in the non-SHG-active region.

5) SFG spectra were observed for cast films made from sacran aqueous solutions ultrasonicated for 20 seconds.

6) CH_2 and CH_3-related peaks, R-COOH peaks, and a water peak were observed in the SFG spectra.

7) The water SFG peak disappeared after the cast film was evacuated.

On the other hand, I also list out the most important properties of SHG-active sacran aggregates from previous studies. [107], [108]

8) Most SHG signals have spotty shapes and have a very strong intensity near the center of the spots.

9) SHG images of the SHG-active sacran aggregates consist of concentric multilayer structures.

10) The SHG intensity spots have a strong incident polarization dependence but the 2PEF intensity does not.

11) When a sacran aqueous solution is put in an electrode cell and applied an electric voltage of 4.5 V and current until it dries, the SHG of sacran film becomes active near the negative electrode. [108]

12) All the sacran molecules take rod-like structures with a diameter of several micrometers and lengths larger than 200 μm above a threshold concentration and show a liquid crystal phase. [127], [125], [131], [184]

According to the above properties of sacran aggregates, I modeled the structure of an SHG-active self-assembled sacran in the following illustration.

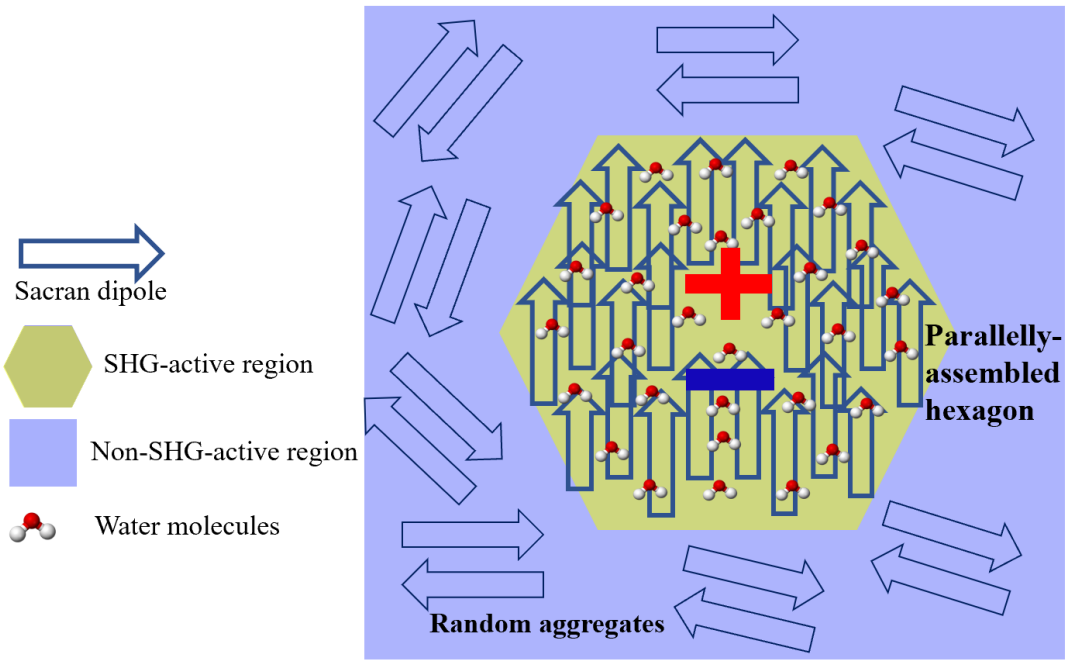

Figure 64. A plausible model of SHG-active sacran dipole aggregates.

Figure 64 is my tentative model structure of the SHG-active sacran aggregates. In the center of the SHG-active region, there might be positively charged sacran chains, because in property 11) above, the existence of positively charged sacran molecules is suggested. [107], [108] In Figure 64 I show only the charges and no sacran molecules. These positively charged sacran chains are a minority species, but they attract negatively charged sacran chains and form a central electric dipole. Other dipoles created around this central dipole are drawn as empty arrows. They are oriented in the same direction as each other and make a macroscopic dipole according to property 10) above. Outside the SHG spot, there are random dipoles created by sacran molecules. They make no macroscopic dipole. Within the SHG spot, we show water molecules. These water molecules are aligned in the same direction as each other so that the SFG of these water molecules are active according to properties 6) and 7) above. Property 10) suggests the one-direction oriented structure of negative sacran chains in the surrounding area of the electric dipole. Property 5) supports this view because such an anisotropy induces SFG activity of sacran molecules.

The nonzero SFG signal of water molecules mentioned in property 5) shows that the water molecules are oriented also. This may be caused by the orientation of the dipoles of the sacran molecules, and the fact endorses the assumption that the dipoles of the sacran molecules are oriented.

A uniform distribution of sodium and calcium cations in the sacran aggregates in property 4) suggests that the distribution of chemical elements is uniform in spite of the fact that the SHG intensity has a small and sharp core at the center. The mechanism of the correlation between SHG activity and Ca density is not understood.

In the SHG-inactive region, there might be a cancellation of electric dipoles of a pair of sacran molecules. This model is suggested according to the analogy with SHG and SFG

activities of amylose and amylopectin. If the reducing ends of sacran chains are up and down by 50% each, the SHG and SFG will be inactive.

The hexagonal structures seen in Figure 59 have not been reported so far. There is no information as to what the microscopic origin of this morphology is. However, it is interesting to guess the relation of this structure to properties 4) and 6). These last two properties clearly show that water is contained in the SHG active aggregates shown in Figure 63. In addition, as already suggested above, water is well aligned in the aggregates as illustrated in Figure 64. Hence the hexagonal shape might come from an ice crystalline morphology like that of snow. This guess may look strange because my samples are kept at room temperature. However, as pointed out by Shen *et al*., water is said to have a significant part of ice structure above the melting point, [182] and so that can lead to the observed hexagonal structure. If this is the case the SHG activity and the hexagonal structure of the SHG-active aggregates may be correlated because they are both induced by the dipole generation in the sacran cast film. An alternative origin of the hexagonal structure can be crystalline phases containing hexagonal spiral structures of saccharide chains such as those of amylopectin. [170]

3.3. Conclusions

In this chapter, SHG-active sacran aggregate structures in the cast film made from ultrasonicated sacran aqueous solution were analyzed by combining the SHG microscope, SEM/EDX-SEM, and SFG techniques. The SHG signals appeared most frequently in a spotty shape with high intensity near the center. According to SEM images, the SHG-active sacran aggregates can self-assemble into hexagonal structures of sizes several to 20 μm having extremely highly oriented and concentric multilayer-like structure units. The presence of countercations of sodium and calcium with a high uniform distribution was

confirmed as it is consistent with the efficient metal ion absorption properties. Calcium density is higher in the area showing SHG signals. SFG spectra were observed from the area with a higher number density of the SHG spots in the film. SFG spectra show peaks of vibrational modes of functional groups such as CH_3, CH_2, COOH, and broadband of O – H stretching mode of water. In our tentative model of the SHG-active sacran aggregate, the SHG phenomenon originates from the main electric dipole at the center created by positively and negatively charged sacran, with well-oriented dipoles induced by sacran chains in the surrounding area.

4. Chapter 4. General conclusions

In this thesis, I focus on studying sacran molecular structure based on nonlinear optical properties using SHG microscopy and the nonlinear response of SHG-active sacran aggregates when the sacran solution is applied to ultrasonication treatment, adsorbing metal ions (Er^{3+} and Nd^{3+}).

I have modeled the structure of SHG-active sacran aggregates at the microscale for the first time based on a combination of studies using SHG microscopy, SEM, EDX-SEM, and SFG spectroscopy. According to SEM images, the SHG-active sacran aggregates can self-assemble into the hexagonal structure of sizes several to 20 μm having extremely high oriented and concentric multilayer-like structure units. The presence of counter cations of sodium and calcium with a high uniform distribution was confirmed as it is consistent with the efficient metal ion absorption properties. Calcium density is higher in the area showing SHG signals.

SFG spectra of sacran cast film with densely SHG spot density are also observed for the first time. SFG spectra show peaks of vibrational modes of functional groups such as CH_3, CH_2, COOH, and broadband of O – H stretching mode of water. As the results of the above studies and previous works, I pointed out the characterization of the SHG-sacran aggregates:

- SHG-active sacran aggregates became visible in linear images after ultrasonication treatment of the source sacran aqueous solution, while it was not before the treatment.
- The number of SHG spots increased after ultrasonication treatment up to 20 seconds (12.2 kJ/ml) and decreased for a longer sonication time.
- Hexagonal structures were observed in many of the SEM images of SHG active spots in the cast film made from 10 to 40-second ultrasonicated sacran aqueous solutions.

- In the hexagonal structure Na, O, S, Ca, and C elements are uniformly distributed. The Ca to S ratio in the SHG-active region is four-times higher than in the non-SHG-active region.
- SFG spectra were observed for cast films made from sacran aqueous solutions ultrasonicated for 20 seconds.
- CH_2 and CH_3 related peaks, R-COOH peaks, and a water peak were observed in the SFG spectra.
- The water SFG peak disappeared after the cast film was evacuated.
- Most SHG signals have spotty shapes and have a very strong intensity near the center of the spots.
- SHG images of the SHG-active sacran aggregates consist of concentric multilayer structures.
- The SHG intensity spots have a strong incident polarization dependence but the 2PEF intensity does not.
- When a sacran aqueous solution is put in an electrode cell and applied at an electric voltage of 4.5 V and current until it dries, SHG of sacran film becomes active near the negative electrode.

The distribution of SHG signal and linear sacran spots in the cast films has been analyzed for the first time. SHG spot distribution changes from the uniform deposition (the original sacran solution and 10 seconds of ultrasonicated sacran solution) to the ring shape at the boundary of cast film (20 seconds of ultrasonicated sacran solutions) and finally transit to the center-bump structure when ultrasonication time is longer than 20 seconds. However, the distribution of linear sacran travels from uniform (the original sacran solution) to ring-like after 10 seconds of ultrasonication time and then separates into a

center bump with a spot size of fewer than 20 μm and a ring shape at the edge of the cast film with a spot size larger than 20 μm.

The behavior of SHG-active sacran aggregates and 0.5 wt% sacran solution adsorbing trivalent metal ions (Er^{3+} and Nd^{3}). The hypothesis is that metal ions connect with the sacran anions and take them away from the initial SHG-active sacran aggregates reducing the intensity weaker and might constitute new electric dipoles that give extremely weak SHG spots.

In summary, I point out some crucial results below:

(i) The SHG intensity of sacran molecules is proportional to the incident laser intensity square. Multiphoton excitation fluorescence experiments are also performed to ensure no three- and fourth-photon excitation fluorescence process.

(ii) The shape of SHG spots has a spotty-like structure with the highest intensity at the center of the spot. It reflects the structure of the local electric dipole with sacran cations at the center of the SHG spot and sacran anions oriented around.

(iii) The one-dimensional oriented structure of sacran chains in the SHG-active sacran aggregates: (1) the branch structure of sacran chains, (2) the Coulomb force from the electric dipole orient the sacran anions, (3) the ferroelectric liquid crystal phase might have existed inside the SHG-active sacran aggregates. By contrast, the 2PEF intensity shows the incident polarization independence.

(iv) SHG spot distribution changes from the uniform deposition (the original sacran solution and 10 seconds of ultrasonicated sacran solution) to the ring shape at the boundary of cast film (20 seconds of ultrasonicated sacran solutions) and finally transit to the center-bump structure when ultrasonication time is longer than 20 seconds.

(v) metal ions connect with the sacran anions and take them away from the initial SHG-active sacran aggregates reducing the intensity weaker and might constitute new electric dipoles that give extremely weak SHG spots.

(vi) SEM/EDX-SEM studies provided clear structures of the SHG-active sacran aggregates which have extremely oriented structures or multilayer-like structure units. Nano/microfibers sacran highly densely orient around a nucleus of the SHG-active sacran aggregate.

(vii) The presence of counter cations of sodium and calcium indicated the high metal ion adsorption properties.

(viii) The SFG spectra generated from the high SHG-spot density area indicated the high hydration of sacran molecules in the dried condition. This provides the potential SFG spectra technique to study sacran molecules.

(ix) The SHG-active sacran aggregate model provides a clearer structure of SHG aggregate and the origin of the SHG phenomenon.

(x) The hexagonal structure might be related to the ice structure of water molecules.

Publications

Thang Dinh Phan, Goro Mizutani, Yanrong Li, Kulisara Budpud, Kosuke Okeyoshi, Maiko Okajima, Tatsuo Kaneko, “Sum-Frequency Generation and Scanning Electron Microscope Studies on Second-Harmonic Generation Active Structures of Sacran Aggregates” e-J. Surf. Sci. Nanotechnol. 20, 98−106 (2022) | DOI: 10.1380/ejssnt.2022-016.

Presentations

1. Thang Dinh Phan, Yanrong Li, Kana Hatano, Goro Mizutani, Kosuke Okeyoshi, Maiko Okajima, Tatsuo Kaneko, “Excitation power dependence of SHG and 2PEF images of polysaccharide sacran cast films”, Physical Society of Japan 2020 Autumn Meeting (September), Japan.

2. Thang Dinh Phan, Goro Mizutani, Yanrong Li, Kulisara Budpud, Kosuke Okeyoshi, Maiko Okajima, Tatsuo Kaneko, “SFG and SEM studies on second-harmonic generation active structures of sacran aggregates”, the 13th International Symposium on Atomic Level Characterizations for New Materials and Devices ’21 held online (ALC ’21 Online), October 2021, Japan.

3. Thang Dinh Phan, Goro Mizutani, Yanrong Li, Kulisara Budpud, Kosuke Okeyoshi, Maiko Okajima, Tatsuo Kaneko, “Observation and modeling of second-harmonic generation active sacran aggregates”, International symposium of Excellent core for Sustainable material research 2021 & The 12th annual symposium for Suizenji-nori and Sacran 2021, Japan.

4. Thang Dinh Phan, Goro Mizutani, Yanrong Li, Pruetsakorn Saosamniang, Kosuke Okeyoshi, Maiko Okajima, Tatsuo Kaneko “Study of nonlinear optical property of

ultrasonicated sacran solutions using SHG microscopy", 14th International Symposium on Atomic Level Characterizations for New Materials and Devices '22 October 16 (Sun) – 21 (Fri), 2022 Bankoku Shinryokan, Okinawa JAPAN .

5. Thang Dinh Phan, Goro Mizutani, Kohei Tsujimura, Kulisara Budpud, Pruetsakorn Saosamniang, Kosuke Okeyoshi, Maiko Okajima, Tatsuo Kaneko1 "Change of distributions of second harmonic generation-active sacran particles of ultrasonicated sacran aqueous solutions", 2022 JAIST International Symposium of Nanomaterials and Devices Research Area, 14th (Wed.), December 2022.

5. Reference

[1] S. Grundmann *et al.*, "Zeptosecond birth time delay in molecular photoionization," *Science*, vol. 370, no. 6514, pp. 339–341, 2020, doi: 10.1126/science.abb9318.

[2] P. A. Franken, A. E. Hill, C. W. Peters, and G. Weinreich, "Generation of optical harmonics," *Physical Review Letters*, vol. 7, no. 4, pp. 118–119, 1961, doi: 10.1103/PhysRevLett.7.118.

[3] J. Kerr, " XL. A new relation between electricity and light: Dielectrified media birefringent ," *The London, Edinburgh, and Dublin Philosophical Magazine and Journal of Science*, vol. 50, no. 332, pp. 337–348, 1875, doi: 10.1080/14786447508641302.

[4] P. Weinberger, "John Kerr and his effects found in 1877 and 1878," *Philosophical Magazine Letters*, vol. 88, no. 12, pp. 897–907, 2008, doi: 10.1080/09500830802526604.

[5] J. Kerr, " LIV. A new relation between electricity and light: Dielectrified media birefringent (Second paper) ," *The London, Edinburgh, and Dublin Philosophical Magazine and Journal of Science*, vol. 50, no. 333, pp. 446–458, 1875, doi: 10.1080/14786447508641319.

[6] V. S. J. Wawilow *et al.*, "Die Beziehungen zwischen Fluoreszenz und Phosphoreszenz in festen und fliissigen Medien," vol. 2, pp. 920–936, 1925.

[7] J. A. Giordmaine, "Mixing of light beams in crystals," *Physical Review Letters*, vol. 8, no. 1, pp. 19–20, 1962, doi: 10.1103/PhysRevLett.8.19.

[8] R. Braunstein, "Nonlinear optical effects," *Physical Review*, vol. 125, no. 2, pp. 475–477, 1962, doi: 10.1103/PhysRev.125.475.

[9] J. A. Armstrong, N. Bloembergen, J. Ducuing, and P. S. Pershan, "Interactions between light waves in a nonlinear dielectric," *Physical Review*, vol. 127, no. 6, pp. 1918–1939, 1962, doi: 10.1103/PhysRev.127.1918.

[10] N. Bloembergen and P. S. Pershan, "Light waves at the boundary of nonlinear media," *Physical Review*, vol. 128, no. 2, pp. 606–622, 1962, doi: 10.1103/PhysRev.128.606.

[11] N. Bloembergen, "Nonlinear Optics- A Lecture Note And Reprint Volume Frontiers in Physics Series." W. A. Benjamin, Inc., New York, 1965.

[12] S. A. Akhmanov and R. V Khokhlov, "DEVELOPMENTS IN NON-LINEAR OPTICS," *Sov. Phys. Usp*, vol. 11, pp. 394–402, 1968, doi: 10.1070/PU1968v011n03ABEH003928.

[13] Y.R. Shen, *The principles of nonlinear optics*. New York: John Wiley & Sons, Inc., 1984.

[14] R. W. Boyd, *Nonlinear Optics*. New York: Academic Press, 2008.

[15] P. J. Mohr, B. N. Taylor, and D. B. Newell, "CODATA recommended values of the fundamental physical constants: 2006," *Reviews of Modern Physics*, vol. 80, no. 2, pp. 633–730, 2008, doi: 10.1103/RevModPhys.80.633.

[16] A. G. Lambert, P. B. Davies, and D. J. Neivandt, "Implementing the theory of sum frequency generation vibrational spectroscopy: A tutorial review," *Applied Spectroscopy*

Reviews, vol. 40, no. 2, pp. 103–145, 2005, doi: 10.1081/ASR-200038326.

[17] G. H. Wagnière and S. Woźniak, "Nonlinear optical properties," *Encyclopedia of Spectroscopy and Spectrometry*, pp. 375–387, 2017, doi: 10.1016/B978-0-12-803224-4.00232-6.

[18] M. Bass, P. A. Franken, and J. F. Ward, "Optical rectification," *Physical Review*, vol. 138, no. 2A, pp. 28–31, 1965, doi: https://doi.org/10.1103/PhysRevLett.9.446.

[19] J. A. Giordmaine and R. C. Miller, "Tunable coherent parametric oscillation in LiNbO3 optical frequencies," *Physical review letters*, vol. 14, no. 24, pp. 973–976, 1965, doi: https://doi.org/10.1103/PhysRevLett.14.973.

[20] R. W. Terhune, P. D. Maker, and C. M. Savage, "Optical harmonic generation in calcite," *Physical Review Letters*, vol. 8, no. 10, pp. 404–406, 1962, doi: https://doi.org/10.1103/PhysRevLett.8.404.

[21] A. P. Shkurinov, A. V. Dubrovskii, and N. I. Koroteecv, "Second Harmonic Generation in an Optically Acitve Liquid: Experiment Observation of a Fouth-Order Opitcal Nonlinearity Due to Molecular Chirality," *Physical Review Letters*, vol. 70, no. 8, 1993, doi: https://doi.org/10.1103/PhysRevLett.70.1085.

[22] J. Clerk-Maxwell, "Remarks on the mathematical classification of physical quantities," in *Proceedings of the London Mathematical Society*, 1869, vol. s1-3, no. 1, pp. 224–233, doi: 10.1112/plms/s1-3.1.224.

[23] D. J. Griffiths, *Introduction to Electrodynamics*. Pearson, Addison-Wesley, 2013.

[24] R. P. Feynman, R. Leighton, and M. Sands, *The Feynman Lectures on Physics 2 - Electromagnatism*. New York: Addison-Wesley, 2010.

[25] W. K. H. Panofsky and M. Phillips, *Classical electricity and magnetism*-. Addison-Wesley Pub. Co, 1962.

[26] Z. Y. Zhao, S. Hameau, M. Voos, and J. Tignon, "THz generation by optical rectification and competition with other nonlinear processes," *17th International Symposium on Space Terahertz Technology 2006, ISSTT 2006*, pp. 259–262, 2006.

[27] F. Kadlec, P. Kužel, and J.-L. Coutaz, "Study of terahertz radiation generated by optical rectification on thin gold films," *Optics Letters*, vol. 30, no. 11, pp. 1402–1404, 2005, doi: https://doi.org/10.1364/OL.30.001402.

[28] G. Ramakrishnan, N. Kumar, P. C. M. Planken, D. Tanaka, and K. Kajikawa, "Surface plasmon-enhanced terahertz emission from a hemicyanine self-assembled monolayer," *Optics Express*, vol. 20, no. 4, p. 4067, 2012, doi: 10.1364/OE.20.004067.

[29] K. J. Kaltenecker *et al.*, "Gouy phase shift of a tightly focused, radially polarized beam," *Optica*, vol. 3, no. 1, p. 35, 2016, doi: 10.1364/optica.3.000035.

[30] P. Koleják, K. Postava, M. Mičica, P. Kužel, F. Kadlec, and J. Pištora, "Experimental Gouy phase shift compensation in Terahertz time-domain spectroscopy," *Photonics and*

Nanostructures - Fundamentals and Applications, vol. 31, no. October 2017, pp. 129–133, 2018, doi: 10.1016/j.photonics.2018.06.011.

[31] S. Feng and H. G. Winful, "Physical origin of the Gouy phase shift," *Optics Letters*, vol. 26, no. 8, p. 485, 2001, doi: 10.1364/ol.26.000485.

[32] N. M. Kroll, "Parametric Amplification in Spatially Extended Media and Application to the Design of Tuneable Oscillators at Optical Frequencies," *Proceedings of the IEEE*, vol. 127, no. 4, pp. 1207–1211, 1962, doi: 10.1109/PROC.1963.1665.

[33] L. E. Myers and W. R. Bosenberg, "Periodically poled lithium niobate and quasi-phase-matched optical parametric oscillators," *IEEE Journal of Quantum Electronics*, vol. 33, no. 10, pp. 1663–1672, 1997, doi: 10.1109/3.631262.

[34] Y. Du *et al.*, "Parametric and cascaded parametric interactions in a quasiperiodic optical superlattice," *Applied Physics Letters*, vol. 81, no. 9, pp. 1573–1575, 2002, doi: 10.1063/1.1502007.

[35] Q. Chen and W. P. Risk, "Periodic poling of KTiOPO4using an applied electric field," *Electronics Letters*, vol. 30, no. 18, pp. 1516–1517, 1994, doi: 10.1049/el:19941019.

[36] S. Kurimura, I. Shimoya, and Y. UESU, "Domain Inversion by an Electron-Beam-Induced Electric Field in MgO : LiNbO 3 , LiNbO 3 and LiTaO 3," *Jpn. J. Appl. Phys*, vol. 35, pp. 31–33, 1996.

[37] J. F. Ward and P. A. Franken, "Structure of nonlinear optical phenomena in potassium dihydrogen phosphate," *Physical Review*, vol. 133, no. 1A, 1964, doi: 10.1103/PhysRev.133.A183.

[38] J. Zhang, J. Y. Huang, H. Wang, K. S. Wong, and G. K. Wong, "Second-harmonic generation from regeneratively amplified femtosecond laser pulses in BBO and LBO crystals," *Journal of the Optical Society of America B*, vol. 15, no. 1, p. 200, 1998, doi: 10.1364/josab.15.000200.

[39] R. C. Eckardt, H. Masuda, Y. X. Fan, and R. L. Byer, "Absolute and Relative Nonlinear Optical Coefficients of KDP, KD*P, BaB2O4, LiIO3, MgO:LiNbO3, and KTP Measured by Phase-Matched Second-Harmonic Generation," *IEEE Journal of Quantum Electronics*, vol. 26, no. 5, pp. 922–933, 1990, doi: 10.1109/3.55534.

[40] F. X. Wang, F. J. Rodríguez, W. M. Albers, R. Ahorinta, J. E. Sipe, and M. Kauranen, "Surface and bulk contributions to the second-order nonlinear optical response of a gold film," *Physical Review B - Condensed Matter and Materials Physics*, vol. 80, no. 23, pp. 4–7, 2009, doi: 10.1103/PhysRevB.80.233402.

[41] S. Deckoff-Jones *et al.*, "Observing the interplay between surface and bulk optical nonlinearities in thin van der Waals crystals," *Scientific Reports*, vol. 6, no. March, pp. 1–7, 2016, doi: 10.1038/srep22620.

[42] J. E. Sipe, "New Green-function formalism for surface optics," *Journal of the Optical*

Society of America B, vol. 4, no. 4, p. 481, 1987, doi: 10.1364/josab.4.000481.

[43] J. Renger, R. Quidant, and L. Novotny, "Enhanced nonlinear response from metal surfaces," *Optics Express*, vol. 19, no. 3, p. 1777, 2011, doi: 10.1364/oe.19.001777.

[44] R. M. Corn and D. A. Higgins, "Optical Second Harmonic Generation as a Probe of Surface Chemistry," *Chemical Reviews*, vol. 94, no. 1, pp. 107–125, 1994, doi: 10.1021/cr00025a004.

[45] F. Brown and M. Matsuoka, "Effect of Adsorbed Surface Layers on Second-Harmonic Light from Silver," *Physical Review*, vol. 185, no. 3, pp. 985–987, 1969, doi: 10.1103/PhysRev.185.985.

[46] J. Rudnick and E. A. Stern, "Second-harmonic radiation from metal surfaces," *Physical Review B*, vol. 4, no. 12, pp. 4274–4290, 1971, doi: 10.1103/PhysRevB.4.4274.

[47] Y.R. Shen, "Optical Second Harmonic Generation At Interfaces," *Annual Review of Physical Chemistry*, vol. 40, no. 1, pp. 327–350, 1989, doi: 10.1146/annurev.physchem.40.1.327.

[48] G. S. He, *Nonlinear Optics and Photonics*. Oxford University Press, USA, 2015.

[49] K. Kreher, *Modern Nonlinear Optics*, vol. 213, no. 1. 1999.

[50] R. L. Sutherland, *Handbook of Nonlinear Optics*, vol. 36, no. 3. Marcel Dekker, Inc, 2003.

[51] P. M. Rentzepis, J. A. Giordmaine, and K. W. Wecht, "Coherent optial mixing in optical active liquids," *Physical review letters*, vol. 16, no. 18, pp. 49–58, 1966, doi: 10.1103/PhysRevLett.16.792.

[52] T. Verbiest, M. Kauranen, Y. Van Rompaey, and A. Persoons, "Optical Activity of Anisotropic Achiral Surfaces," *Physical Review Letters*, vol. 77, no. 8, pp. 1456–1459, 1996, doi: 10.1103/PhysRevLett.77.1456.

[53] H. Sano and G. Mizutani, "Ab initio calculation of surface nonlinear optical response," *e-Journal of Surface Science and Nanotechnology*, vol. 1, no. July, pp. 57–66, 2003, doi: 10.1380/ejssnt.2003.57.

[54] N. Bloembergen, "Surface nonlinear optics: A historical overview," *Applied Physics B: Lasers and Optics*, vol. 68, no. 2–3, pp. 289–293, 1999, doi: 10.1007/s003400050621.

[55] S. S. Jha, "Theory of optical harmonic generation at a metal surface," *Physical Review*, vol. 140, no. 6A, 1965, doi: 10.1103/PhysRev.140.A2020.

[56] S. Jha, Sudhanshu, "Second-Order Optical Processes and Harmonic Fields in Solids," *Physical Review*, vol. 145, no. 1962, p. 500, 1966, doi: 10.1103/PhysRev.145.500.

[57] Y. R. Shen, *Fundamentals of Sum-Frequency Spectroscopy*. Cambridge, 2016.

[58] J. D. Byers, H. I. Yee, T. Petralli-Mallow, and J. M. Hicks, "Second-harmonic generation circular-dichroism spectroscopy from chiral monolayers," *Physical Review B*, vol. 49, no. 20, pp. 14643–14647, 1994, doi: 10.1103/PhysRevB.49.14643.

[59] J. M. Hicks, T. Petralli-Mallow, and J. D. Byers, "Consequences of chirality in second-order

non-linear spectroscopy at surfaces," *Faraday Discussions*, vol. 99, no. 1, pp. 341–357, 1994, doi: 10.1039/FD9949900341.

[60] W. Kaiser and C. G. B. Garrett, "Two-photon excitation in CaF2: Eu2+," *Physical Review Letters*, vol. 7, no. 6, pp. 229–231, 1961, doi: 10.1103/PhysRevLett.7.229.

[61] W. Denk, J. H. Strickler, and W. W. Webb, "Two-photon laser scanning fluorescence microscopy," *Science*, vol. 248, no. 4951, pp. 73–76, 1990, doi: 10.1126/science.2321027.

[62] Y. Barad, H. Eisenberg, M. Horowitz, and Y. Silberberg, "Nonlinear scanning laser microscopy by third harmonic generation," *Applied Physics Letters*, vol. 70, no. 8, pp. 922–924, 1997, doi: 10.1063/1.118442.

[63] J. M. Bueno, F. J. Avila, and P. Artal, "Second Harmonic Generation Microscopy: A Tool for Quantitative Analysis of Tissues," *Intech*, p. 13, 2016, doi: http://dx.doi.org/10.5772/63493.

[64] J.-X. Cheng, L. D. Book, and X. S. Xie, "Polarization Coherent anti-stokes Raman scattering microscopy," *Optics Letters*, vol. 26, no. 17, pp. 83–86, 2001, doi: 10.1364/ol.26.001341.

[65] C. L. Evans and X. S. Xie, "Coherent anti-Stokes Raman scattering microscopy: Chemical imaging for biology and medicine," *Annual Review of Analytical Chemistry*, vol. 1, no. 1, pp. 883–909, 2008, doi: 10.1146/annurev.anchem.1.031207.112754.

[66] I. Freund and M. Deutsch, "Second-harmonic microscopy of biological tissue," *Optics Letters*, vol. 11, no. 2, p. 94, 1986, doi: 10.1364/ol.11.000094.

[67] R. Gauderon, P. B. Lukins, and C. J. R. Sheppard, "Optimization of second-harmonic generation microscopy," *Micron*, vol. 32, no. 7, pp. 691–700, 2001, doi: 10.1016/S0968-4328(00)00066-4.

[68] K. Ahi, "Mathematical modeling of thz point spread function and simulation of THz imaging systems," *IEEE Transactions on Terahertz Science and Technology*, vol. 7, no. 6, pp. 747–754, 2017, doi: 10.1109/TTHZ.2017.2750690.

[69] J. D. Bhawalkar *et al.*, "Two-photon laser scanning fluorescence microscopy - From a fluorophore and specimen perspective," *Bioimaging*, vol. 4, no. 3, pp. 168–178, 1996, doi: 10.1002/1361-6374(199609)4:3<168::aid-bio7>3.3.co;2-%23.

[70] Q. Li, S. S. H. Wu, and K. C. Chou, "Subdiffraction-limit two-photon fluorescence microscopy for GFP-tagged cell imaging," *Biophysical Journal*, vol. 97, no. 12, pp. 3224–3228, 2009, doi: 10.1016/j.bpj.2009.09.038.

[71] D. M. Nikolenko *et al.*, "Measurement of the Tensor Analyzing Powers T20 and T21 in Elastic Electron-Deuteron Scattering," *Physical Review Letters*, vol. 90, no. 7, p. 4, 2003, doi: 10.1103/PhysRevLett.90.072501.

[72] F. Helmchen and W. Denk, "Deep tissue two-photon microscopy," *Nature Methods*, vol. 2, no. 12, pp. 932–940, 2005, doi: 10.1038/nmeth818.

[73] K. Svoboda and R. Yasuda, “Principles of Two-Photon Excitation Microscopy and Its Applications to Neuroscience,” *Neuron*, vol. 50, no. 6, pp. 823–839, 2006, doi: 10.1016/j.neuron.2006.05.019.

[74] R. K. P. Benninger, W. J. Ashby, E. A. Ring, and D. W. Piston, “A single-photon counting detector for increased sensitivity in two-photon laser scanning microscopy,” vol. 33, no. 24, pp. 2895–2897, 2009, doi: 10.1364/ol.33.002895.

[75] V. D. Ching-Roa, E. M. Olson, S. F. Ibrahim, R. Torres, and M. G. Giacomelli, “Ultrahigh-speed point scanning two-photon microscopy using high dynamic range silicon photomultipliers,” *Scientific Reports*, vol. 11, no. 1, pp. 1–12, 2021, doi: 10.1038/s41598-021-84522-0.

[76] M. N. Modi, K. Daie, G. C. Turner, and K. Podgorski, “Two-photon imaging with silicon photomultipliers,” *Optics Express*, vol. 27, no. 24, p. 35830, 2019, doi: 10.1364/oe.27.035830.

[77] K. Taira, T. Hashimoto, and H. Yokoyama, “Two-photon fluorescence imaging with a pulse source based on a 980-nm gain-switched laser diode,” *Optics Express*, vol. 15, no. 5, p. 2454, 2007, doi: 10.1364/oe.15.002454.

[78] J. G.- Mayer, “Uber elementarakte mit zwei quantensprungen von,” 1931, doi: 10.1002/andp.19314010303.

[79] A. Jabłoństski, “Efficiency of anti-stokes fluorescence in dyes,” *Nature*, vol. 131, no. 3319, pp. 839–840, 1933, doi: 10.1038/131839b0.

[80] M. Y. Berezin and S. Achilefu, “Fluorescence lifetime measurements and biological imaging,” *Chemical Reviews*, vol. 110, no. 5, pp. 2641–2684, 2010, doi: 10.1021/cr900343z.

[81] M. Oheim, D. J. Michael, M. Geisbauer, D. Madsen, and R. H. Chow, “Principles of two-photon excitation fluorescence microscopy and other nonlinear imaging approaches,” *Advanced Drug Delivery Reviews*, vol. 58, no. 7, pp. 788–808, 2006, doi: 10.1016/j.addr.2006.07.005.

[82] A. Diaspro and G. Chirico, “Two-photon excitation microscopy,” *Advances in Imaging and Electron Physics*, vol. 126, pp. 399–429, 2003, doi: 10.1016/S1076-5670(03)80016-2.

[83] W. Denk, J. H. Strickler, and W. W. Webb, “Two-photon laser scanning fluorescence microscopy,” *Science*, vol. 248, pp. 73–76, 1990, doi: 10.1126/science.2321027.

[84] B. A. MacVicar and S. A. Mulligan, “Two-Photon Fluorescence Microscopy: Basic Principles, Advantages and Risks,” *Modern Research and Educational Topics in Microscopy*, no. January 2007, pp. 881–889, 2007.

[85] D. Kobat, N. G. Horton, and C. Xu, “In vivo two-photon microscopy to 1.6-mm depth in mouse cortex,” *Journal of Biomedical Optics*, vol. 16, no. 10, p. 1, 2011, doi: 10.1117/1.3646209.

[86] P. J. Campagnola and L. M. Loew, “Second-harmonic imaging microscopy for visualizing biomolecular arrays in cells, tissues and organisms,” *Nature Biotechnology*, vol. 21, no. 11, pp. 1356–1360, 2003, doi: 10.1038/nbt894.

[87] D. S. Chemla and J. Zyss, *Nonlinear Optical Properties of Organic Molecules and Crystals*, vol. 1. Academic Press, Inc., 1987.

[88] D. S. CHEMLA and J. ZYSS, *Nonlinear optical properties of organic molecules and crystals*, vol. 2. Academic Press, Inc., 1987.

[89] B. R. Masters and P. T. C. So, *Biomedical nonlinear optical microscopy*. Oxford University Press, Inc., 2008.

[90] S. W. Chu *et al.*, “Studies of $\chi(2)/\chi(3)$ tensors in submicron-scaled bio-tissues by polarization harmonics optical microscopy,” *Biophysical Journal*, vol. 86, no. 6, pp. 3914–3922, 2004, doi: 10.1529/biophysj.103.034595.

[91] R. LaComb, O. Nadiarnykh, S. S. Townsend, and P. J. Campagnola, “Phase matching considerations in second harmonic generation from tissues: Effects on emission directionality, conversion efficiency and observed morphology,” *Optics Communications*, vol. 281, no. 7, pp. 1823–1832, 2008, doi: 10.1016/j.optcom.2007.10.040.

[92] S. V. Plotnikov, A. C. Millard, P. J. Campagnola, and W. A. Mohler, “Characterization of the myosin-based source for second-harmonic generation from muscle sarcomeres,” *Biophysical Journal*, vol. 90, no. 2, pp. 693–703, 2006, doi: 10.1529/biophysj.105.071555.

[93] R. Gauderon, P. B. Lukins, and C. J. R. Sheppard, “Three-dimensional second-harmonic generation imaging with femtosecond laser pulses,” *Optics Letters*, vol. 23, no. 15, p. 1209, 1998, doi: 10.1364/ol.23.001209.

[94] D. Yelin and Y. Silberberg, “Laser scanning third-harmonic-generation microscopy in biology,” vol. 5, no. 8, pp. 169–175, 1999, doi: https://doi.org/10.1364/OE.5.000169.

[95] C. V. Raman, “A new radiation,” *Proceedings of the Indian Academy of Sciences - Section A*, vol. 37, no. 3, pp. 333–341, 1953, doi: 10.1007/BF03052651.

[96] R. Loudon, *The Quantum Theory of Light*. Oxford University Press, 2000.

[97] C. M. Penney, L. M. Goldman, and M. Lapp, “Raman Scattering Cross Sections,” *Nature Physical Science*, vol. 235, pp. 110–112, 1972, doi: 10.1038/physci235110b0.

[98] T. Chernenko, C. Matthäus, L. Milane, L. Quintero, M. Amiji, and M. Diem, “Label-free raman spectral imaging of intracellular delivery and degradation of polymeric nanoparticle systems,” *ACS Nano*, vol. 3, no. 11, pp. 3552–3559, 2009, doi: 10.1021/nn9010973.

[99] G. Romero *et al.*, “Surface engineered poly(lactide-co-glycolide) nanoparticles for intracellular delivery: Uptake and cytotoxicity - A confocal Raman microscopic study,” *Biomacromolecules*, vol. 11, no. 11, pp. 2993–2999, 2010, doi: 10.1021/bm1007822.

[100] L. Wei, Y. Yu, Y. Shen, M. C. Wang, and W. Min, “Vibrational imaging of newly synthesized proteins in live cells by stimulated Raman scattering microscopy,” *Proceedings*

of the National Academy of Sciences of the United States of America, vol. 110, no. 28, pp. 11226–11231, 2013, doi: 10.1073/pnas.1303768110.

[101] Y. Shen, *Towards fast coherent anti-Stokes Raman scattering microscopy*. Texas A & M University, 2018.

[102] J. Cheng and X. S. Xie, "Coherent anti-Stokes Raman scattering microscopy: Instrumentation, theory, and applications," *J Phys Chem B*, vol. 108, pp. 827–840, 2004, doi: https://doi.org/10.1021/jp035693v.

[103] E. Capitaine *et al.*, "Coherent anti-Stokes Raman scattering under electric field stimulation," *Physical Review B*, vol. 94, no. 245136, pp. 1–6, 2016, doi: 10.1103/PhysRevB.94.245136.

[104] A. Paddubskaya, A. Dementjev, A. Devižis, R. Karpicz, S. Maksimenko, and G. Valušis, "Coherent anti-Stokes Raman scattering as an effective tool for visualization of single-wall carbon nanotubes," *Optics Express*, vol. 26, no. 8, p. 10527, 2018, doi: 10.1364/oe.26.010527.

[105] M. Okajima-Kaneko, M. Ono, K. Kabata, and T. Kaneko, "Extraction of novel sulfated polysaccharides from Aphanothece sacrum (Sur.) Okada, and its spectroscopic characterization," *Pure and Applied Chemistry*, vol. 79, no. 11, pp. 2039–2046, 2007, doi: 10.1351/pac200779112039.

[106] K. Hori, T. Ueno-Mohri, and T. Okita, "Absorption of color additives and settling volume in water of blue-green alga, ishikurage (Nostoc commune)," *Plant Foods for Human Nutrition*, vol. 42, no. 1, pp. 31–36, 1992, doi: 10.1007/BF02196070.

[107] Y. Zhao *et al.*, "Optical second-harmonic images of sacran megamolecule aggregates," *Journal of the Optical Society of America A*, vol. 34, no. 2, pp. 146–152, 2017, doi: 10.1364/JOSAA.34.000146.

[108] Y. Zhao *et al.*, "Electric Field Effect on Optical Second-harmonic Generation of Amphoteric Megamolecule Aggregates," *Journal of the Physical Society of Japan*, vol. 86, 2017, doi: 10.7566/JPSJ.86.124401.

[109] T. D. Phan *et al.*, "Sum-Frequency Generation and Scanning Electron Microscope Studies on Second-Harmonic Generation Active Structures of Sacran Aggregates," *e-Journal of Surface Science and Nanotechnology*, vol. 20, no. 2, pp. 98–106, 2022, doi: 10.1380/ejssnt.2022-016.

[110] L. E. Puluhulawa, I. M. Joni, A. F. A. Mohammed, H. Arima, and N. Wathoni, "The use of megamolecular polysaccharide Sacran in food and biomedical applications," *Molecules*, vol. 26, no. 11, pp. 1–15, 2021, doi: 10.3390/molecules26113362.

[111] F. Watanabe, E. Miyamoto, T. Fujita, Y. Tanioka, and Y. Nakano, "Characterization of a corrinoid compound in the edible (blue-green) alga, Suizenji-nori," *Bioscience, Biotechnology and Biochemistry*, vol. 70, no. 12, pp. 3066–3068, 2006, doi: 10.1271/bbb.60395.

[112] K. Igata *et al.*, “Cationic Polymer Brush/Giant Polysaccharide Sacran Assembly: Structure and Lubricity,” *Langmuir*, vol. 36, no. 23, pp. 6494–6501, 2020, doi: 10.1021/acs.langmuir.0c00854.

[113] M. K. Okajima *et al.*, “Supergiant ampholytic sugar chains with imbalanced charge ratio form saline ultra-absorbent hydrogels,” *Macromolecules*, vol. 41, no. 12, pp. 4061–4064, 2008, doi: 10.1021/ma800307w.

[114] T. Mitsumata, T. Miura, N. Takahashi, M. Kawai, M. K. Okajima, and T. Kaneko, “Ionic state and chain conformation for aqueous solutions of supergiant cyanobacterial polysaccharide,” *Physical Review E - Statistical, Nonlinear, and Soft Matter Physics*, vol. 87, no. 4, pp. 1–9, 2013, doi: 10.1103/PhysRevE.87.042607.

[115] M. K. Cowman, T. A. Schmidt, P. Raghavan, and A. Stecco, “Viscoelastic Properties of Hyaluronan in Physiological Conditions,” *F1000Research*, vol. 4, no. May, pp. 1–13, 2015, doi: 10.12688/f1000research.6885.1.

[116] G. Holzwarth, “Molecular weight of xanthan polysaccharide,” *Carbohydrate Research*, vol. 66, no. 1, pp. 173–186, 1978, doi: 10.1016/S0008-6215(00)83250-4.

[117] L. Zhong, M. Oostrom, M. J. Truex, V. R. Vermeul, and J. E. Szecsody, “Rheological behavior of xanthan gum solution related to shear thinning fluid delivery for subsurface remediation,” *Journal of Hazardous Materials*, vol. 244–245, pp. 160–170, 2013, doi: 10.1016/j.jhazmat.2012.11.028.

[118] T. Dürig and K. Karan, *Binders in wet granulation*. 2018.

[119] P. Khuman, W. B. K. Singh, S. D. Devi, and H. Naorem, “Viscosityerature behavior of hydroxypropyl cellulose solution in presence of an electrolyte or a surfactant: A convenient method to determine the cloud point of polymer solutions,” *Journal of Macromolecular Science, Part A: Pure and Applied Chemistry*, vol. 51, no. 11, pp. 924–930, 2014, doi: 10.1080/10601325.2014.953377.

[120] M. A. Rousselle, “Determining the Molecular Weight Distribution of Cotton Cellulose: A New GPC Solvent,” *Textile Research Journal*, vol. 72, no. 2, pp. 131–134, 2002, doi: 10.1177/004051750207200207.

[121] J. Desbrieres, “Viscosity of semiflexible chitosan solutions: Influence of concentration, temperature, and role of intermolecular interactions,” *Biomacromolecules*, vol. 3, no. 2, pp. 342–349, 2002, doi: 10.1021/bm010151+.

[122] P. J. Lakin, *IR and Raman Spectroscopy: Principles and Spectral Interpretation*. 2011.

[123] B. H. Stuart, *Infrared Spectroscopy: Fundamentals and Applications*. 2004.

[124] M. K. Okajima, D. Kaneko, T. Mitsumata, T. Kaneko, and J. Watanabe, “Cyanobacteria that produce megamolecules with efficient self-orientations,” *Macromolecules*, vol. 42, no. 8, pp. 3057–3062, 2009, doi: 10.1021/ma802829x.

[125] K. Okeyoshi, M. K. Okajima, and T. Kaneko, “The cyanobacterial polysaccharide sacran:

characteristics, structures, and preparation of LC gels," *Polymer Journal*, vol. 53, no. 1, pp. 81–91, 2021, doi: 10.1038/s41428-020-00426-2.

[126] K. Shikinaka, K. Okeyoshi, H. Masunaga, M. K. Okajima, and T. Kaneko, "Solution structure of cyanobacterial polysaccharide, sacran," *Polymer (United Kingdom)*, vol. 99, pp. 767–770, 2016, doi: 10.1016/j.polymer.2016.08.003.

[127] K. Budpud, K. Okeyoshi, M. K. Okajima, and T. Kaneko, "Vapor-Sensitive Materials from Polysaccharide Fibers with Self-Assembling Twisted Microstructures," *Small*, vol. 16, no. 29, pp. 1–7, 2020, doi: 10.1002/smll.202001993.

[128] K. Budpud, K. Okeyoshi, S. Kobayashi, M. K. Okajima, and T. Kaneko, "Super-Moisturizing Materials from Morphological Deformation of Suprapolysaccharides," *Macromolecular Rapid Communications*, vol. 43, no. 11, pp. 1–8, 2022, doi: 10.1002/marc.202200163.

[129] K. Budpud, K. Okeyoshi, M. K. Okajima, and T. Kaneko, "Cyanobacterial supra-polysaccharide: Self-similar hierarchy, diverse morphology, and application prospects of sacran fibers," *Biopolymers*, vol. 113, no. 9, pp. 1–11, 2022, doi: 10.1002/bip.23522.

[130] K. Okeyoshi *et al.*, "Drying-Induced Self-Similar Assembly of Megamolecular Polysaccharides through Nano and Submicron Layering," *Langmuir*, vol. 33, no. 20, pp. 4954–4959, 2017, doi: 10.1021/acs.langmuir.7b00107.

[131] K. Okeyoshi, M. K. Okajima, and T. Kaneko, "Milliscale Self-Integration of Megamolecule Biopolymers on a Drying Gas-Aqueous Liquid Crystalline Interface," *Biomacromolecules*, vol. 17, no. 6, pp. 2096–2103, 2016, doi: 10.1021/acs.biomac.6b00302.

[132] K. Okeyoshi, M. K. Okajima, and T. Kaneko, "Emergence of polysaccharide membrane walls through macro-space partitioning via interfacial instability," *Scientific Reports*, vol. 7, no. 1, pp. 1–8, 2017, doi: 10.1038/s41598-017-05883-z.

[133] K. Okeyoshi, T. Shinhama, K. Budpud, G. Joshi, M. K. Okajima, and T. Kaneko, "Micelle-Mediated Self-Assembly of Microfibers Bridging Millimeter-Scale Gap to Form Three-Dimensional-Ordered Polysaccharide Membranes," *Langmuir*, vol. 34, no. 46, pp. 13965–13970, 2018, doi: 10.1021/acs.langmuir.8b03116.

[134] Q. T. Le Nguyen, M. Okajima, T. Mitsumata, K. Kan, H. T. Tran, and T. Kaneko, "Trivalent metal-mediated gelation of novel supergiant sulfated polysaccharides extracted from Aphanothece stagnina," *Colloid and Polymer Science*, vol. 290, no. 2, pp. 163–172, 2012, doi: 10.1007/s00396-011-2528-3.

[135] M. K. Okajima *et al.*, "Anionic complexes of MWCNT with supergiant cyanobacterial polyanions," *Biopolymers*, vol. 99, no. 1, pp. 1–9, 2013, doi: 10.1002/bip.22129.

[136] M. K. Okajima, Q. T. Le Nguyen, M. Nakamura, T. Ogawa, H. Kurata, and T. Kaneko, "Double-metal complexation of heterogels containing cyanobacterial polysaccharides," *Journal of Applied Polymer Science*, vol. 128, no. 1, pp. 676–683, 2013, doi:

10.1002/app.38261.

[137] M. K. Okajima, S. Miyazato, and T. Kaneko, “Cyanobacterial megamolecule sacran efficiently forms LC gels with very heavy metal ions,” *Langmuir*, vol. 25, no. 15, pp. 8526–8531, 2009, doi: 10.1021/la8036956.

[138] M. K. Okajima, M. Nakamura, T. Mitsumata, and T. Kaneko, “Cyanobacterial Polysaccharide Gels with Efficient Rare-Earth-Metal Sorption,” *Biomacromolecules*, vol. 11, no. 7, pp. 1773–1778, 2010, doi: 10.1021/bm100231q.

[139] M. K. Okajima *et al.*, “Photoshrinkage in polysaccharide gels with trivalent metal ions.,” *Biomacromolecules*, vol. 13, no. 12, pp. 4158–4163, 2012, doi: 10.1021/bm301440e.

[140] M. K. Okajima *et al.*, “Gelation behavior by the lanthanoid adsorption of the cyanobacterial extracellular polysaccharide,” *Biomacromolecules*, vol. 11, no. 11, pp. 3172–3177, 2010, doi: 10.1021/bm101012u.

[141] N. Wathoni, K. Motoyama, T. Higashi, M. Okajima, T. Kaneko, and H. Arima, “Physically crosslinked-sacran hydrogel films for wound dressing application,” *International Journal of Biological Macromolecules*, vol. 89, pp. 465–470, 2016, doi: 10.1016/j.ijbiomac.2016.05.006.

[142] K. Motoyama *et al.*, “Anti-inflammatory effects of novel polysaccharide sacran extracted from cyanobacterium Aphanothece sacrum in various inflammatory animal models,” *Biological and Pharmaceutical Bulletin*, vol. 39, no. 7, pp. 1172–1178, 2016, doi: 10.1248/bpb.b16-00208.

[143] K. Motoyama *et al.*, “Potential Use of a Megamolecular Polysaccharide Sacran as a Hydrogel-Based Sustained Release System,” *Chemical and Pharmaceutical Bulletin*, vol. 62, no. 7, pp. 636–641, 2014, doi: 10.1248/cpb.c14-00053.

[144] K. Motoyama, Y. Tanida, A. Sakai, T. Higashi, S. Kaneko, and H. Arima, “Anti-allergic effects of novel sulfated polysaccharide sacran on mouse model of 2,4-Dinitro-1-fluorobenzene-induced atopic dermatitis,” *International Journal of Biological Macromolecules*, vol. 108, pp. 112–118, 2018, doi: 10.1016/j.ijbiomac.2017.11.155.

[145] N. R. Ngatu *et al.*, “Anti-allergic and Profilaggrin (ProFLG)-mRNA expression modulatory effects of sacran,” *International Journal of Biological Macromolecules*, vol. 105, pp. 1532–1538, 2017, doi: 10.1016/j.ijbiomac.2017.05.049.

[146] N. R. Ngatu, R. Hirota, M. K. Okajima, T. Kaneko, K. F. Malonga, and N. Suganuma, “Sacran , a natural skin barrier enhancer , improves atopic and contact eczema : Case report,” *Annals of Phytomedicine*, vol. 4, no. 1, pp. 111–113, 2015.

[147] N. R. Ngatu *et al.*, “Anti-inflammatory effects of sacran, a novel polysaccharide from Aphanothece sacrum, on 2,4,6-trinitrochlorobenzene-induced allergic dermatitis in vivo,” *Annals of Allergy, Asthma and Immunology*, vol. 108, no. 2, pp. 117–122, 2012, doi: 10.1016/j.anai.2011.10.013.

[148] A. C. Jones, H. C. Aspinall, and P. R. Chalker, “Molecular design of improved precursors for the MOCVD of oxides used in microelectronics ☆,” vol. 201, pp. 9046–9054, 2007, doi: 10.1016/j.surfcoat.2007.04.118.

[149] G. Adachi, N. Imanaka, and S. Tamura, “Ionic Conducting Lanthanide Oxides,” *Chemical Reviews*, pp. 2405–2429, 2002, doi: 10.1021/cr0103064 CCC:

[150] C. Benelli and D. Gatteschi, “Magnetism of Lanthanides in Molecular Materials with Transition-Metal Ions and Organic Radicals,” *Chemical Reviews*, pp. 2369–2387, 2002, doi: 10.1021/cr010303r.

[151] M. K. Okajima, M. Nakamura, T. Ogawa, H. Kurata, T. Mitsumata, and T. Kaneko, “Spongy hydrogels of cyanobacterial polyanions mediate energy-saving electrolytic metal-refinement,” *Industrial and Engineering Chemistry Research*, vol. 51, no. 25, pp. 8704–8707, 2012, doi: 10.1021/ie301117p.

[152] P. F. Moulton, “Spectroscopic and laser characteristics of Ti:Al_2O_3,” *Journal of the Optical Society of America B*, vol. 3, no. 1, p. 125, 1986, doi: 10.1364/josab.3.000125.

[153] A. Sanchez, R. E. Fahey, A. J. Strauss, and R. L. Aggarwal, “Room-temperature continuous-wave operation of a Ti:Al_2O_3 laser,” *Optics Letters*, vol. 11, no. 6, p. 363, 1986, doi: 10.1364/ol.11.000363.

[154] P. Albers, E. Stark, and G. Huber, “Continuous-wave laser operation and quantum efficiency of titanium-doped sapphire,” *Journal of the Optical Society of America B*, vol. 3, no. 1, p. 134, 1986, doi: 10.1364/josab.3.000134.

[155] U. Morgner *et al.*, “Sub-two-cycle pulses from a Kerr-lens mode-locked Ti : sapphire laser (vol 24, pg 411, 1999),” *Optics Letters*, vol. 24, no. 13, p. 920, 1999.

[156] A. Stingl, R. Szipöcs, M. Lenzner, C. Spielmann, and F. Krausz, “Sub-10-fs mirror-dispersion-controlled Ti:sapphire laser,” *Optics Letters*, vol. 20, no. 6, p. 602, 1995, doi: 10.1364/ol.20.000602.

[157] Spectra-physics, *Mai Tai Series Owners Manual*. 2015.

[158] Y. J. Huang, Y. S. Tzeng, C. Y. Tang, Y. P. Huang, and Y. F. Chen, “Tunable GHz pulse repetition rate operation in high-power TEM_00-mode Nd:YLF lasers at 1047 nm and 1053 nm with self mode locking,” *Optics Express*, vol. 20, no. 16, p. 18230, 2012, doi: 10.1364/oe.20.018230.

[159] Spectra-Physics, *Spectra-Physics Lasers-Spitfire User’s Manual*. 1995.

[160] Olympus, *Instructions BX60 System Microscope*. 2021.

[161] M. K. Okajima, R. Mishima, K. Amornwachirabodee, T. Mitsumata, K. Okeyoshi, and T. Kaneko, “Anisotropic swelling in hydrogels formed by cooperatively aligned megamolecules,” *RSC Advances*, vol. 5, no. 105, pp. 86723–86729, 2015, doi: 10.1039/c5ra18585h.

[162] S. Klimmer *et al.*, “All-optical polarization and amplitude modulation of second-harmonic

generation in atomically thin semiconductors," *Nature Photonics*, vol. 15, no. 11, pp. 837–842, 2021, doi: 10.1038/s41566-021-00859-y.

[163] B. Dev Choudhury, P. K. Sahoo, R. Sanatinia, G. Andler, S. Anand, and M. Swillo, "Surface second harmonic generation from silicon pillar arrays with strong geometrical dependence," *Optics Letters*, vol. 40, no. 9, p. 2072, 2015, doi: 10.1364/ol.40.002072.

[164] O. del Barco and J. M. Bueno, "Second harmonic generation signal in collagen fibers: role of polarization, numerical aperture, and wavelength," *Journal of Biomedical Optics*, vol. 17, no. 4, p. 045005, 2012, doi: 10.1117/1.jbo.17.4.045005.

[165] R. M. Williams, W. R. Zipfel, and W. W. Webb, "Interpreting second-harmonic generation images of collagen I fibrils," *Biophysical Journal*, vol. 88, no. 2, pp. 1377–1386, 2005, doi: 10.1529/biophysj.104.047308.

[166] B. Gutiérrez-Medina and M. de J. Sánchez Miranda, "Quantitative Image Restoration in Bright Field Optical Microscopy," *Biophysical Journal*, vol. 113, no. 9, pp. 1916–1919, 2017, doi: 10.1016/j.bpj.2017.09.002.

[167] D. S. James and P. J. Campagnola, "Recent Advancements in Optical Harmonic Generation Microscopy: Applications and Perspectives," *BME Frontiers*, vol. 2021, pp. 1–24, 2021, doi: 10.34133/2021/3973857.

[168] A. G. F. De Beer and S. Roke, "Obtaining molecular orientation from second harmonic and sum frequency scattering experiments in water: Angular distribution and polarization dependence," *Journal of Chemical Physics*, vol. 132, no. 23, 2010, doi: 10.1063/1.3429969.

[169] T. G. Zhang, C. H. Zhang, and G. K. Wong, "Determination of molecular orientation in molecular monolayers by second-harmonic generation," *Journal of the Optical Society of America B*, vol. 7, no. 6, p. 902, 1990, doi: 10.1364/josab.7.000902.

[170] L. Kong, C. Lee, S. H. Kim, and G. R. Ziegler, "Characterization of starch polymorphic structures using vibrational sum frequency generation spectroscopy," *Journal of Physical Chemistry B*, vol. 118, no. 7, pp. 1775–1783, 2014, doi: 10.1021/jp411130n.

[171] H. F. Zobel, "Molecules to Granules: A Comprehensive Starch Review," *Starch - Stärke*, vol. 40, no. 2, pp. 44–50, 1988, doi: 10.1002/star.19880400203.

[172] A. Seki, M. Yoshio, Y. Mori, and M. Funahashi, "Ferroelectric Liquid-Crystalline Binary Mixtures Based on Achiral and Chiral Trifluoromethylphenylterthiophenes," *ACS Applied Materials and Interfaces*, vol. 12, no. 47, pp. 53029–53038, 2020, doi: 10.1021/acsami.0c17717.

[173] K. Skarp and M. A. Handschy, "Ferroelectric Liquid Crystals. Material Properties and Applications," *Molecular Crystals and Liquid Crystals Incorporating Nonlinear Optics*, vol. 165, no. 1, pp. 439–509, 1988, doi: 10.1080/00268948808082210.

[174] M. G. Slavomir Pirkl, *Ferroelectric Liquid Crystals with High Spontaneous Polarization*. Mickaël Lallart (IntechOpen, 2011) Chapter 17, 2011.

[175] A. Mertelj *et al.*, “Splay Nematic Phase,” *Physical Review X*, vol. 8, no. 4, pp. 1–12, 2018, doi: 10.1103/PhysRevX.8.041025.

[176] R. J. Mandle and A. Mertelj, “Orientational order in the splay nematic ground state,” *Physical Chemistry Chemical Physics*, vol. 21, no. 34, pp. 18769–18772, 2019, doi: 10.1039/c9cp03581h.

[177] N. Sebastián *et al.*, “Ferroelectric-Ferroelastic Phase Transition in a Nematic Liquid Crystal,” *Physical Review Letters*, vol. 124, no. 3, pp. 1–6, 2020, doi: 10.1103/PhysRevLett.124.037801.

[178] R. Bhardwaj, X. Fang, and D. Attinger, “Pattern formation during the evaporation of a colloidal nanoliter drop: A numerical and experimental study,” *New Journal of Physics*, vol. 11, 2009, doi: 10.1088/1367-2630/11/7/075020.

[179] R. Bhardwaj, X. Fang, P. Somasundaran, and D. Attinger, “Self-assembly of colloidal particles from evaporating droplets: Role of DLVO interactions and proposition of a phase diagram,” *Langmuir*, vol. 26, no. 11, pp. 7833–7842, 2010, doi: 10.1021/la9047227.

[180] P. B. Petersen, R. J. Saykally, M. Mucha, and P. Jungwirth, “Enhence Concentration of Polarizable Anions at the Liquid Water Surface: SHG Spectroscopy and MD Simulations of Sodium Thiocyanide,” *J. Phys. Chem. B*, vol. 109, pp. 10915–10921, 2005, doi: 10.1021/jp050864c.

[181] G. Joshi, K. Okeyoshi, M. K. Okajima, and T. Kaneko, “Directional control of diffusion and swelling in megamolecular polysaccharide hydrogels,” *Soft Matter*, vol. 12, no. 25, pp. 5515–5518, 2016, doi: 10.1039/c6sm00971a.

[182] Y. R. Shen and V. Ostroverkhov, “Sum-frequency vibrational spectroscopy on water interfaces: Polar orientation of water molecules at interfaces,” *Chemical Reviews*, vol. 106, no. 4, pp. 1140–1154, 2006, doi: 10.1021/cr040377d.

[183] D. Lin-Vien, N. B. Colthup, W. G. Fateley, and J. G. Grasselli, “Compounds Containing the Carbonyl Group,” *The Handbook of Infrared and Raman Characteristic Frequencies of Organic Molecules*, vol. 3, pp. 117–154, 1991, doi: 10.1016/b978-0-08-057116-4.50015-8.

[184] K. Shikinaka, K. Okeyoshi, H. Masunaga, M. K. Okajima, and T. Kaneko, “Solution structure of cyanobacterial polysaccharide, sacran,” *Polymer*, vol. 99, pp. 767–770, 2016, doi: 10.1016/j.polymer.2016.08.003.